

タービンブレードにおける新しい渦はくり抑制法に
関する数値計算

**Numerical Simulation of a New Method for Vortex
Shedding Suppression on Turbine Blades**

2017

MOHD HAFIZ BIN MOHD NOH
モハマドハフィズビンモハマドノー

NAGOYA UNIVERSITY
GRADUATE SCHOOL OF ENGINEERING
DEPARTMENT OF AEROSPACE ENGINEERING

**NUMERICAL SIMULATION OF A NEW
METHOD FOR VORTEX SHEDDING
SUPPRESSION ON TURBINE BLADES**

Dissertation
Submitted in partial fulfillment of the
requirements for the degree of
Doctor of Engineering

by

Mohd Hafiz Bin Mohd Noh

Bachelor of Mechanical Engineering, KUiTTHO Malaysia, 2005
Master of Science (Thermal Power – Aerospace Propulsion), Cranfield University
United Kingdom, 2008

ABSTRACT

The performance of a gas turbine can be improved by minimizing component losses. The wakes of a turbine blade have an unsteady characteristic called vortex shedding. Vortex shedding contributes different loss mechanisms and is significant under high-speed conditions. Losses can be reduced by optimizing the blade geometry (shape) or by employing additional flow control techniques.

This research started with the development of CFD numerical code. The three-dimensional, Reynolds-averaged, compressible unsteady Navier–Stokes equations are solved. The Spalart–Allmaras turbulence model with Delayed Detached Eddy Simulation is used. Pre-processing of this simulation has been carried out using Gridgen Version 15, and post-processing has been visualized using Fieldview Version 16. The configuration of the blade is similar to the experiment conducted by Professor C.H Sieverding from Von Karman Institute, Belgium. The numerical method is validated by comparing the numerical results with experimental data obtained by Sieverding et al. The validation process gives a good agreement with the experimental results.

In chapter 3, a method for suppressing vortex shedding by connecting the pressure side and suction side via a series of micro through-holes is proposed. The chapter focuses on the effect of the size and location of the multiple micro holes at the trailing edge region on wake vortex shedding. First, the location of the hole was fixed at $S/D = \pm 0.62$, and three different hole diameters, D_h were tested; $0.054D$, $0.065D$ and $0.094D$. The flow through each micro-hole is modeled using the Hagen–Poiseuille equation. The result shows that at a fixed location of $S/D = \pm 0.62$, the hole diameter of $0.094D$ is the most effective among the three diameters. $D_h = 0.094D$ reduced the wake loss by a maximum of 10%, increased the trailing edge pressure distribution by 14% and gave a reduction in wake velocity profile thickness by a maximum of 24% as compared with the base (no hole) case. In addition, a series of micro-holes suppresses the vortex and reduces the pressure drop in the wake at lower distances of x/D . Then, the effect of a fixed diameter hole of $0.094D$ at three different locations; $S/D = \pm 0.73$, ± 0.62 and ± 0.58 was studied. The best location was obtained at $S/D = \pm 0.62$, where the

maximum reduction of average wake loss of approximately 2.6% was achieved, in comparison to the base case (without hole case). The wake loss is sensitive to the size and location of the hole. A micro-hole series of $D_h = 0.094D$ at $S/D = \pm 0.62$ showed the best result among others, and the flow field also showed the suppression of vortex downstream of the blade wake.

In chapter 4, the effect on a number of steady jet holes and their arrangement has been studied in a high subsonic turbine blade. This study focuses on the effect of single, double and triple rows of steady jets on wake vortex shedding, and the pressure around the blade and at the wake. The reaction of the steady jets has been validated with established data under a condition of: transonic flow at Mach Number of 0.8, Reynolds number of 3.0×10^6 , and angle of attack of 1.0° . The result revealed that the location of the hole is important: employing a series of steady jet slot-holes at the location of significant pressure difference can reduce the wake loss by a maximum of 13% and increase the trailing edge pressure distribution. Additionally, a double slot-hole series is beneficial in terms of pressure, where the concentrated pressure drop is reduced and surface pressure coefficient, $C_{p,sur}$ is increased by a maximum of 53%. The wake loss is also reduced by 46% in the case of double slots, and the flow field showed that the pressure drop at the wake was successfully eliminated, which led to a reduction in wake loss. In addition, the instantaneous vorticity also showed the strength of the wake vortex was reduced in all jet cases. The findings show that the double slot-hole series is more effective in reducing wake loss and pressure drop than the single or triple slot-hole series.

Chapter 5 describes techniques of making the slot-hole series. One of the techniques suitable for making a micro-hole on a turbine blade is the use of electrical discharge machining (EDM). A turbine blade is normally coated with a non-conductive coating in order to operate under high temperature conditions. In order to perform the EDM process, a conductive layer coating must be applied at the trailing edge area, since EDM requires a conductive surface. The full-scale simulation of this coating process is presented in this chapter. A hybrid computational method, combining FVM (Finite Volume Method) for solving the high-speed flows of compressible gas, and MPS (Moving Particle Semi-implicit) for solving the deformation of the droplet, has been

developed. This hybrid method is extended to simulate the plasma spray solving the compressible and viscous gas flow, heat transfer between the droplet and the substrate, and phase change of the droplet. This extension is an innovation, performed for the first time in the present study. The plasma spray processes have been simulated, from the acceleration to the solidification of the droplet on a substrate. The unsteady three-dimensional compressible Navier-Stokes equations are solved. As a result, a new method, coupling FVM and MPS via a virtual boundary method, has successfully been developed. The processes from the acceleration and deformation of a droplet under the influence of the ambient gas flow to the solidification of the droplet on a substrate have successfully been observed. The trend of flatness at the initial temperature of 300K is proportional to $Re^{0.26}$, which is consistent with the experimental result ($Re^{0.2-0.3}$). The splat shape results also agree well with the results of previous studies using the VOF method.

ACKNOWLEDGEMENTS



In the Name of Allah, the Most Gracious, the Most Merciful

First of all, I am deeply grateful to Allah S.W.T for all the blessings, strength, help and guidance that enabled me to finish this dissertation.

I wish to express my deepest appreciation to my supervisor, Associate Professor Dr. Koichi Mori, for his constant guidance, encouragement, continued support, motivation, patience and enthusiasm that have helped me to successfully complete my doctoral course and this dissertation.

I would also like to thank Emeritus Professor Dr. Yoshiaki Nakamura, who was responsible in bringing me to the Fluid Dynamics Laboratory at Nagoya University, Japan. This dedication is also extended to all members of my PhD viva committee – Professor Dr. Koji Nagata, Professor Dr. Yasuhiko Sakai, and Professor Dr. Jiro Kasahara – for their constructive advice and valuable discussions.

I would like to offer my heartfelt gratitude to all members in the Aerospace Engineering Fluid Dynamics Laboratory and Experiment team, Nagoya University, Japan, for their support and help during my PhD period. Not forgotten are all Malaysian friends and families in Nagoya, for their moral support and friendship.

I am greatly indebted to the Ministry of Higher Education Malaysia and Universiti Teknologi MARA (UiTM) Malaysia for the scholarship and financial support.

Finally, I would like to thank my beloved wife, Nur Azirah Abd Aziz, for sacrificing her life's comfort and taking care of our daughters, Nur Iris Rashika and Izumi Haifa, and our sons, Fathi Zulfiqar and Firas Adyan. I am deeply grateful to my brothers and sisters, my parents, Mohd Noh Masini and Sharipah Jaffar, and my parents-in-law, Abd. Aziz Ali and Rahmah Ibrahim, for their prayers and help during this PhD journey.

Table of Contents

Abstract	i
Acknowledgments	iv
Table of Contents	v
List of Figures	viii
List of Tables	ix
Nomenclature	x
CHAPTER 1 INTRODUCTION	
1.1 Preamble	1
1.2 Background of the Study	1
1.2.1 Reducing losses via blade shape optimization method	3
1.2.2 Reducing losses via flow control mechanism	3
1.2.2.1 Active Flow Control	4
1.2.2.2 Passive Flow Control	5
1.2.2.3 Hybrid Flow Control	7
1.3 Problem Statement	8
1.4 Objectives of the Study	8
1.5 Scope and Limitations of the Study	10
1.6 Significance of the Study	11
CHAPTER 2 METHODOLOGY AND MATHEMATICAL DERIVATION	
2.1 Preamble	12
2.2 Research Methodology Flow	12
2.3 Development of CFD Numerical Code	14
2.3.1 Navier-Stokes Equations	14
2.3.2 Lower Upper Symmetric Gauss Seidel Method (LU-SGS)	18
2.3.3 Inviscid Flux	23
2.3.3.1 AUSM (Advection Upstream Splitting Method) Scheme	23
2.3.3.2 Roe Scheme	25
2.3.4 Metrics, Jacobian and Geometrical Quantities	25
2.4 Boundary Conditions	26
2.4.1 Inlet Boundary Conditions	27
2.4.2 Outlet Boundary Conditions	27
2.4.3 Wall Boundary Conditions	28
2.4.4 Periodical Boundary Conditions	28
2.5 Turbulence Model	29
2.5.1 Spalart-Allmaras Turbulence Model (SA)	29

2.5.2	Detached Eddy Simulation (<i>DES</i>)	36
2.5.3	Delay Detached Eddy Simulation (<i>DDES</i>)	36
2.5.4	Improved Delay Detached Eddy Simulation (<i>IDDES</i>)	37
CHAPTER 3	EFFECT OF MULTIPLE THROUGH-HOLES ON THE TURBINE BLADE TRAILING EDGE	
3.1	Introduction	39
3.2	Computational Method	40
3.2.1	Boundary Conditions and Turbulence Model	41
3.3	Results and Findings	43
3.3.1	CFD Code Validations	43
3.3.2	Velocity Profile Thickness	48
3.3.3	Total Pressure	50
3.3.4	Wake Loss	53
3.3.5	Instantaneous Flow Field	57
3.4	Conclusions	61
CHAPTER 4	DIFFERENT SYNTHETIC JET HOLE ARRANGEMENTS ON A HIGH SUBSONIC TURBINE BLADE	
4.1	Introduction	63
4.2	Numerical Method	64
4.2.1	Boundary Conditions and Turbulence Model	65
4.3	Results and Findings	68
4.3.1	Surface Pressure Coefficient, $C_{P,sur}$ and Lift Coefficient, C_L	68
4.3.3	Flow Field Contours	71
4.3.4	Wake Loss	73
4.4	Conclusions	74
CHAPTER 5	SIMULATION OF COMPRESSIBLE AND MULTI-PHASE FLOW IN PLASMA SPRAY WITH FVM-MPS HYBRID METHOD	
5.1	Introduction	75
5.1.1	Electrical Discharge Machining (EDM)	75
5.1.2	Conductive Coatings	77
5.2	Methodology	79
5.2.1	Gas Flow Calculation	79
5.2.2	Particle Calculation Method	82
5.2.3	Interface Determination	82
5.2.4	External Forces (Surface Tension, Air Force) Model	83

5.2.5	Heat Conduction Model	83
5.2.6	Phase Transition (Solidification) Model	84
5.3	Results and Findings	84
5.4	Conclusions	88
CHAPTER 6 OVERALL CONCLUSION		
6.1	Preamble	90
6.2	Overall Conclusions	90
6.3	Recommendations	91
REFERENCES		93
LIST OF PUBLICATIONS		106

LIST OF FIGURES

Figure 2.1	Research Methodology Flow	13
Figure 3.1	Blade configuration and dimensions (in mm)	40
Figure 3.2	Trailing-edge S/D , x/D and Y/D reference system	40
Figure 3.3	Boundary conditions and simulation grid b) Close view of grid at micro-holes area	42
Figure 3.4	Connecting holes at the trailing edge of the blade	43
Figure 3.5	Trailing edge pressure distribution comparison among four different turbulence models and experimental data	44
Figure 3.6	Comparison of the isentropic Mach number on the blade	45
Figure 3.7	Instantaneous vorticity contour in the wake of the blade	46
Figure 3.8	Pressure Spectra comparison at $S/D = -0.62, -0.69, -0.82$	46
Figure 3.9	Boundary layer profile at trailing edge	47
Figure 3.10	Velocity profile at the blade wake for different hole diameters at (a), (b) and (c)	49
Figure 3.11	Time-averaged total pressure contour at the blade wake for different hole diameters	51
Figure 3.12	Distribution of trailing edge pressure along the trailing edge	52
Figure 3.13	Wake loss coefficients at $x/D = 0.2$	53
Figure 3.14	Wake loss coefficients at $x/D = 1.5$	55
Figure 3.15	Wake loss coefficients at $x/D = 0.2$ ($D_h = 0.094D$)	56
Figure 3.16	Wake loss coefficients at $x/D = 1.5$ ($D_h = 0.094D$)	57
Figure 3.17	Iso-surface instantaneous vorticity magnitude for base and hole case. Hole case condition ($D_h = 0.094D$, $S/D = \pm 0.62$)	58
Figure 3.18	Frequency comparison between base and hole case. Hole case condition ($D_h = 0.094D$, $S/D = \pm 0.62$)	60
Figure 3.19	Entropy comparison between base and hole case. Hole case condition ($D_h = 0.094D$, $S/D = \pm 0.62$)	61
Figure 4.1	Trailing-edge S/D , x/D and Y/D reference system	65
Figure 4.2	Boundary condition, calculation grid, blade configuration and dimensions (in mm)	66
Figure 4.3	The location selection for Synthetic jet configurations	66
Figure 4.4	Wake Loss for Base, A, B and C	67
Figure 4.5	Synthetic jet configurations: (a) single slot-hole (b) double slot-hole (c) triple slot-hole (d) slot-hole configurations	68
Figure 4.6	Pressure and Lift Coefficient for each case	69
Figure 4.7	Distribution of trailing edge pressure for each case	70
Figure 4.8	Time average total pressure contour: (a) Base, (b) Single Row Holes (c) Double Row Holes and (d) Triple Row Holes	72

Figure 4.9	Iso-surface Instantaneous vorticity for each case	73
Figure 4.10	Wake Loss for (a) Base, (b) Single (c) Double and (d) Triple Rows	74
Figure 5.1	Proposed method of conductor coating by Williamson [105]	76
Figure 5.2	Overall computational grid (b) Position of expansion nozzle [$d =$ nozzle diameter ($5mm$), $L =$ nozzle distance ($50mm$)]	79
Figure 5.3	The calculated velocity distributions of the jet initial conditions	80
Figure 5.4	Droplet around the flow ($Re = 133$)	80
Figure 5.5	The droplet velocity distribution in the collision process	85
Figure 5.6	The droplet temperature distribution during the collision process	86
Figure 5.7	Flatness as a function of impact velocity	87
Figure 5.8	Streamline around the droplet (a) CFD calculation (b) Reference [121]	88

LIST OF TABLES

Table 2.1	All Constants in Spalart Allmaras Turbulence Model	31
Table 3.1	Comparison frequency (kHz) between numerical and experimental	47
Table 3.2	Hole diameters at constant $S/D = \pm 0.62$	48
Table 3.3	Velocity profile thickness for different hole diameters at (a), (b) and (c)	48
Table 3.4	Variation of S/D at a constant hole diameter ($D_h = 0.094D$)	55
Table 4.1	Location of pressure difference	66
Table 5.1	Calculation condition of droplet and gas jet	81

NOMENCLATURE

C	Chord
D	trailing edge diameter
s	Pitch
P	total pressure
T	total temperature
M	Mach number
S	trailing edge length
L	length of the hole
D_h	hole's diameter
γ	specific heat ratio (1.4)
f_d	delay function (DDES)
ν	molecular viscosity
$U_{i,j,k}$	velocity gradient
d_{DES}	redefined DES length scale
C_{DES}	adjustable parameter (0.65)
$C_{p,sur}$	surface pressure coefficient
c	speed of sound
c_0	speed of sound in stagnation condition
Re	Reynolds number
mm	millimeter
LPT	Low Pressure Turbine
R	Gas constant (0.287)
x,y,z	Cartesian coordinate system

SUBSCRIPTS

01	at inlet to the blade
02	at outlet from the blade
is	isentropic
in	inside the calculation domain
$inlet$	inlet / boundary of the calculation domain
ax	axial
MUSCL	monotonic upstream–cantered scheme for conservation laws
SLAU	simple low dissipative AUSM

GREEK SYMBOLS

ν_T	kinematic eddy viscosity
---------	--------------------------

κ	von Karman constant (0.41)
ξ	wake loss
ρ	Density
T	Viscous stress
B	Heat diffusion
M	Kinematic viscosity
ξ, η, ζ	Generalized coordinate system

CHAPTER 1

INTRODUCTION

1.1 PREAMBLE

This chapter introduces the background detail of the study and the structure of the thesis. The contents are organized to emphasize the innovativeness of this study that contributes new knowledge in the niche area of gas turbine research. The sub-topics described in this chapter introduce the background to the study, set out the problem statement and objectives of the study, discuss its significance and limitations, and provide the scope of study. The chapter ends with an outline of thesis.

1.2 BACKGROUND OF THE STUDY

The performance of turbomachinery has generally been measured by its efficiency, associated with an increase in the ratio of power output to weight and size, and in respect to temperature and pressure. The loss in efficiency of a turbine is usually caused by irreversibility, which is frequently associated with viscous flow phenomena, heat transfer across finite temperature differences, and other non-equilibrium processes such as shock waves.

The viscous effects of a turbine are not restricted to boundary layers but are also present in the freestream due to the span-wise and pitch-wise gradients of the flow. They also exist within free shear layers and in the dissipation and mixing of viscous flow structures [1]. Interactions between a series of rotors and stators in an aero engine

contribute to overall noise and produce unsteady aerodynamic behavior. The turbine blade wakes are normally presented as an unsteady character because of the existence of large-scale organized structures in vortex streets, in the forms of vortex shedding. This vortex shedding is influenced by the geometry of the blade and the pressure gradient of the boundary layer state at the separation point. Furthermore, the wake of the turbine cascade trailing edge is frequently characterized by von Karman vortex streets [2]. At a higher speed condition, the formation of vortex shedding directly contributes to the amount of loss that will decrease the base pressure [3]. Base pressure here refers to the pressure distribution on the wall of the blade trailing edge.

Vortex shedding (or Karman vortex) has been observed for both wake area on the bluff body (cylinder) and on the turbine blade [4]. The vortex for a circular cylinder start to shed as low as at $Re = 40$ for a circular cylinder [5][6]. The formation of the vortex shedding region ends at the beginning of a periodic vortex street, which can be discerned at the beginning of the periodic wake by a sudden reduction of the low frequency irregularities observed in the formation region [5] or when the mainstream flow first crosses the wake axis [7].

There are several patterns of vortex shedding and Gostelow et al. [4] has noted the similarities among a vortex induced by vibration of a cylinder, an oscillating airfoil, and a turbine cascade at transonic flow condition. Cicatelli and Sieverding [8] have drawn attention to several conclusions about the vortex shedding mode of a transonic turbine cascade: the classical Von Karman vortex street that sheds from the pressure side and the suction side is frequently out-of-phase; a vortex that sheds from both sides in-phase (couples); double vortices that shed from each side out-of-phase (doublet); and doublet at the pressure side and von Karman at the suction side (hybrid).

Generally, the losses in a gas turbine can be assigned to three main origins, which are;

1. The losses due to profile loss, which are due to boundary layer [9].
2. The losses due to shock loss, which are due to normal and oblique shock [10].
3. The losses due to mixing loss, which are due to wake rapid dissipation and shock boundary layer [11].

Many studies have been carried out to improve the performance of gas turbines and one of them is by minimizing the loss formation. Component losses can be presented as a wake loss coefficient, profile loss, secondary loss, tip clearance loss and annulus loss [12][13]. Turbomachinery losses can be reduced via modification of blade surface geometry, and suitable flow control may cause the profile pressure to be increased [2]. There are two methods to reduce these losses: first, by optimization of the turbine blade shape; and secondly, by appropriate flow control. Both options have advantages and disadvantages.

1.2.1 Reducing losses via blade shape optimization method

Zhou et al. [14] investigated the effect of the trailing edge thickness on vortex shedding. In this research, the turbine trailing blade was modified; the trailing edge thickness was varied from 1.4% to 4.7% of the pitch size. The results show that when the trailing edge was increased from 1.4% to 2.8%, the losses were reduced, but further increments beyond this percentage, resulted in an increase in observed losses. Bourgoyne et al. [15] ran an experiment for a hydrofoil with a trailing edge bevel angle of 44% and suction side angle of 52%. It was found that a thicker trailing edge tends to increase the vortex shedding strength. Generally, optimization of blade shape may require a lengthy process including dismantling, machining, fabrication, etc. This may lead to higher costs. Thus accurate flow and boundary layer control seems to be a more feasible option.

1.2.2 Reducing losses via flow control mechanism

Flow control of a vortex may deal with various categories, including flow separation, vortex formation, flow reattachment, vortex breakdown and vortex instabilities. Several methods of flow control can be used, such as use of multiple vortices, use of different control surfaces, blowing and suction, low-frequency and high-frequency excitation, feedback control, passive control with wing flexibility, and plasma

actuators. Appropriate flow control can minimize vortex shedding and ultimately, completely suppress it. Generally, there are three main categories of flow control in a turbine blade, which are: active flow control, passive flow control, and hybrid (a combination of active and passive) flow control.

1.2.2.1 Active Flow Control

Active flow control is beneficial as it can “turn off” at a higher Reynolds number and is also able to control intensity, according to the location where separation occurs. Andre et al. [16] tried to suppress the unsteady wake vortex shedding of two rotated cylinders and found that doublet-like direction was efficient in suppressing the unsteady vortex shedding and successfully reduced the formation of drag. Meanwhile, the application of plasma actuators on a truncated trailing edge has been experimentally investigated by Tani [17], where a 300mm plate of 12mm thickness with a rounded nose and a truncated trailing edge was immersed in a uniform flow at free stream velocity ranging from 5m/s to 9m/s. He found that, by applying plasma actuators at some range of trailing edge, the total kinetic energy contained in vortex shedding was reduced by 40% and the von Karman vortex was successfully suppressed at a velocity of 7.5m/s. The same objective was also achieved by locating a cylinder with a smaller radius near the wake of the study cylinder model [18]. This approach had the effect of reducing the development of disturbance, where local stability of the flow has been disturbed, and caused diffusion of the concentrated vortices near the shear layer, which showed a successful reduction in vortex frequency and suppression. However, this method requires additional devices which may increase complexity in turbomachinery application.

Chan et al. [19] applied two suction holes on the cylinder, facing the oncoming flow. They concluded that the suction flow control method changed the alternative vortex into symmetrical mode and, at the same time, had a beneficial effect on lift and drag reduction. One well-known active flow control is the use of vortex generator jets (VGJs). This method has proven to be effective in flat plate application under adverse pressure gradients, works well in eliminating a stalled region, and can act the same as

steady flow jets under low mass flow value [20][21][22]. Even though VGJ has been a successful method of flow control and wake vortex suppression, it requires additional hardware which may increase overall weight.

Bernardini et al. [23] conducted an experiment to overview the effectiveness of a synthetic jet in suppressing the turbine cascade boundary layer. In their experiment, the rectangular slot was located at 60mm from the leading edge, and this result was also numerically investigated. The result shows that with two different Reynolds numbers, the synthetic jet had a positive impact on suppression, and reduced the separation in a time averaged domain. Borgeson [24] introduced a boundary layer control called micro-electromechanical system (MEMS) to trip the flow and delay the separation of cross flow of the cylinder. His result showed that by forcing at shedding frequency, the momentum drag can be reduced by 25%. However, this method tended to form grooves on the study model, which would lead to extra drag. In addition, MEMS was difficult to apply in a Low Pressure Turbine (LPT) as this application cannot withstand high temperatures and there are also manufacturing difficulty issues. VGJ and MEMS are both relatively complex and require additional power from the engine.

1.2.2.2 Passive Flow Control

Passive flow control seems more straightforward; it requires less power, is easy to fabricate and in some situations, it is more robust. One of the best-known methods of passive control is to modify the blade shape, which may include the use of submerged vortex-generators, large-eddy breakup devices, and elongated boundary-layer arches methods [25]. The triangular flow vortex generator device (VGD), has been explored by Chang [26], and an extensive study of semicircular VGD and simple vane VGD has been further investigated by Rao et al. [27]. However, even though most of the passive flow controls are able to control the boundary layer and suppress the flow efficiently, a serious disadvantage relates to overall engine performance. In particular, engines may not perform well at operating conditions with higher Reynolds numbers, where the passive control system tends to produce more severe drag. Bearmen et al. [28] varying

the length of an splitter plate at the blunted trailing edge. This method reduced the velocity fluctuation, which indicates that the flow was successfully controlled.

McCormick [29] attempted to reduce the higher drag formation which occurs in the most passive flow control by using a passive cavity and passive vortex generator method. The results revealed that the vortex generator successfully suppressed shock induced-separation and improved the boundary layer characteristics, while passive cavity flow control had a beneficial effect on drag reduction. However, although this passive control system is able to reduce drag formation, it faces problems when operating at higher Reynolds numbers.

Wheeler doublets (reverse S shaped curves) and transverse grooves (V shaped grooves) were explored by Lin et al. [30]. Although this approach was found to work well, it is not easy to integrate.

Another method associated with flow suppression for drag reduction involves riblets and micro textures. Riblets have been found to be an effective way for drag reduction by creating a viscosity-dominated region in the base of riblet valleys. Chu et al. [31] found that even though V-grooved riblets can reduce drag, it was also observed that the boundary layers between smooth and riblet walls consisted of counter-rotating stream-wise vortices, which produced positive turbulent stress. These findings were supported by El-Sanmi et al. [32], who performed a simulation on thin rectangular riblets that were uniformly distributed at a channel wall, using the DNS method. Although the results showed that drag formation was reduced, the DNS method entailed a high computational cost; eventually it limited the Reynolds number that could be run in the simulation.

The riblets method was also actively investigated experimentally by Choi et al. [33]. They found that a doublets-like counter rotation reduced the drag and suppressed the unsteady vortex wakes. This line of research was further improved in another study [34], where the degree of unsteady wake suppression was found to be proportional to the speed of the rotation; at a certain optimum rotation rate, a perfect suppression could be achieved, with the total drag reduced to zero. At this critical rotational rate, the wake forms an elliptic body. This finding is relevant to the research conducted by Bearmen et al. that found a 30% reduction of the drag could lead to 6%-9% of the vortex being

suppressed [35]. It should be mentioned here that vortex suppression can also be achieved by reducing drag formation.

Another well-known method of passive flow control is the use of dimples. The structure of dimples is straight forward and easy to understand, and the idea is derived from the surface of a golf ball [36][37]. Bearman et al. [38] investigated the effect of a dimple structure on a circular cylinder, and concluded that a circular cylinder with a dimpled surface resulted in a lower drag coefficient compared to a smooth cylinder. However, vortex shedding remained unaffected. Lake [39] studied passive recessed spherical dimples, and also varied the location of the dimples on an airfoil. The researcher observed reduction of drag and flow separation losses, but he failed to establish optimal dimple size and the effect on flow suppression.

All of the above studies have demonstrated significant results, but none of these methods have been tested in turbomachinery turbine application, as the flow field in a turbine is difficult to predict. Furthermore, apart from focusing on vortex suppression, another important parameter to be focused on is pressure distribution, since vortex generation may penalize pressure formation, which directly influences the overall performance of a gas turbine engine. These findings are supported by Effendy et al. [40] in their research on unsteady phenomena (shock wave) in a turbine cascade. They used pressure loss as an indicator to measure shock wave strength, where the conclusion leads to gas turbine performance degradation. Turbine efficiency may drop as the axial gap increases, which is related to diffusion of vortices and rotor formation wake upstream, which results in an increase in pressure loss [41]. In another study, a cut back trailing edge design was investigated. The study confirmed that RANS agreed well with experimental data for pressure distribution but was not suitable for calculation of film cooling [40]. This shows that pressure distribution is a key for any performance prediction of a gas turbine.

1.2.2.3 Hybrid Flow Control

Hybrid flow control is a method which combines active and passive flow control. Veldhuis et al. [42] ran an experiment on an airfoil in which his team located a small

cylinder between the front flap, and non-pulsed plasma actuators over the flap. The cylinder functioned as a vortex generator and the plasma actuators acted to re-attach the flow. The actuators suppressed the flow significantly at a velocity of 30m/s – 40m/s. The result showed that in certain conditions, the lift increased to a maximum of 18%.

1.3 PROBLEM STATEMENT

This study focuses on four problems that arise from the aforementioned issue introduced earlier in this chapter. The problems are being stated as below;

1. To date, very few CFD numerical code (programs) have been developed and validated in respect of the experimental data provided by Sieverding et al. [71][72]. So this study is conducted for future investigation of the respective turbine blade.
2. There is a lack of research regarding hybrid flow control which combines passive and active methods of control, and which is believed to be beneficial for wake flow control.
3. The effect of the number of micro holes of a steady jet and their arrangement, span-wise and stream-wise direction, for a high subsonic turbine blade has yet to be investigated.
4. Most CFD programs have used the VOF (Volume of Fluid) method to simulate droplet trajectories of thermal spray coatings. This may lead to higher computational cost while at the same time; the calculation of particle deformation cannot be achieved.

1.4 OBJECTIVES OF THE STUDY

Based on the problems identified above, the objectives of this study are elaborated as follows:

1. **To suppress vortex shedding at the wake area by connecting the suction side and the pressure side of turbine blade.**

To implement this method, it is first necessary **to develop a numerical code CFD (computational program) based on the experimental data obtained from Sieverding et al. [71][72] from the Von Karman Institute, Belgium.** The validation will be based on pressure distribution on a turbine blade at its trailing edge and the isentropic Mach number along the blade surface. This validation is also supported by the result of frequency data at the initial location of vortex shedding formation and the dimensionless velocity at a distance equal to one of trailing diameter (boundary layer profile). The data on pressure distribution will focus between $-2.0 < S/D < +2.0$ since at this area, the pressure distribution is significantly different (and also because the experimental pressure probe has been placed along this area). A series of micro-holes which connect between the suction side and the pressure side of the turbine blade are introduced. The physics of the micro-hole is represented in terms of a finite mathematical model – dimensionless velocity via the Hagen-Poiseuille equation. The size of the micro-hole is also optimized. This micro-hole should be capable of suppressing the vortex shedding, reducing the wake loss produced and increasing the base pressure. The flow field of vortex shedding and pressure drop also needs to be analyzed.

2. To suppress wake vortex shedding by applying multi-holes of a steady synthetic jet and to study the effect of their arrangement (stream wise and span wise).

In order to achieve this objective, the possibility of applying a steady synthetic jet is considered, because although this application is simple, it gives substantial benefits in terms of vortex suppression. This method uses the same validated numerical code as described in the previous objective. Different arrangements of holes, which include single-, double- and triple-hole arrangements are carried out in this study. The validation of the mathematical model of steady synthetic jet has been carried out on an airfoil case [94].

- 3. To perform a full scale model of a simulation for a thermal conductive coating (the first step for making a series of holes, which was explained in the first objective)**

In order to achieve this objective, the development of a **numerical code CFD (computational program) coupling between Finite Volume Method (FVM) and Moving Particle Semi- Implicit (MPS)** for modeling of droplet impingement on a substrate is essential. For the first time, a hybrid solution which combines FVM (Finite Volume Method) for solving the spray of the gas jet, and MPS (Moving Particle Semi-implicit) for solving the deformation of the droplet has been performed. In the past, plasma spray was related to Full-scaling modeling, where a simple model as a point mass is applied to represent the powder particle behavior, and the jet has been solved by using either Finite Difference Method or the Finite Volume Method.

1.5 SCOPE AND LIMITATIONS OF THE STUDY

In respect to the listed objectives, the following scope has been outlined to ensure the study remains focused and also to ensure that the study outcomes are sufficient to provide specific in-depth knowledge for other researchers to pursue further studies in the turbomachinery niche area.

This research is focused on a turbine cascade, in which the parameter and size are similar to the experimental apparatus of Siverding et al. [71][72]. However, the numerical program which has been developed will be capable of being used in any turbomachinery turbine blade calculation studies for compressible flow. The calculation uses only the Lower Upper Symmetric Gauss Siedel method, together with a second-order dual time method, to calculate the unsteady flow. This study is limited to one equation turbulence model, which includes Spalart Allamaras (SA), Detached Eddy Simulation (DES), Delay Detached Eddy Simulation (DDES) and Improved Delay Detached Eddy Simulation (IDDES) turbulence models.

1.6 SIGNIFICANCE OF THE STUDY

1. The developed CFD code will be a viable alternative to experimentation. This numerical CFD work has been completed and this could boost a more detailed investigation on turbine blades. Future users will be able to carry out parametric studies without conducting experiments. Apart from applied research, fundamental research can also be conducted using this developed code.
2. This study introduces a new flow control system which is simpler and more reliable; it has contributed an innovation to flow control technology by combining active and passive flow control. Small flow disturbance in turbine flow (at the suction surface) is beneficial in reducing the vortex strength at the wake area.
3. For the first time, the FVM and MPS methods have been coupled, which has produced significant benefits. A full scaling simulation has been successfully observed. A major benefit of coupling is the reduction in complexity and computational time, because two calculation processes have been combined into one. By using this newly developed program, the calculation of particle impingement on a study substrate can be accurately calculated. This is considered to be a new approach since the previous method used only the Volume of Fluid (VOF) method. Furthermore, this new coupling does not require very fine meshing, especially at the region where particles are injected into the substrate.

CHAPTER 2

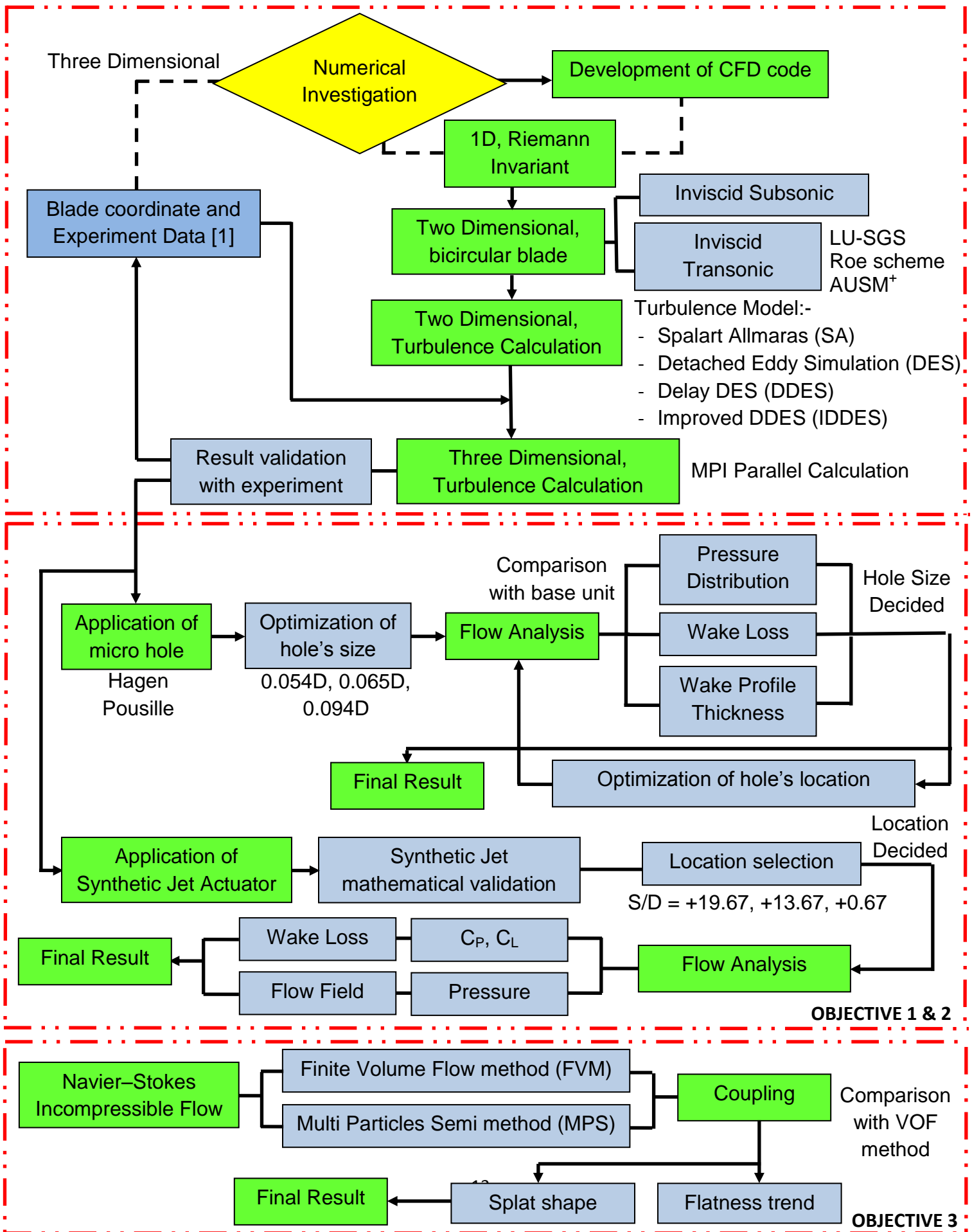
METHODOLOGY

2.1 PREAMBLE

In Chapter 2, the methods to achieve the objectives of study are highlighted. This study has successfully executed three major tasks: (i) the development of numerical code for two dimensional and three dimensional turbine cascades (ii) application of micro-holes in terms of finite dimensionless velocity and steady jet configuration study; and (iii) a coupling between Finite Volume Method and Moving Particles Semi Implicit (MPS) method, with a comparison to the established Volume of Fluid (VOF) method.

2.2 RESEARCH METHODOLOGY FLOW

The research methodology in this study is divided into three main phases. Each phase focuses on the specific methods applied to achieve the objectives of the study. Fig. 2.1 shows the research methodology flow chart that is referred to throughout this thesis.



2.3 DEVELOPMENT OF CFD NUMERICAL CODE

2.3.1 NAVIER-STOKES EQUATIONS

The conservation of mass, momentum, and energy equations in the unsteady compressible three dimensional viscous flows for Navier Stokes, can be represented as;

$$\frac{\partial Q}{\partial t} + \frac{\partial E}{\partial x} + \frac{\partial F}{\partial y} + \frac{\partial G}{\partial z} = \frac{\partial E_v}{\partial x} + \frac{\partial F_v}{\partial y} + \frac{\partial G_v}{\partial z}. \quad (2.1)$$

For conservative form and Cartesian coordinate system, it can be represented as;

$$Q = \begin{bmatrix} \rho \\ \rho u \\ \rho v \\ \rho w \\ e \end{bmatrix}, \quad E = \begin{bmatrix} \rho u \\ \rho u^2 + p \\ \rho uv \\ \rho uw \\ u(e + p) \end{bmatrix}, \quad F = \begin{bmatrix} \rho v \\ \rho vu \\ \rho v^2 + p \\ \rho vw \\ u(e + p) \end{bmatrix}, \quad G = \begin{bmatrix} \rho w \\ \rho wu \\ \rho wv \\ \rho w^2 + p \\ u(e + p) \end{bmatrix}, \quad (2.2)$$

$$E_v = \begin{bmatrix} 0 \\ \tau_{xx} \\ \tau_{xy} \\ \tau_{xz} \\ \beta_x \end{bmatrix}, \quad F_v = \begin{bmatrix} 0 \\ \tau_{yx} \\ \tau_{yy} \\ \tau_{yz} \\ \beta_y \end{bmatrix}, \quad G_v = \begin{bmatrix} 0 \\ \tau_{zx} \\ \tau_{zy} \\ \tau_{zz} \\ \beta_z \end{bmatrix}.$$

in which Q represents conservative variables, E, F and G represent inviscid fluxes, and E_v , F_v and G_v represent viscous fluxes, as shown in Eq. 2.2. The viscous stress and heat diffusion can be estimated as follows:

$$\begin{aligned} \tau_{xx} &= \frac{2}{3}\mu \left(2\frac{\partial u}{\partial x} - \frac{\partial v}{\partial y} - \frac{\partial w}{\partial z} \right), & \tau_{xy} &= \tau_{yx} = \mu \left(2\frac{\partial u}{\partial y} - \frac{\partial v}{\partial x} \right), \\ \tau_{yy} &= \frac{2}{3}\mu \left(2\frac{\partial v}{\partial y} - \frac{\partial w}{\partial z} - \frac{\partial u}{\partial x} \right), & \tau_{yz} &= \tau_{zy} = \mu \left(2\frac{\partial v}{\partial z} - \frac{\partial w}{\partial y} \right), \\ \tau_{zz} &= \frac{2}{3}\mu \left(2\frac{\partial w}{\partial z} - \frac{\partial u}{\partial x} - \frac{\partial v}{\partial y} \right), & \tau_{zx} &= \tau_{xz} = \mu \left(2\frac{\partial w}{\partial x} - \frac{\partial u}{\partial z} \right), \end{aligned} \quad (2.3)$$

$$\begin{aligned}\beta_x &= u\tau_{xx} + v\tau_{xy} + w\tau_{xz} + k \frac{\partial T}{\partial x} , \\ \beta_y &= u\tau_{yx} + v\tau_{yy} + w\tau_{yz} + k \frac{\partial T}{\partial y} , \\ \beta_z &= u\tau_{zx} + v\tau_{zy} + w\tau_{zz} + k \frac{\partial T}{\partial z} .\end{aligned}$$

The three dimensionless unsteady compressible Navier Stokes equation form (in Cartesian coordinate) can be represented as expression (2.4).

$$\frac{\partial Q}{\partial t} + \frac{\partial E}{\partial x} + \frac{\partial F}{\partial y} + \frac{\partial G}{\partial z} = \frac{1}{Re_\infty} \left(\frac{\partial E_v}{\partial x} + \frac{\partial F_v}{\partial y} + \frac{\partial G_v}{\partial z} \right). \quad (2.4)$$

Other dimensionless forms which associate with the equation above are as follows:

$$\begin{aligned}e &= \frac{p}{\rho(\gamma - 1)} + \frac{1}{2}(u^2 + v^2 + w^2) , & c_v &= \frac{1}{\gamma(\gamma - 1)M_\infty} , \\ k &= \frac{\mu}{(\gamma - 1)\mu_\infty^2 Pr} , & p &= \rho RT , \\ \mu &= \frac{1 + S_0/T_\infty}{T + S_0/T_\infty} T^{2/3} , & R &= \frac{1}{\gamma\mu_\infty^2} , & \mu_\infty &= \frac{v_\infty}{c_\infty} .\end{aligned} \quad (2.5)$$

As for body fitted grid, the procedure of mapping the Cartesian coordinate system (x,y,z) into the coordinate system (ξ,η,ζ) needs to be done, as presented in Eq. (2.6). This procedure has been explained in detail in [43][44].

$$x = x(\varepsilon, \eta, \zeta) , \quad y = y(\varepsilon, \eta, \zeta) , \quad z = z(\varepsilon, \eta, \zeta) . \quad (2.6)$$

Total differential of the dependent variables in Eq. (2.6) can be formed into a matrix as follows:

$$\begin{bmatrix} dx \\ dy \\ dz \end{bmatrix} = \begin{bmatrix} x_\varepsilon & x_\eta & x_\zeta \\ y_\varepsilon & y_\eta & y_\zeta \\ z_\varepsilon & z_\eta & z_\zeta \end{bmatrix} \begin{bmatrix} d\varepsilon \\ d\eta \\ d\zeta \end{bmatrix} . \quad (2.7)$$

Following a similar procedure, the generalized coordinate system (ξ, η, ζ) is in a function of the Cartesian coordinate system.

$$\varepsilon = \varepsilon(x, y, z) , \quad \eta = \eta(x, y, z) , \quad \zeta = \zeta(x, y, z) . \quad (2.8)$$

By using the total differential procedure, we can obtain Eq. (2.9).

$$\begin{bmatrix} d\varepsilon \\ d\eta \\ d\zeta \end{bmatrix} = \begin{bmatrix} \varepsilon_x & \varepsilon_y & \varepsilon_z \\ \eta_x & \eta_y & \eta_z \\ \zeta_x & \zeta_y & \zeta_z \end{bmatrix} \begin{bmatrix} dx \\ dy \\ dz \end{bmatrix} . \quad (2.9)$$

From Eq. (2.7) and Eq. (2.9), we can obtain Eq. (2.10)

$$\begin{bmatrix} \varepsilon_x & \varepsilon_y & \varepsilon_z \\ \eta_x & \eta_y & \eta_z \\ \zeta_x & \zeta_y & \zeta_z \end{bmatrix} = \begin{bmatrix} x_\varepsilon & x_\eta & x_\zeta \\ y_\varepsilon & y_\eta & y_\zeta \\ z_\varepsilon & z_\eta & z_\zeta \end{bmatrix}^{-1} . \quad (2.10)$$

From Eq. (2.10), the expression (2.11) can be obtained as:

$$\begin{aligned} \varepsilon_x &= J(y_\eta z_\zeta - y_\zeta z_\eta) , & \varepsilon_y &= J(z_\eta x_\zeta - z_\zeta x_\eta) , & \varepsilon_z &= J(x_\eta y_\zeta - x_\zeta y_\eta) , \\ \eta_x &= J(y_\zeta z_\varepsilon - y_\varepsilon z_\zeta) , & \eta_y &= J(z_\zeta x_\varepsilon - z_\varepsilon x_\zeta) , & \eta_z &= J(x_\zeta y_\varepsilon - x_\varepsilon y_\zeta) , \\ \zeta_x &= J(y_\varepsilon z_\eta - y_\eta z_\varepsilon) , & \zeta_y &= J(z_\zeta x_\varepsilon - z_\varepsilon x_\zeta) , & \zeta_z &= J(x_\zeta y_\varepsilon - x_\varepsilon y_\zeta) . \end{aligned} \quad (2.11)$$

The Jacobian "J" can be obtained by the reciprocal of the determinant of the matrix of the right hand side of Eq. (2.11), which is shown in Eq. (2.12)

$$J^{-1} = x_\varepsilon(y_\eta z_\zeta - y_\zeta z_\eta) + x_\eta(y_\zeta z_\varepsilon - y_\varepsilon z_\zeta) + x_\zeta(y_\varepsilon z_\eta - y_\eta z_\varepsilon) . \quad (2.12)$$

Eq. (2.4) can be transformed into a generalized coordinate system as;

$$\begin{aligned}
\frac{\partial E}{\partial x} &= \varepsilon_x \frac{\partial E}{\partial \varepsilon} + \eta_x \frac{\partial E}{\partial \eta} + \zeta_x \frac{\partial E}{\partial \zeta} \\
&= J \frac{\partial}{\partial \varepsilon} \left(\frac{\varepsilon_x E}{J} \right) + \frac{\partial}{\partial \eta} \left(\frac{\eta_x E}{J} \right) + \frac{\partial}{\partial \zeta} \left(\frac{\zeta_x E}{J} \right) \\
&= J \frac{\partial}{\partial \varepsilon} (J^{-1}(\varepsilon_x E)) + \frac{\partial}{\partial \eta} (J^{-1}(\eta_x E)) + \frac{\partial}{\partial \zeta} (J^{-1}(\zeta_x E)) .
\end{aligned} \tag{2.13}$$

And the dimensionless generalized coordinate system for Navier-Stokes can be represented in terms of relation (2.14);

$$\frac{\partial \hat{Q}}{\partial t} + \frac{\partial \hat{E}}{\partial \varepsilon} + \frac{\partial \hat{F}}{\partial \eta} + \frac{\partial \hat{G}}{\partial \zeta} = \frac{1}{Re_\infty} \left(\frac{\partial \hat{E}_v}{\partial \varepsilon} + \frac{\partial \hat{F}_v}{\partial \eta} + \frac{\partial \hat{G}_v}{\partial \zeta} \right) , \tag{2.14}$$

where

$$\begin{aligned}
\hat{Q} &= J^{-1} Q , \\
\hat{E} &= J^{-1}(\varepsilon_x E + \varepsilon_y F + \varepsilon_z G) , & \hat{E}_v &= J^{-1}(\varepsilon_x E_v + \varepsilon_y F_v + \varepsilon_z G_v) , \\
\hat{F} &= J^{-1}(\eta_x E + \eta_y F + \eta_z G) , & \hat{E}_v &= J^{-1}(\eta_x E_v + \eta_y F_v + \eta_z G_v) , \\
\hat{G} &= J^{-1}(\zeta_x E + \zeta_y F + \zeta_z G) , & \hat{G}_v &= J^{-1}(\zeta_x E_v + \zeta_y F_v + \zeta_z G_v) .
\end{aligned} \tag{2.15}$$

and

$$\begin{aligned}
\hat{Q} &= \begin{bmatrix} \rho \\ \rho u \\ \rho v \\ \rho w \\ e \end{bmatrix} , & \hat{E} &= J^{-1} \begin{bmatrix} \rho U \\ \rho u U + \varepsilon_x p \\ \rho v U + \varepsilon_y p \\ \rho w U + \varepsilon_z p \\ U(e + p) \end{bmatrix} , & \hat{F} &= J^{-1} \begin{bmatrix} \rho V \\ \rho u V + \eta_x p \\ \rho v V + \eta_y p \\ \rho w V + \eta_z p \\ V(e + p) \end{bmatrix} , \\
\hat{G} &= J^{-1} \begin{bmatrix} \rho W \\ \rho u W + \zeta_x p \\ \rho v W + \zeta_y p \\ \rho w W + \zeta_z p \\ W(e + p) \end{bmatrix} , & E_v &= \begin{bmatrix} 0 \\ \varepsilon_x \tau_{xx} + \varepsilon_y \tau_{xy} + \varepsilon_z \tau_{xz} \\ \varepsilon_x \tau_{yx} + \varepsilon_y \tau_{yy} + \varepsilon_z \tau_{yz} \\ \varepsilon_x \tau_{zx} + \varepsilon_y \tau_{zy} + \varepsilon_z \tau_{zz} \\ \varepsilon_x \beta_x + \varepsilon_y \beta_y + \varepsilon_z \beta_z \end{bmatrix} ,
\end{aligned} \tag{2.16}$$

$$F_v = \begin{bmatrix} 0 \\ \eta_x \tau_{xx} + \eta_y \tau_{xy} + \eta_z \tau_{xz} \\ \eta_x \tau_{yx} + \eta_y \tau_{yy} + \eta_z \tau_{yz} \\ \eta_x \tau_{zx} + \eta_y \tau_{zy} + \eta_z \tau_{zz} \\ \eta_x \beta_x + \eta_y \beta_y + \eta_z \beta_z \end{bmatrix}, \quad G_v = \begin{bmatrix} 0 \\ \zeta_x \tau_{xx} + \zeta_y \tau_{xy} + \zeta_z \tau_{xz} \\ \zeta_x \tau_{yx} + \zeta_y \tau_{yy} + \zeta_z \tau_{yz} \\ \zeta_x \tau_{zx} + \zeta_y \tau_{zy} + \zeta_z \tau_{zz} \\ \zeta_x \beta_x + \zeta_y \beta_y + \zeta_z \beta_z \end{bmatrix},$$

where U , V , and W represent the contra-variant velocities as shown in Eq. (2.17).

$$\begin{aligned} U &= \varepsilon_x u + \varepsilon_y v + \varepsilon_z w, \\ V &= \eta_x u + \eta_y v + \eta_z w, \\ W &= \zeta_x u + \zeta_y v + \zeta_z w. \end{aligned} \tag{2.17}$$

2.3.2 LOWER UPPER SYMMETRIC GAUSS SEIDEL METHOD (LU-SGS)

LU-SGS is an implicit scheme which is also known as Lower-Upper Symmetric Successive Over-relaxation (LU-SSOR) [45][46][47]. Unlike Alternating Direction Implicit (ADI), LU-SGS is stable not only for two dimensional calculations but also for three dimensional calculations [45]. From Eq. (2.18);

$$\frac{\partial \hat{Q}}{\partial t} + \frac{\partial \hat{E}}{\partial \varepsilon} + \frac{\partial \hat{F}}{\partial \eta} + \frac{\partial \hat{G}}{\partial \zeta} = \frac{1}{Re_\infty} \left(\frac{\partial \hat{E}_v}{\partial \varepsilon} + \frac{\partial \hat{F}_v}{\partial \eta} + \frac{\partial \hat{G}_v}{\partial \zeta} \right), \tag{2.18}$$

we can rearrange Eq. (2.18), and eventually the outcome relation is as follows:

$$\frac{\partial \hat{Q}}{\partial t} + \frac{\partial}{\partial \varepsilon} \left[\hat{E} - \frac{1}{Re_\infty} \hat{E}_v \right] + \frac{\partial}{\partial \eta} \left[\hat{F} - \frac{1}{Re_\infty} \hat{F}_v \right] + \frac{\partial}{\partial \zeta} \left[\hat{G} - \frac{1}{Re_\infty} \hat{G}_v \right] = 0. \tag{2.19}$$

The dual time method is used to obtain accurate time integration for unsteady calculations [48][49]. Derivative of pseudo-time, Γ is introduced as shown in Eq. (2.20).

$$\frac{\partial \hat{Q}}{\partial \Gamma} + \frac{\partial}{\partial \varepsilon} \left[\hat{E} - \frac{1}{Re_\infty} \hat{E}_v \right] + \frac{\partial}{\partial \eta} \left[\hat{F} - \frac{1}{Re_\infty} \hat{F}_v \right] + \frac{\partial}{\partial \zeta} \left[\hat{G} - \frac{1}{Re_\infty} \hat{G}_v \right] = 0. \tag{2.20}$$

For implicit integration, Eq. (2.20) can be written as follows;

$$\left[\frac{\partial \hat{Q}}{\partial t} + \frac{\partial}{\partial x} \left[\hat{E} - \frac{1}{Re_\infty} \hat{E}_v \right] + \frac{\partial}{\partial y} \left[\hat{F} - \frac{1}{Re_\infty} \hat{F}_v \right] + \frac{\partial}{\partial z} \left[\hat{G} - \frac{1}{Re_\infty} \hat{G}_v \right] \right]^{m+1} + \frac{\hat{Q}^{m+1} - \hat{Q}^m}{\Delta \Gamma} . \quad (2.21)$$

Inviscid flux \hat{E}^{m+1} can be linearized using a Taylor series expansion.

$$\hat{E}^{m+1} \approx E^m + \left[\frac{\partial \hat{E}}{\partial \hat{Q}} \right]^m [\hat{Q}^{m+1} - \hat{Q}^m] = \hat{E}^m + \hat{A}^m \Delta \hat{Q}^m . \quad (2.22)$$

Also, \hat{F}^{m+1} and \hat{G}^{m+1} can be treated in the same way, and presented in Eq. (2.23);

$$\begin{aligned} \hat{F}^{m+1} &\approx F^m + \left[\frac{\partial \hat{F}}{\partial \hat{Q}} \right]^m [\hat{Q}^{m+1} - \hat{Q}^m] = \hat{F}^m + \hat{B}^m \Delta \hat{Q}^m , \\ \hat{G}^{m+1} &\approx G^m + \left[\frac{\partial \hat{G}}{\partial \hat{Q}} \right]^m [\hat{Q}^{m+1} - \hat{Q}^m] = G^m + \hat{C}^m \Delta \hat{Q}^m . \end{aligned} \quad (2.23)$$

If we substitute Eq. (2.22) and Eq. (2.23) into Eq. (2.21), we can achieve Eq. (2.24).

$$\begin{aligned} \left[I + \frac{\partial \hat{A}}{\partial \hat{\varepsilon}} + \frac{\partial \hat{B}}{\partial \hat{\eta}} + \frac{\partial \hat{C}}{\partial \hat{\zeta}} \right]^m \Delta \hat{Q}^m = - \left[\frac{\partial \hat{Q}}{\partial t} \right]^{m+1} \\ - \left[\frac{\partial}{\partial \varepsilon} \left(\hat{E} - \frac{1}{Re_\infty} \hat{E}_v \right) + \frac{\partial}{\partial \eta} \left(\hat{F} - \frac{1}{Re_\infty} \hat{F}_v \right) + \frac{\partial}{\partial \zeta} \left(\hat{G} - \frac{1}{Re_\infty} \hat{G}_v \right) \right]^m , \end{aligned} \quad (2.24)$$

where

$$I = \begin{bmatrix} 1/\Delta \Gamma & 0 & 0 & 0 & 0 \\ 0 & 1/\Delta \Gamma & 0 & 0 & 0 \\ 0 & 0 & 1/\Delta \Gamma & 0 & 0 \\ 0 & 0 & 0 & 1/\Delta \Gamma & 0 \\ 0 & 0 & 0 & 0 & 1/\Delta \Gamma \end{bmatrix} . \quad (2.2)$$

The dual time approach is based on a second-order accurate time which can be expressed as relation (2.26):

$$\begin{aligned}
\left[\frac{\partial \hat{Q}}{\partial t}\right]^{m+1} &= \left[\frac{1}{J} \frac{\partial \hat{Q}}{\partial t} + Q \frac{\partial}{\partial t} \left(\frac{1}{J}\right)\right]^{m+1} = \frac{1}{J} \frac{3Q^{m+1} - 4Q^n + Q^{n+1}}{2\Delta t} + \left[\frac{1}{J} Q \frac{\partial}{\partial t}\right]^{m+1} \\
&= \frac{1}{J} \frac{3\Delta Q^m}{2\Delta t} + \frac{1}{J} \frac{3Q^m - 4Q^n + Q^{n+1}}{2\Delta t} + \left[Q \frac{\partial}{\partial t} \left(\frac{1}{J}\right)\right]^{m+1} \\
&= \frac{3\Delta \hat{Q}^m}{2\Delta t} + \frac{3\hat{Q}^m - 4\hat{Q}^n + \hat{Q}^{n+1}}{2\Delta t} + \underbrace{\left[Q \frac{\partial}{\partial t} \left(\frac{1}{J}\right)\right]^{m+1}}_0 .
\end{aligned} \tag{2.26}$$

The term $\left[Q \frac{\partial}{\partial t} \left(\frac{1}{J}\right)\right]^{m+1}$ is equal to zero since the calculation grid is not a moving grid in this research. The solution is advanced in pseudo (nonphysical) time step “ m ” between each physical time step “ n ”. Substitute Eq. (2.26) into Eq. (2.24);

$$\begin{aligned}
\left[\hat{I} + \frac{\partial \hat{A}}{\partial \varepsilon} + \frac{\partial \hat{B}}{\partial \eta} + \frac{\partial \hat{C}}{\partial \zeta}\right]^m \Delta \hat{Q}^m &= \\
&- \left[\frac{\partial}{\partial \varepsilon} \left(\hat{E} - \frac{1}{Re_\infty \hat{E}_v}\right) + \frac{\partial}{\partial \eta} \left(\hat{F} - \frac{1}{Re_\infty \hat{F}_v}\right) + \frac{\partial}{\partial \zeta} \left(\hat{G} - \frac{1}{Re_\infty \hat{G}_v}\right)\right]^m \\
&- \frac{3\hat{Q}^m - 4\hat{Q}^n + \hat{Q}^{n+1}}{2\Delta t} = \text{Right Hand Side (RHS)} ,
\end{aligned} \tag{2.27}$$

where

$$\hat{I} = \text{diag} \left[\frac{3}{2\Delta t} + \frac{1}{\Delta \Gamma}, \frac{3}{2\Delta t} + \frac{1}{\Delta \Gamma} \right] . \tag{2.28}$$

In Eq. (2.28), the term $\partial/\partial \xi, \partial/\partial \eta$ and $\partial/\partial \zeta$ can be approximated by central difference operators D_ξ, D_η and D_ζ , respectively.

$$\left[\hat{I} + \frac{\partial \hat{A}}{\partial \varepsilon} + \frac{\partial \hat{B}}{\partial \eta} + \frac{\partial \hat{C}}{\partial \zeta} \right] \Delta \hat{Q} = \hat{I} + [(D_{\varepsilon}^{-} \hat{A}^{+} + D_{\varepsilon}^{+} \hat{A}^{-}) + (D_{\eta}^{-} \hat{B}^{+} + D_{\eta}^{+} \hat{B}^{-}) + (D_{\zeta}^{-} \hat{C}^{+} + D_{\zeta}^{+} \hat{C}^{-})] \Delta \hat{Q} \quad , \quad (2.29)$$

where $D_{\xi}^{-}, D_{\eta}^{-}$ and D_{ζ}^{-} are backward-difference operators and $D_{\xi}^{+}, D_{\eta}^{+}$ and D_{ζ}^{+} are forward-difference operators.

$$D_{\varepsilon}^{-} \hat{A}^{+} = \frac{\hat{A}_{i,j,k}^{+} - \hat{A}_{i-1,j,k}^{+}}{\Delta \varepsilon} \quad , \quad D_{\varepsilon}^{+} \hat{A}^{-} = \frac{\hat{A}_{i+1,j,k}^{-} - \hat{A}_{i,j,k}^{-}}{\Delta \varepsilon} \quad , \quad (2.30)$$

A^{+} and A^{-} are constructed as follows:

$$A^{+} = R_{\varepsilon} \Lambda_{\varepsilon}^{+} L_{\varepsilon} \quad , \quad A^{-} = R_{\varepsilon} \Lambda_{\varepsilon}^{-} L_{\varepsilon} \quad , \quad (2.31)$$

$D_{\eta}^{-}, D_{\zeta}^{-}, D_{\eta}^{+}, D_{\zeta}^{+}, B^{+}, C^{+}, B^{-}$ and C^{-} were constructed using the same approach as Eq. (2.30) and Eq. (2.31).

$$\left[I + \frac{\partial \hat{A}}{\partial \varepsilon} + \frac{\partial \hat{B}}{\partial \eta} + \frac{\partial \hat{C}}{\partial \zeta} \right]^m \Delta \hat{Q} = L + D + U \quad , \quad (2.32)$$

where L represents the lower triangle matrix, U as the upper triangle matrix , and D as diagonal terms.

$$\begin{aligned} L &= -\frac{\hat{A}_{i-1,j,k}^{+}}{\Delta \varepsilon} - \frac{\hat{B}_{i,j-1,k}^{+}}{\Delta \eta} + \frac{\hat{C}_{i,j,k-1}^{+}}{\Delta \zeta} \quad , \\ D &= \hat{I} + \frac{\hat{A}_{i,j,k}^{+}}{\Delta \varepsilon} - \frac{\hat{A}_{i,j,k}^{-}}{\Delta \varepsilon} + \frac{\hat{B}_{i,j,k}^{+}}{\Delta \eta} - \frac{\hat{B}_{i,j,k}^{-}}{\Delta \eta} + \frac{\hat{C}_{i,j,k}^{+}}{\Delta \zeta} - \frac{\hat{C}_{i,j,k}^{-}}{\Delta \zeta} \quad , \\ U &= \frac{\hat{A}_{i+1,j,k}^{-}}{\Delta \varepsilon} - \frac{\hat{B}_{i,j+1,k}^{-}}{\Delta \eta} - \frac{\hat{C}_{i,j,k+1}^{-}}{\Delta \zeta} \quad , \end{aligned} \quad (2.33)$$

$L+D+U$ can be approximated as follows:

$$L + D + U = (L + D)D^-(D + U) - LD^-U \approx (L + D)D^-(D + U) , \quad (2.34)$$

where

$$\begin{aligned} L + D &= \hat{I} + D_\varepsilon^- \hat{A}^+ + D_\eta^- \hat{B}^+ + D_\zeta^- \hat{C}^+ - \hat{A}^- - \hat{B}^- - \hat{C}^- , \\ D &= \hat{I} + \hat{A}^+ - \hat{A}^- + \hat{B}^+ - \hat{B}^- + \hat{C}^+ - \hat{C}^- , \\ D + U &= \hat{I} + D_\varepsilon^- \hat{A}^- + D_\eta^- \hat{B}^- + D_\zeta^- \hat{C}^- - \hat{A}^+ - \hat{B}^+ - \hat{C}^+ . \end{aligned} \quad (2.35)$$

By substituting Eq. (2.34) into Eq. (2.29), we can obtain the following relation.

$$(L + D) \underbrace{D^-(D + U)}_{\Delta \hat{Q}^*} = RHS . \quad (2.36)$$

The above equation (Eq. (2.36)) can be solved via two approaches. Firstly, via forward sweep, this can be explained in relation (2.37);

$$\Delta \hat{Q}_{i,j,k}^* = D \left[RHS + (\hat{A}^+ \Delta \hat{Q}^*)_{i-1,j,k} + (\hat{B}^+ \Delta \hat{Q}^*)_{i,j-1,k} + (\hat{C}^+ \Delta \hat{Q}^*)_{i,j,k-1} \right]. \quad (2.37)$$

Secondly, via backward sweep, this can be explained by Eq. (2.38);

$$\Delta \hat{Q}_{i,j,k}^* = \Delta \hat{Q}_{i,j,k}^* - D^{-1} \left[(\hat{A}^- \Delta \hat{Q}^*)_{i+1,j,k} + (\hat{B}^- \Delta \hat{Q}^*)_{i,j+1,k} + (\hat{C}^- \Delta \hat{Q}^*)_{i,j,k+1} \right]. \quad (2.38)$$

This sweep was carried out on the plane at which $i+j+k = \text{constant}$, where \hat{Q} (iplane, ipoint) = $\hat{Q}(i,j,k)$ [50][51]. The superscript “+” represents non-negative Jacobian and “-” represents non-positive Jacobian as shown in Eq. (2.39).

$$\hat{A}^\pm \approx \frac{1}{2} [\hat{A} \pm \tilde{\rho}(\hat{A})I] , \quad (2.39)$$

where

$$\tilde{\rho}(\hat{A}) = \sigma \max[|\lambda(\hat{A})|] = \sigma \left[|U| + c \sqrt{\varepsilon_x^2 + \eta_y^2 + \zeta_z^2} \right] . \quad (2.40)$$

So that, the respective diagonal terms can be simplified as Eq. (2.41);

$$\begin{aligned} D &= [\hat{I} + \hat{A}_{i,j,k}^+ - \hat{A}_{i,j,k}^- + \hat{B}_{i,j,k}^+ - \hat{B}_{i,j,k}^- + \hat{C}_{i,j,k}^+ - \hat{C}_{i,j,k}^-] \\ &= I + [\tilde{\rho}(\hat{A}) + \tilde{\rho}(\hat{B}) + \tilde{\rho}(\hat{C})]I . \end{aligned} \quad (2.41)$$

The explanation of viscous Jacobian approximation and LU-SGS with dual time method can be found in [51][52]. The matrix-free method was adopted in the present work as follows:

$$\begin{aligned} \hat{A}^\pm \Delta \hat{Q} &\approx (\hat{A} \pm \tilde{\rho} \hat{l}) \Delta \hat{Q} = \hat{A} \Delta \hat{Q} \pm \tilde{\rho} \Delta \hat{Q} = \Delta \hat{E} \pm \tilde{\rho} \Delta \hat{Q} \\ &= [\hat{E}(Q + \Delta Q) - \hat{E}(Q)] \pm \tilde{\rho} \Delta \hat{Q} . \end{aligned} \quad (2.42)$$

2.3.3 INVISCID FLUX

There are two methods to solve inviscid fluxes, which are: central difference scheme, and upwind scheme. Central difference scheme principally requires numerical viscosity for numerical instability. In contrast, upwind scheme does not require this numerical viscosity. Upwind scheme has two approaches of calculation method: flux vector splitting, and flux difference splitting. In this calculation, the accuracy of the scheme has been improved by using MUSCL method (2nd order accuracy).

2.3.3.1 AUSM (ADVECTION UPSTREAM SPLITTING METHOD) SCHEME

AUSM is a flux vector splitting upwind scheme, used to estimate the inviscid flux at the cell interface, so that the inviscid flux vector on left and right of this interface can be determined [53][54][55]. The inviscid flux has been estimated first on the cell

interface ξ direction. The amplitude “ Sa^ξ ” is used to generalize the speed of sound from a Cartesian coordinate to a generalized coordinate system.

$$Sa^\xi = \sqrt{\varepsilon_x^2 + \varepsilon_y^2 + \varepsilon_z^2} \quad , \quad (2.43)$$

contravariant velocities on the left, U_L and right, U_R can be estimated as follows:

$$U_R = \varepsilon_x u_R + \varepsilon_y v_R + \varepsilon_z w_R \quad , \quad (2.44)$$

$$U_L = \varepsilon_x u_L + \varepsilon_y v_L + \varepsilon_z w_L \quad . \quad (2.45)$$

Mach number in the coordinate system for right, M_R and left, M_L of the interface can be estimated using Eq. (2.46);

$$M_R = \frac{U_R}{Sa^\xi c_R} \quad , \quad M_L = \frac{U_L}{Sa^\xi c_L} \quad . \quad (2.46)$$

Mach number and pressure at the interface can be estimated as follows;

$$M_{1/2} = M^+ + M^- \quad , \quad p_{1/2} = p^+ + p^- \quad , \quad |M_{1/2}| = M^+ + M^- \quad , \quad (2.47)$$

where

$$M^+ = \begin{cases} \frac{1}{4}(M_L + 1)^2, & \text{if } |M_L| \leq 1 \\ \frac{1}{2}(M_L + |M_L|), & \text{others} \end{cases} \quad (2.48)$$

$$p^+ = \begin{cases} \frac{1}{4}(M_L + 1)^2 p_L (2 - M_L), & \text{if } |M_L| \leq 1 \\ p_L \frac{M^+}{M_L}, & \text{others} \end{cases}$$

$$\begin{aligned}
M &= \begin{cases} \frac{1}{4}(M_R + 1)^2, & \text{if } |M_R| \leq 1 \\ \frac{1}{2}(M_R + |M_R|), & \text{others} \end{cases} \\
p^+ &= \begin{cases} \frac{1}{4}(M_R + 1)^2 p_R (2 - M_R), & \text{if } |M_R| \leq 1 \\ p_R \frac{M}{M_R}, & \text{others} \end{cases} .
\end{aligned} \tag{2.49}$$

Finally, the inviscid flux at the interface can be estimated by relation (2.50).

$$\begin{aligned}
\hat{E}_{\frac{1}{2}} &= \frac{1}{2} Sa^\varepsilon M_{\frac{1}{2}} \left\{ \begin{bmatrix} \rho_L c_L \\ \rho u_L c_L \\ \rho v_L c_L \\ \rho w_L c_L \\ \rho_L h_L c_L \end{bmatrix} + \begin{bmatrix} \rho_R c_R \\ \rho u_R c_R \\ \rho v_R c_R \\ \rho w_R c_R \\ \rho_R h_R c_R \end{bmatrix} \right\} \\
&- \frac{1}{2} Sa^\varepsilon M_{\frac{1}{2}} \left\{ \begin{bmatrix} \rho_L c_L \\ \rho u_L c_L \\ \rho v_L c_L \\ \rho w_L c_L \\ \rho_L h_L c_L \end{bmatrix} + \begin{bmatrix} \rho_R c_R \\ \rho u_R c_R \\ \rho v_R c_R \\ \rho w_R c_R \\ \rho_R h_R c_R \end{bmatrix} \right\} + \begin{bmatrix} 0 \\ \varepsilon_x p_{\frac{1}{2}} \\ \varepsilon_y p_{\frac{1}{2}} \\ \varepsilon_z p_{\frac{1}{2}} \\ 0 \end{bmatrix} .
\end{aligned} \tag{2.50}$$

In η and ζ directions, $\hat{F}_{1/2}$ and $\hat{G}_{1/2}$ can be obtained by replacing $\xi_x, \xi_y, \xi_z, \eta_x, \eta_y, \eta_z$ and $\zeta_x, \zeta_y, \zeta_z$ respectively.

2.3.3.2 ROE SCHEME

Roe scheme [56][57] is a flux difference splitting upwind scheme. The Roe scheme is an approximation of exact Riemann solver (Godunov scheme).

2.3.4 METRICS, JACOBIAN AND GEOMETRICAL QUANTITIES

The relations between face vectors and metrics are

$$S^\varepsilon = J^{-1}\nabla\varepsilon = J^{-1} \begin{bmatrix} \varepsilon_x \\ \varepsilon_y \\ \varepsilon_z \end{bmatrix}, \quad S^\eta = J^{-1}\nabla\eta = J^{-1} \begin{bmatrix} \eta_x \\ \eta_y \\ \eta_z \end{bmatrix}, \quad S^\zeta = J^{-1}\nabla\zeta = J^{-1} \begin{bmatrix} \zeta_x \\ \zeta_y \\ \zeta_z \end{bmatrix}, \quad (2.51)$$

Several forms of face vector estimation [56][58][59] can presented as follows;

$$\begin{aligned} S_{i,j,k}^\varepsilon &= \frac{1}{8} (r_{i,j+1,k+1} - r_{i,j-1,k-1}) \times (r_{i,j-1,k+1} - r_{i,j+1,k-1}), \\ S_{i,j,k}^\eta &= \frac{1}{8} (r_{i+1,j,k+1} - r_{i-1,j,k-1}) \times (r_{i-1,j,k+1} - r_{i+1,j,k-1}), \\ S_{i,j,k}^\zeta &= \frac{1}{8} (r_{i+1,j+1,k} - r_{i-1,j-1,k}) \times (r_{i-1,j+1,k} - r_{i+1,j-1,k}). \end{aligned} \quad (2.52)$$

The reciprocal of the Jacobian is equivalent to the cell volume and can be obtained by the following relation:

$$J^{-1} = V = V_1 + V_2 + V_3, \quad (2.53)$$

where

$$\begin{aligned} V_1 &= \frac{1}{12} (S_{i+1,j,k}^\varepsilon + S_{i-1,j,k}^\varepsilon) \times (r_{i+1,j+1,k+1} - r_{i-1,j-1,k-1}), \\ V_2 &= \frac{1}{12} (S_{i,j+1,k}^\eta + S_{i,j-1,k}^\eta) \times (r_{i+1,j+1,k+1} - r_{i-1,j-1,k-1}), \\ V_3 &= \frac{1}{12} (S_{i+1,j,k}^\zeta + S_{i-1,j,k}^\zeta) \times (r_{i+1,j+1,k+1} - r_{i-1,j-1,k-1}). \end{aligned} \quad (2.54)$$

2.4 BOUNDARY CONDITIONS

Improper implementation of a boundary condition may lead to a less accurate result in numerical solution. Since turbomachinery calculation may involve isentropic flow, special treatment is needed, especially at the inlet and the outlet. So, in this calculation code, total pressure and total temperature at the inlet, and static pressure at the exit, have been specified.

2.4.1 INLET BOUNDARY CONDITIONS

Imposed boundary conditions at the turbine inlet are total pressure, $P_{01} = 140,000\text{Pa}$ and total temperature, $T_{01} = 280\text{K}$, respectively. For the inlet boundary condition, subsonic Riemann Invariant condition, R_{01} has been imposed, where [53];

$$R_{01} = \vec{V}_{in}\vec{n} - 2 \left[\frac{c_{in}}{\gamma - 1} \right]. \quad (2.55)$$

\vec{V}_{in} is velocity vector and \vec{n} is normal vector on the inlet plane. With this, we can calculate the velocity V_{01}

$$V_{01} = \frac{-R_{01} - (\gamma - 1)}{(\gamma - 1)\cos^2\theta + 2} \{1 + \cos\theta\sqrt{A_1 - A_2}\}, \quad (2.56)$$

where;

$$A_1 = \frac{[(\gamma - 1)\cos^2\theta + 2]c_0^2}{(\gamma - 1)R_{01}^2} \quad \text{and} \quad A_2 = \left[\frac{\gamma - 1}{2} \right], \quad (2.57)$$

where θ is the flow angle relative to the inlet boundary [53]. The speed of sound at stagnation condition, c_0 can be obtained by

$$c_0 = c_{in}^2 + \frac{\gamma - 1}{2} (\vec{V}_{in})^2. \quad (2.58)$$

2.4.2 OUTLET BOUNDARY CONDITIONS

At the outlet, $M_{is,02} = 0.79$ and the Reynolds number is 2.8×10^6 , which is the same as in references [71][72]. To achieve this condition, the outlet pressure is specified as $P_{02} = 92,755 \text{ Pa}$ (Eq. (2.59)). Based on this condition, $P_{s,02}$ and $T_{s,02}$ have been calculated via isentropic Mach number relation;

$$P_{s,02} = P_{01} \left(1 + \frac{\gamma - 1}{2} M_{is,02}^2 \right)^{-\left(\frac{\gamma}{\gamma-1}\right)}, \quad (2.59)$$

$$T_{s,02} = T_{01} \left(1 + \frac{\gamma - 1}{2} M_{is,02}^2 \right)^{-1}. \quad (2.60)$$

At the outlet, the static pressure has been prescribed. Subsonic outlet boundary condition and entropy relation have been imposed, which has been calculated by Eq. (2.60), so

$$R_{02} = \overline{V}_{in} \vec{n} + 2 \left[\frac{c_{in}}{\gamma - 1} \right], \quad (2.61)$$

where the outlet pressure has been specified (in dimensionless form), so the density, ρ_{02} and velocity V_{02} can be obtained by;

$$\rho_{02} = \left[\frac{P_{02}}{P_{in}} \right]^{\left(\frac{1}{\gamma}\right)}, \quad (2.62)$$

$$V_{02} = R_{02} - 2 \left[\frac{c_{02}}{\gamma - 1} \right]. \quad (2.63)$$

2.4.3 WALL BOUNDARY CONDITIONS

On the blade surface, a non-slip adiabatic wall boundary condition is applied, where the velocity at the wall is equal to zero.

$$u = v = w = 0. \quad (2.64)$$

2.4.4 PERIODICAL BOUNDARY CONDITIONS

Translational periodical boundary condition is applied for this calculation as in previous studies [18][60][61]. Since the simulation of the blade consists of several other

cascades, single blade calculation will be challenging. Several boundary conditions have been tested, including farfield and symmetrical boundary conditions, but the results are not consistent with the reference. Finally, average condition is used in periodic boundary condition, which has given a result that is in good agreement with the experiment.

2.5 TURBULENCE MODEL

Reynolds Average Navier Stokes (RANS) equations contain the Reynolds stress tensor ($-\rho u_i' u_j'$) which is normally governed with another equation to solve it. Eddy viscosity is replaced into Reynolds stress as;

$$\begin{aligned} \mu &= \mu_{laminar} + \mu_{turbulent} \\ k &= k_{laminar} + k_{turbulent} = c_p \left[\frac{\mu_{laminar}}{Pr_{laminar}} + \frac{\mu_{turbulent}}{Pr_{turbulent}} \right] \end{aligned} \quad (2.65)$$

$\mu_{turbulent}$ can be estimated by means of a turbulence model. Several turbulence models have undergone investigation in this numerical calculation. Since the scope of this study has been limited to one equation turbulence model, four turbulence models were tested, which are Spalart Allmaras (SA), Detached Eddy Simulation (DES), Delay Detached Eddy Simulation (DDES) and Improved Delay Detached Eddy Simulation (IDDES) turbulence models [62][63][64][65].

2.5.1 SPALART-ALLMARAS TURBULENCE MODEL (SA)

Although Spalart-Allmaras is one of a number of equation turbulence models, it provides reasonably accurate prediction [53]. The Spalart Allmaras model is a transport equation model for eddy viscosity. Eq. (2.66) is the transport equation for eddy viscosity, $\tilde{\nu}$.

$$\frac{D\tilde{\nu}}{Dt} = \underbrace{c_{b1}\tilde{S}\tilde{\nu}}_{Production} + \underbrace{\frac{1}{\sigma}[\nabla \cdot ((\mathbf{v} + \tilde{\nu})\nabla\tilde{\nu}) + c_{b2}(\nabla\tilde{\nu})^2]}_{Diffusion} - \underbrace{c_{w1}f_w\left(\frac{\tilde{\nu}}{d}\right)^2}_{Destruction} . \quad (2.66)$$

“ d ” is distance from the wall to the nearest field point (nearest meshing layer). The explanation of production terms is as follows:

$$\begin{aligned} \tilde{S} &= f_{v3}S + \frac{\tilde{\nu}}{\kappa^2 d^2} f_{v2} \\ S &= \sqrt{2\Omega_{ijk}\Omega_{ijk}} \\ \Omega_{ij} &= \frac{1}{2} \left[\frac{\partial u_i}{\partial x_j} - \frac{\partial u_j}{\partial x_i} \right] \\ f_{v2} &= 1 - \frac{x}{1 + f_{v1}}, \quad f_{v3} = 1 \end{aligned} \quad (2.67)$$

also, there is a modification for f_{v2} in order to avoid negative \tilde{S} , as shown in Eq. (2.68).

$$f_{v2} = \left[1 + \frac{X}{1 + c_{v2}} \right]^{-3}, \quad f_{v3} = \frac{(1 + Xf_{v1})(1 - f_{v2})}{\max(x, 0.001)}. \quad (2.68)$$

Furthermore, the explanation of the destruction term is

$$f_w = g \left[\frac{1 + c_{w3}^6}{g^6 + c_{w3}^6} \right]^{\frac{1}{6}}, \quad g = r + c_{w2}(r^6 - r), \quad r = \frac{\tilde{\nu}}{\tilde{S}\kappa^2 d^2}. \quad (2.69)$$

The absolute turbulent viscosity can be calculated as;

$$\mu_T = \rho\tilde{\nu}f_{v1}, \quad (2.70)$$

where

$$f_{v1} = \frac{X^3}{X^3 + c_{v1}^3}, \quad X = \frac{\tilde{v}}{\nu} . \quad (2.71)$$

All constants are listed in Table 2.1.

Table 2.1. All Constants in Spalart Allmaras Turbulence Model

Constant	Value	Constant	Value
c_{b1}	0.135	k	0.41
c_{b2}	0.622	c_{w1}	$\frac{c_{b1}}{k^2} + \frac{1 + c_{b2}}{\sigma}$
c_{v1}	7.1	c_{w2}	0.3
c_{v2}	5	c_{w3}	2
σ	2/3		

For dimensionless form of Spalart Allmaras relation;

$$\frac{D\tilde{v}}{Dt} = c_{b1}\tilde{S}\tilde{v} + \frac{1}{\sigma Re_\infty} [\nabla \cdot ((\nu + \tilde{v})\nabla\tilde{v}) + c_{b2}(\nabla\tilde{v})^2] - \frac{1}{Re_\infty} c_{w1}f_w \left(\frac{\tilde{v}}{d}\right)^2, \quad (2.72)$$

and,

$$\tilde{S} = f_{v3}S + \frac{f_{v2}\tilde{v}}{Re_\infty \kappa^2 d^2}, \quad r = \frac{\tilde{v}}{Re_\infty \tilde{S} \kappa^2 d^2}. \quad (2.73)$$

The equation was cast in conservative form to be similar to Navier-Stokes equations. This can be done by multiplying Eq. (2.73) with ρ which eases the programming purpose.

$$\rho \frac{D\tilde{v}}{Dt} = \rho c_{b1}\tilde{S}\tilde{v} + \frac{1}{\sigma Re_\infty} [\nabla \cdot ((\nu + \tilde{v})\nabla\tilde{v}) + c_{b2}(\nabla\tilde{v})^2] - \frac{1}{Re_\infty} c_{w1}f_w \left(\frac{\tilde{v}}{d}\right)^2, \quad (2.74)$$

where $\rho \frac{D\tilde{v}}{Dt}$ can be represented by;

$$\rho \frac{D\tilde{v}}{Dt} = \rho \frac{d\tilde{v}}{dt} + \rho V + \nabla \tilde{v} . \quad (2.75)$$

On the other hand, the conventional conservative form is:

$$\begin{aligned} \frac{D\rho\tilde{v}}{Dt} &= \frac{d\rho\tilde{v}}{dt} + \rho V + \nabla(\rho V\tilde{v}) \\ &= \rho \frac{d\tilde{v}}{dt} + \tilde{v} \frac{d\rho}{dt} + \rho V \cdot \nabla \tilde{v} + \tilde{v} \nabla \rho V \\ &= \rho \frac{d\tilde{v}}{dt} + \tilde{v} \frac{d\rho}{dt} + \tilde{v} \underbrace{\left[\frac{d\rho}{dt} + \nabla \rho V \right]}_{0=\text{continuity}} . \end{aligned} \quad (2.76)$$

As a result, both forms are equal, so the diffusion term can be rearranged as follows:

$$\begin{aligned} \nabla \cdot ((v + \tilde{v}) \nabla \tilde{v}) + c_{b2} (\nabla \tilde{v})^2 \\ \Rightarrow (1 + c_{b2}) \nabla \cdot ((v + \tilde{v}) \nabla \tilde{v}) - c_{b2} (v + \tilde{v}) \nabla^2 \tilde{v}. \end{aligned} \quad (2.77)$$

The transport equation in Cartesian non-dimensional conservative form can be written as follows:

$$\begin{aligned} \frac{\partial \rho \tilde{v}}{\partial t} &= \frac{\partial \rho \tilde{v} u}{\partial x} + \frac{\partial \rho \tilde{v} v}{\partial y} + \frac{\partial \rho \tilde{v} w}{\partial z} = \rho c_{b1} \tilde{S} \tilde{v} - \frac{\rho}{Re_\infty} c_{w1} f_w \left(\frac{\tilde{v}}{d} \right)^2 \\ &+ \frac{\rho(1 + c_{b2})}{\sigma Re_\infty} \left[\frac{\partial}{\partial x} \left[(v + \tilde{v}) \frac{\partial \tilde{v}}{\partial x} \right] + \left[\frac{\partial}{\partial y} \left[(v + \tilde{v}) \frac{\partial \tilde{v}}{\partial y} \right] + \left[\frac{\partial}{\partial z} \left[(v + \tilde{v}) \frac{\partial \tilde{v}}{\partial z} \right] \right] \right] \\ &- \frac{\rho c_{b2}}{\sigma Re_\infty} \left[\left[(v + \tilde{v}) \frac{\partial^2 \tilde{v}}{\partial x^2} \right] + \left[\left[(v + \tilde{v}) \frac{\partial^2 \tilde{v}}{\partial y^2} \right] + \left[\left[(v + \tilde{v}) \frac{\partial^2 \tilde{v}}{\partial z^2} \right] \right] \right]. \end{aligned} \quad (2.78)$$

To deal with arbitrary geometry, Eq. (2.78) was transformed from Cartesian coordinate system to generalized coordinate system.

$$\begin{aligned} \frac{\partial J^{-1}\rho\tilde{v}}{\partial t} &= \frac{\partial J^{-1}\rho\tilde{v}u}{\partial \varepsilon} + \frac{\partial J^{-1}\rho\tilde{v}v}{\partial \eta} + \frac{\partial J^{-1}\rho\tilde{v}w}{\partial \zeta} = \text{prod} - \text{dest} \\ &+ \frac{1}{Re_\infty} \left[A \frac{\partial \tilde{F}_{v1}}{\partial \varepsilon} - B \frac{\partial \tilde{F}_{v2}}{\partial \varepsilon} + A \frac{\partial \tilde{E}_{v1}}{\partial \eta} - B \frac{\partial \tilde{E}_{v2}}{\partial \eta} + A \frac{\partial \tilde{G}_{v1}}{\partial \zeta} - B \frac{\partial \tilde{G}_{v2}}{\partial \zeta} \right]. \end{aligned} \quad (2.79)$$

The left hand side of Eq. (2.79) represents the convective terms, and the third term on the right hand side represents diffusive terms, which are expressed as follows:

$$\begin{aligned} \tilde{F}_{v1} &= J^{-1}[\varepsilon_x F_{v1} + \varepsilon_y E_{v1} + \varepsilon_z G_{v1}] \quad , \\ \tilde{F}_{v2} &= J^{-1}[\varepsilon_x F_{v2} + \varepsilon_y E_{v2} + \varepsilon_z G_{v2}] \quad , \\ \tilde{E}_{v1} &= J^{-1}[\eta_x F_{v1} + \eta_y E_{v1} + \eta_z G_{v1}] \quad , \\ \tilde{E}_{v2} &= J^{-1}[\eta_x F_{v2} + \eta_y E_{v2} + \eta_z G_{v2}] \quad , \\ \tilde{G}_{v1} &= J^{-1}[\zeta_x F_{v1} + \zeta_y E_{v1} + \zeta_z G_{v1}] \quad , \\ \tilde{G}_{v2} &= J^{-1}[\zeta_x F_{v2} + \zeta_y E_{v2} + \zeta_z G_{v2}] \quad , \end{aligned} \quad (2.80)$$

where

$$\begin{aligned} F_{v1} &= (v + \tilde{v}) \frac{\partial \tilde{v}}{\partial x}, & E_{v1} &= (v + \tilde{v}) \frac{\partial \tilde{v}}{\partial y}, & G_{v1} &= (v + \tilde{v}) \frac{\partial \tilde{v}}{\partial z}, \\ F_{v2} &= \frac{\partial \tilde{v}}{\partial x}, & E_{v2} &= \frac{\partial \tilde{v}}{\partial y}, & G_{v2} &= \frac{\partial \tilde{v}}{\partial z}, \\ A &= \frac{\rho(1 + c_{b,2})}{\sigma}, & B &= \frac{\rho c_{b,2}(v + \tilde{v})}{\sigma}, & f_{v2} &= \frac{1}{(1 + x/c_{v2})^3} \end{aligned} \quad (2.81)$$

Production term (Prod.) and Destruction term (Dest.) are defined by

$$\text{Prod} = \rho c_{b,1} \tilde{S} \tilde{v} = P \tilde{v}, \quad \text{Dest} = \frac{1}{Re_\infty} \rho c_{w1} f_w \left(\frac{\tilde{v}}{d} \right)^2 \quad (2.82)$$

The Jacobian is needed in order to solve Eq. (2.82).

$$\mathbf{Jacobian} = \mathbf{D} - \mathbf{P} = \mathbf{pos}[\mathbf{D} - \mathbf{P}] + \mathbf{pos}[\mathbf{D}' - \mathbf{P}']\tilde{\mathbf{v}} \quad , \quad (2.83)$$

where

$$\mathbf{pos}(x) = \begin{cases} \mathbf{x}, & \text{if } x \geq 0 \\ \mathbf{0}, & \text{if } x < 0 \end{cases} \quad . \quad (2.84)$$

The prime "" refers to derivative to $\tilde{\mathbf{v}}$

$$\tilde{\mathbf{S}}' = \frac{\mathbf{1}}{\kappa^2 d^2 Re_\infty} \left[\mathbf{f}_{v2} - \frac{3X}{c_{v2}} \left(\mathbf{1} + \frac{X}{c_{v2}} \right)^{-4} \right] \quad . \quad (2.85)$$

The derivative of " \mathbf{P} " is as follows:

$$\mathbf{P}' = \rho c_{b1} \tilde{\mathbf{S}}' \quad , \quad (2.86)$$

and the derivative of " \mathbf{D} " can be obtained by Eq. (2.87)

$$\mathbf{D}' = \frac{\rho c_{b1}}{d^2 Re_\infty} [\mathbf{f}_{w1} + \tilde{\mathbf{v}} \mathbf{f}'_w] \quad , \quad (2.87)$$

where

$$\begin{aligned} \frac{\partial \mathbf{f}_w}{\partial \tilde{\mathbf{v}}} &= \frac{\partial \mathbf{f}_w}{\partial \mathbf{g}} \frac{\partial \mathbf{g}}{\partial r} \frac{\partial r}{\partial \tilde{\mathbf{v}}} \quad , \\ \frac{\partial r}{\partial \tilde{\mathbf{v}}} &= \frac{r}{\tilde{\mathbf{v}}} \left(\mathbf{1} - \tilde{\mathbf{v}} \frac{\tilde{\mathbf{S}}'}{\mathbf{S}} \right) \quad , \\ \frac{\partial \mathbf{g}}{\partial r} &= \mathbf{1} + c_{w2} (6r^5 - 1) \quad , \end{aligned} \quad (2.88)$$

$$\frac{\partial f_w}{\partial g} = \frac{f_w}{g} \left(1 - \frac{g^6}{g^6 + c_{w3}^6} \right) .$$

Equation (2.79) is close to NS equations and can be solved using *LUSGS*. In Eq. (2.79), RHS includes the source term, i.e. Prod.-Dest. Solution of Eq. (2.89) presented the solution for one-dimensional and the addition of (ξ and η) for two-dimensional and (ξ , η and ζ) for three-dimensional.

$$L = \bar{M}_{i-1}^{(1)} + \bar{M}_{i-1}^{(2)} , \quad (2.89)$$

where

$$\begin{aligned} \bar{M}_{i-1}^{(1)} &= \mathbf{0.5}(U + |U|)_{i-1} + c_{i-1} S a_{i-\frac{1}{2}}^\varepsilon , \\ \bar{M}_{i-1}^{(2)} &= \left[(\mathbf{1} + c_{b2})(\tilde{v} + v)_{i-1/2} - c_{b2}(\tilde{v} + v)_i \right] \frac{\rho_{i-1} S a_{i-1/2}^\varepsilon}{\sigma R e_\infty} . \end{aligned} \quad (2.90)$$

The upper triangular matrix can be calculated as follows:

$$U = \bar{M}_{i+1}^{(1)} + \bar{M}_{i+1}^{(2)} , \quad (2.91)$$

where

$$\begin{aligned} \bar{M}_{i+1}^{(1)} &= \mathbf{0.5}(U + |U|)_{i+1} + c_{i+1} S a_{i+\frac{1}{2}}^\varepsilon , \\ \bar{M}_{i+1}^{(2)} &= \left[(\mathbf{1} + c_{b2})(\tilde{v} + v)_{i+1/2} - c_{b2}(\tilde{v} + v)_i \right] \frac{\rho_{i+1} S a_{i+1/2}^\varepsilon}{\sigma R e_\infty} . \end{aligned} \quad (2.92)$$

The diagonal elements can be calculated as follows:

$$D = \bar{M}_i^{(1)} + \bar{M}_i^{(2)} + \mathbf{Jacobian} , \quad (2.93)$$

where

$$\begin{aligned}
\bar{M}_i^{(1)} &= [\mathbf{0.5}(U + |U|)_i + c_i S a_i^\varepsilon] - [\mathbf{0.5}(U - |U|)_i - c_i S a_i^\varepsilon] \\
\bar{M}_i^{(2)} &= (\mathbf{1} + c_{b2})(\tilde{v} + v)_{i-\frac{1}{2}} S a_{i-\frac{1}{2}}^\varepsilon + (\mathbf{1} + c_{b2})(\tilde{v} + v)_{i+\frac{1}{2}} S a_{i+\frac{1}{2}}^\varepsilon \\
&= -c_{b2}(\tilde{v} + v)_i \left(S a_{i-\frac{1}{2}}^\varepsilon + S a_{i+\frac{1}{2}}^\varepsilon \right) \frac{\rho_i}{\sigma R e_\infty} .
\end{aligned} \tag{2.94}$$

2.5.2 DETACHED EDDY SIMULATION (DES)

DES was adopted in the present work. *DES* has been developed to deal with higher Reynold numbers and was originally formulated by Spalart et al., [64]. The *DES* turbulence model is a hybrid scheme that works as *RANS* near the wall, and works as *LES* away from the wall, including a separated boundary layer and wake. For *RANS*, the spatial Favre filtered compressible Navier-Stokes equations are used. In *LES*, the original Smagorinsky model is used for sub-grid-scale (SGS) modeling for small eddy [66][67]. As described before, the destruction part of SA turbulence model contains $[\tilde{v}/d]^2$. As this term balances the production term, so \tilde{v} becomes proportional to S and d^2 . The SGS scale, \tilde{v} together with S and grid spacing Δ , becomes ν_{SGS} proportional to $[S\Delta^2]$ [64]. So here the initial idea of *DES* becomes evident: *DES* works by replacing the length scale in the SA turbulence model d with a new length scale, \tilde{d}

$$\tilde{d} = \min(d, \Delta C_{DES}) , \tag{2.95}$$

where $\Delta = \max(\Delta_x, \Delta_y, \Delta_z)$ is local maximum grid spacing. Thus, with this new \tilde{d} , *DES* is able to control the eddy viscosity. Near the blade surface, $\tilde{d} = d$; otherwise $\tilde{d} = \Delta C_{DES}$.

2.5.3 DELAY DETACHED EDDY SIMULATION (DDES)

Because the length scale depends only on the grid spacing, problems can arise if the grid spacing (in wall-normal) is finer than boundary layer thickness [65]. In this case,

the local maximum grid spacing Δ becomes smaller than the wall distance d in the boundary layer. In order to solve this problem, *DDES* has been introduced. Since the Spalart–Allmaras model does not have an internal length scale, the parameter r_d is introduced. The *SA* model with *DDES* is defined as [65]

$$f_d = 1 - \tanh([8r_d]^3) \quad \text{where } r_d = \frac{v_T + \nu}{\sqrt{u_{ijk}u_{ijk}}\kappa^2 d^2} \quad , \quad (2.96)$$

where u_{ijk} is velocity profile in i , j and k direction and f_d is 1 in the *LES* region where $r_d \ll 1$ and zero are in the *RANS* region [65]. κ is von karman constant (0.41) and ν_T is kinematic eddy viscosity [65]. Eventually, new length scale, d_{DES} can be redefined as;

$$d_{DES} = d - f_d \max(0, d - C_{DES}\Delta) \quad . \quad (2.97)$$

For *RANS* simulation, outside of the boundary layer and separated flow region, d_{DES} behaves like classical *DES* where d_{DES} is the redefined *DES* length scale and ΔC_{DES} is an adjustable parameter that is equal to 0.65. Therefore, at the boundary layer ($f_d = 0$), d_{DES} is equal to d as in *RANS* simulation while outside of the boundary layer and separated flow region, d_{DES} is like that in classical *DES*.

2.5.4 IMPROVED DELAY DETACHED EDDY SIMULATION (IDDES)

This method has been introduced and a further improvement to *DDES* has been made. Parameter r_d is different from *DDES* method.

$$r_{d, iddes} = \frac{v_T + \nu}{\kappa^2 d^2 \max\{[\sum_{ijk} \sqrt{u_{ijk}u_{ijk}}], 10^{-10}\}} \quad . \quad (2.98)$$

The major differences of *DDES* and *IDDES* compared to others are that they require more computational cost, but at the same time are beneficial in terms of less

requirement for fine grid near the wall. As compared with *DES*, *DDES* estimates *RANS* by flow and grid size, while *DES* depends on only grid size.

CHAPTER 3

EFFECT OF MULTIPLE THROUGH-HOLES ON THE TURBINE BLADE TRAILING EDGE

3.1 INTRODUCTION

A number of studies have been devoted to improving the performance of a gas turbine by minimizing component losses such as wake loss, profile loss, secondary loss, tip clearance loss, and annulus loss [12][39]. Losses can be reduced via the optimum design of the blade geometry (shape) and by employing additional flow control techniques [13]. The turbine blade wakes have an unsteady characteristic that originates from the large-scale organized structures in vortex streets, in the form of vortex shedding. Vortex shedding contributes different loss mechanisms. The total loss from vortex shedding is generally important under high-speed conditions [3].

One of the active flow control techniques being used to suppress vortex shedding involves jets, such as plasma actuators and synthetic jets [17][23]. Optimization of the blade geometry is another way of suppressing vortex shedding. Zhou et al. [14] investigated the effect of the trailing edge thickness on vortex shedding. Dwayne et al. [15] found that a thicker trailing edge tended to increase the vortex shedding strength. Bearmen et al. [28] tested a so-called 'splitter plate' at the trailing edge.

This study proposes a method of suppressing vortex shedding by connecting the pressure side and the suction side via micro holes. In previous studies, the pressure loss of the blade was suppressed by making holes on the blade. Yangwei et al. [68] found that the total pressure loss and the passage blockage were reduced by making a suction slot on the blade. The pressure distribution on the blade has been increased by

injecting cold air through holes to cool the film [69]. The pressure along the trailing edge has been increased by making a 0.1-mm hole, connecting the suction side and the pressure side of the blade [70]. In these foregoing studies, the simulation only considered the hole as being a single point on the blade span-wise, and the location and size of the hole were not optimized. Thus, this study focuses on the effect of size and location of the multiple micro holes at the trailing edge region on wake vortex shedding.

3.2 COMPUTATIONAL METHOD

The three-dimensional, Reynolds-averaged, unsteady Navier–Stokes equation is solved. The numerical model consists of the continuity equation, three dimensional Navier-Stokes equations for compressible flow. The inviscid fluxes are discretized using the total variation diminishing scheme, and viscous fluxes are discretized using standard central differences. The configuration of the cascade is presented in Fig. 3.1, where the chord length, C , is 140 mm, axial chord length, C_{ax} , is 91.84 mm and pitch, s , is 97.44 mm. The span-wise size of the blade is 10% of the blade chord length, and trailing edge diameter, $D = 7.48$ mm. S is the length measured along the trailing edge surface line.

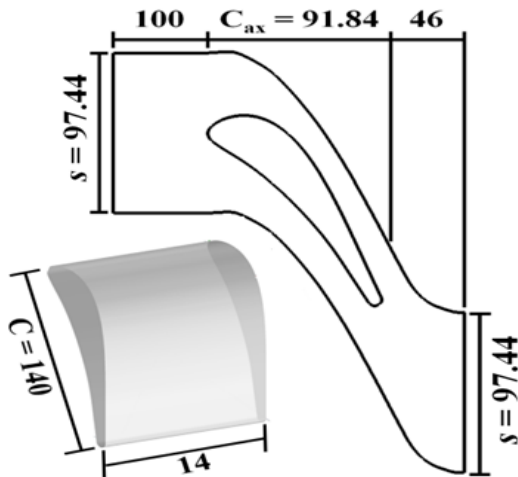


Figure 3.1: Blade configuration and dimensions (in mm)

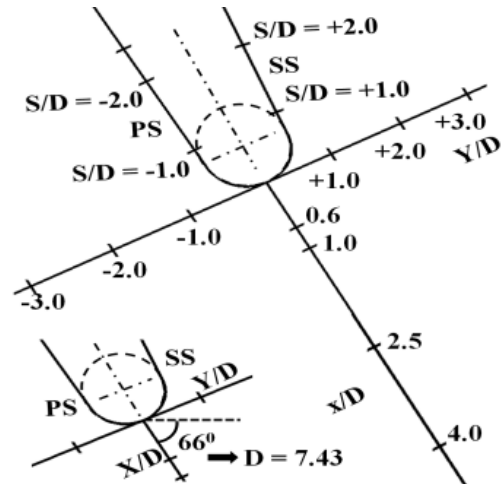


Figure 3.2: Trailing-edge S/D , x/D and Y/D reference system

The in-house code being used in this calculation is structured grid, single block, and second-order accurate in time. Roe's flux-difference splitting scheme is used for a numerical inviscid flux calculation, where second-order accuracy is achieved employing the MUSCL scheme with the van Albada flux limiter. The lower upper symmetric Gauss Seidel together with a second-order dual time stepping method is employed to calculate the unsteady flow.

Fig. 3.2 shows a close-up view of the region around the trailing edge and the definitions of x/D and Y/D . The maximum number of iterations is 2×10^6 , and there are five inner iterations for the implicit scheme (time marching). Dimensionless Δt^* is equal to 105.42×10^{-6} and the physical time step $\Delta t = 3.33 \times 10^{-7}$ s. The numerical method is validated by comparing the numerical results with experimental data obtained by Sieverding et al., [71][72] for the configuration without a hole. The Courant-Friedrichs-Lewy number is around 10.

3.2.1 BOUNDARY CONDITIONS AND TURBULENCE MODEL

Fig. 3.3 shows an O-type structured grid that has $413 \times 194 \times 50 (= 4.0 \times 10^6)$ grid points. For pre-processing, the grid has been developed via Gridgen Version 15 software. The minimum grid size is 0.002mm which is equivalent to $y^+ \approx 1$. On the blade surface, a non-slip adiabatic wall boundary condition is applied. Subscripts "01" and "02" refer to the inlet and outlet condition, while subscripts "in" and "out" represent inside and outside the calculation domain. Imposed boundary conditions at the turbine inlet are total pressure, $P_{01} = 140,000$ Pa and total temperature, $T_{01} = 280$ K, respectively. For inlet boundary condition, subsonic Riemann Invariant condition, R_{01} , has been imposed. Translational periodical boundary condition is applied for this calculation, as illustrated in Fig. 3.3 as in previous studies [18][60][61].

At the outlet, isentropic Mach number $M_{is,02} = 0.79$ and the Reynolds number is 2.8×10^6 , which is the same as references [71][72]. To achieve these conditions, the outlet total pressure is specified as $P_{02} = 92,755$ Pa. Subscript "is" refers to isentropic. At the outlet, the static pressure P_{02} has been prescribed.

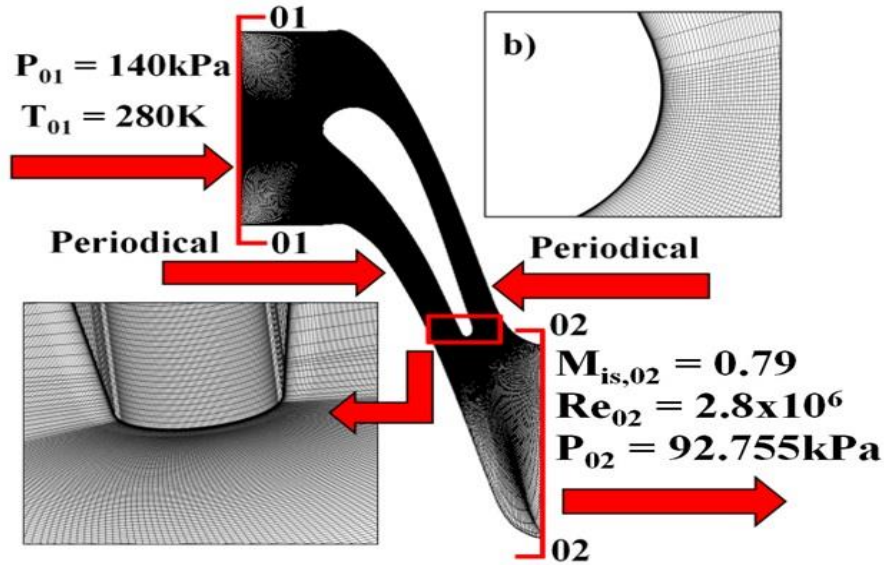


Figure 3.3: Boundary conditions and simulation grid b) Close view of grid at micro-holes area

Subsonic outlet boundary condition and entropy relation have been imposed, so subsonic Riemann Invariant condition at outlet, R_{02} can be calculated. The flow through each micro-hole is modeled using the Hagen–Poiseuille equation [70];

$$U = \frac{R^2}{4\mu} \left[-\frac{\Delta P}{\Delta L} \right], \quad (3.1)$$

where U is the velocity through the hole, R is the radius of the hole, μ is the viscosity, ΔP is the pressure difference across the micro-hole and ΔL is the tube length. This equation was not explicitly being checked since little research has been conducted using Eq. (3.1) in turbomachinery fluid dynamics research; however, it is being widely used in other research fields, i.e. morphology, and biology for calculating blood flow and capillary flow [73][74][75]. In turbine calculation, to date, this relation was first introduced by El Gendi et al. [70]. Several assumptions have been made in respect to Eq. (3.1).

First, since the hole size in this study is of micrometer size, the effect inside the hole is assumed to be laminar and incompressible. The velocity around the hole is also assumed to be uniform.

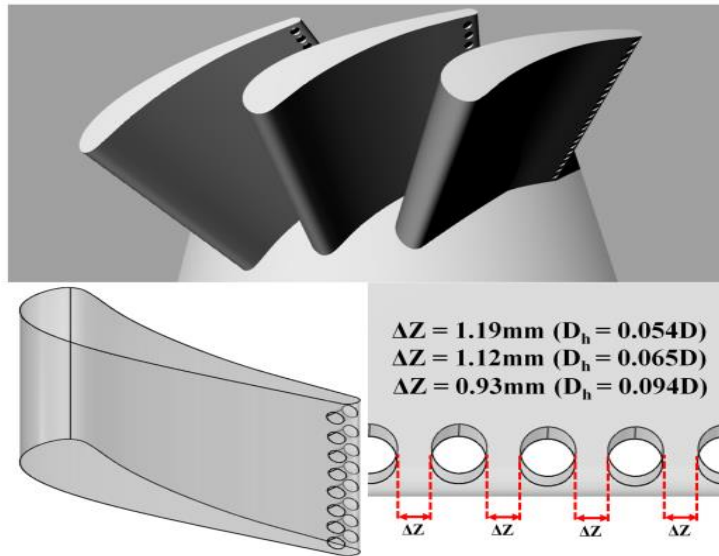


Figure 3.4: Connecting holes at the trailing edge of the blade

This U affected mass, momentum and energy conservation. After validation, the micro-hole is applied in the area of the trailing edge of the studied blade as illustrated in Fig. 3.4. The number of holes has been fixed to be eight (8) for all the cases. The number of holes has been limited to eight due to limitation of span size. Four turbulence models have been tested, which are Spalart Allamaras (*SA*), Detached Eddy Simulation (*DES*), Delay Detached Eddy Simulation (*DDES*) and Improved Delay Detached Eddy Simulation (*IDDES*) turbulence models [62][63][64][65], which were explained in Chapter 2.

3.3 RESULTS AND FINDINGS

3.3.1 CFD CODE VALIDATIONS

Each turbulence model has been compared in terms of trailing edge pressure distribution to the experimental result [71][72]. Fig. 3.5 shows the comparison result of each turbulence model. As we can see, *SA* model is not able to capture the minimal pressure as well as the others. This can be explained as in the *SA* model destruction

part; the d (distance from the wall to the nearest field point) solely depends on grid size, so if any viscous effect appears lower than Δ , the length scale needs to be modified.

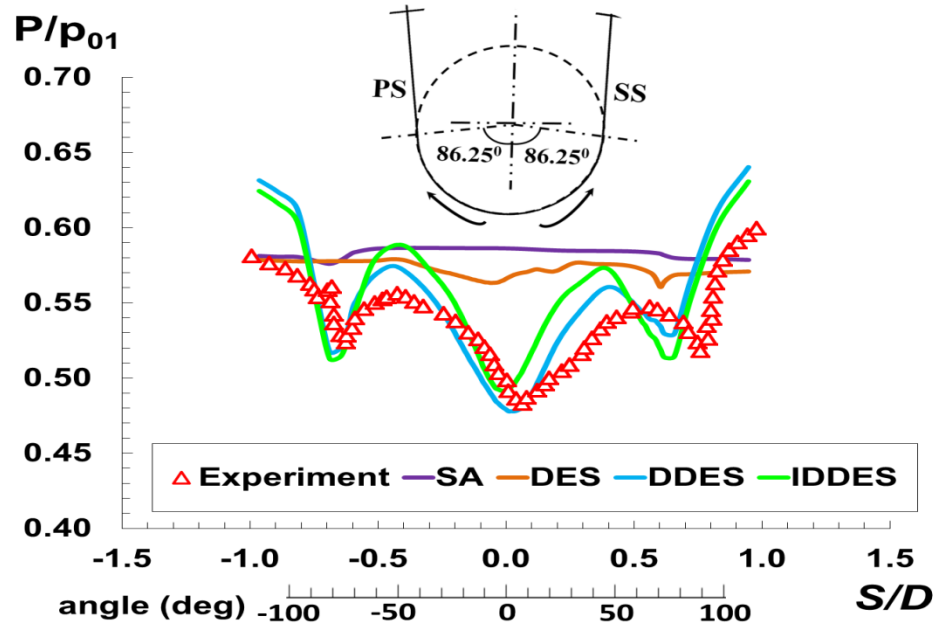


Figure 3.5: Trailing edge pressure distribution comparison among four different turbulence models and experimental data

Potsdam et al. [76] confirmed that the non-modified SA model has a problem when dealing with highly vortical flow. Therefore, it can be said that d cannot be calculated in a conventional way. As *DES* is implemented, we can see a slight improvement in capturing the pressure drop on the surface, but it is still insufficient to produce a result close to that of the experiment. However, *DDES* and *IDDES* turbulence models appear to give good results, close to the experiment. Based on this finding, *DDES* turbulence is selected to be used in this calculation, a selection which was also suggested by previous researchers [65][70][77]. Magagnato et al. [78] found that *DDES* was more capable of capturing the incipient separation in transitional flow prediction on a turbine blade as compared to *LES*, thereby supporting the choice of the *DDES* turbulence model to be applied in a turbine blade study.

The present computation produced three local minimum values of dimensionless pressure, which also appeared in the experimental results (at $S/D \approx -0.7, 0.0$ and 0.75). The locations of these minimal points and the minimum values of the computed results

agree well with the experimental results. Sieverding et al. [71] claimed that at this pressure plateau (after the pressure minima values), there are separations due to overexpansion of the suction and pressure sides. This is one of the reasons for the discrepancy between the present results and the experimental results at $|S/D| > 0.8$.

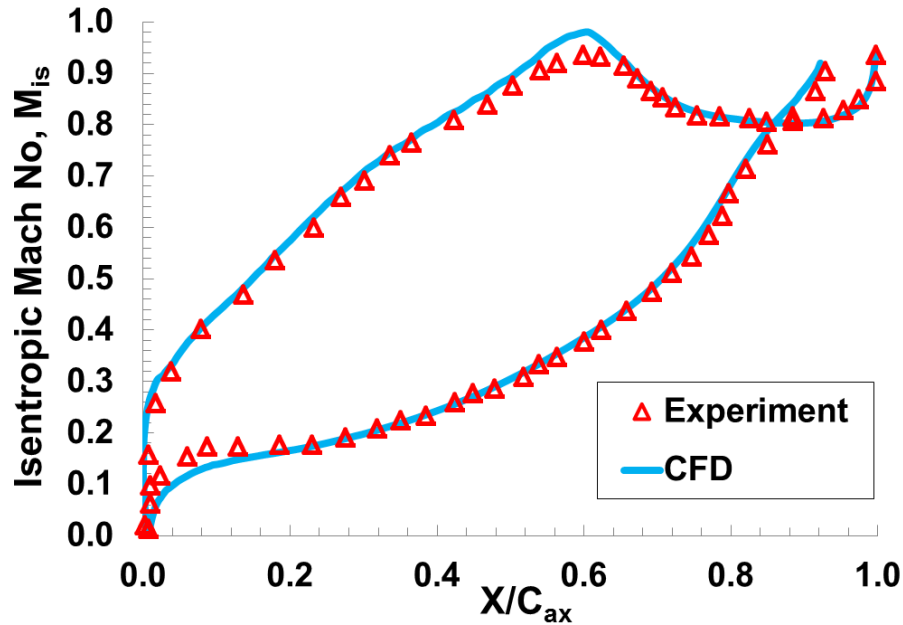


Figure 3.6: Comparison of the isentropic Mach number on the blade

Fig. 3.6 shows the isentropic Mach number. The numerical results agree well with the experimental results. In order to decide the location of the hole, we observe the flow field near the trailing edge of the blade (no hole) and the Fast Fourier Transformation (FFT) calculation has been tabulated at the respective location. FFT gives information about the dominant frequency at the location of the selected hole and indicates whether our flow calculation captured the flow field in a timely accurate manner. Friedrichs et al. [79] made holes in regions of high static pressure to reduce aerodynamic penalties. The vortices should be suppressed by making holes near the location of vortex shedding. Fig. 3.7 shows the instantaneous vorticity contour in the wake of the blade. The initial vortex shedding begins at $S/D = -0.62$. This result is consistent with Lake's [39] results that vortex shedding of the studied blade starts at about 70% of the normalized axial.

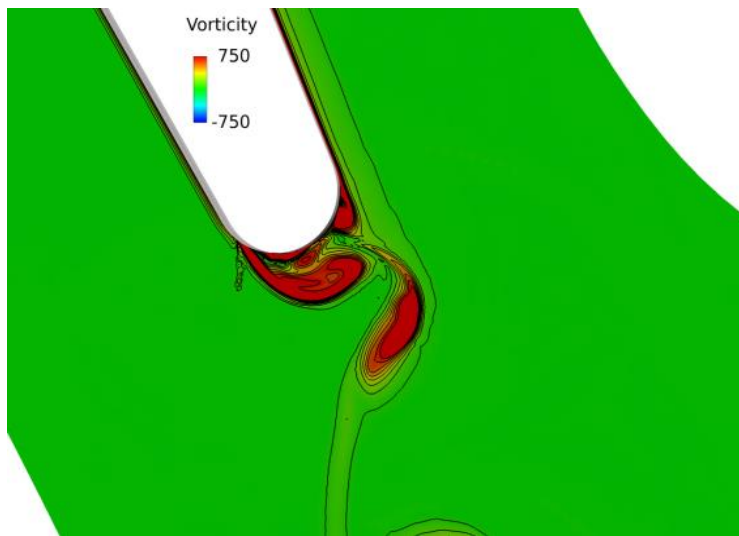


Figure 3.7: Instantaneous vorticity contour in the wake of the blade

Besides observation on the flow field near trailing edge, the frequency comparison at several locations around the trailing edge has been plotted. FFT also shows that the predominant frequency occurred at $S/D = -0.62$, as shown in Fig. 3.8.

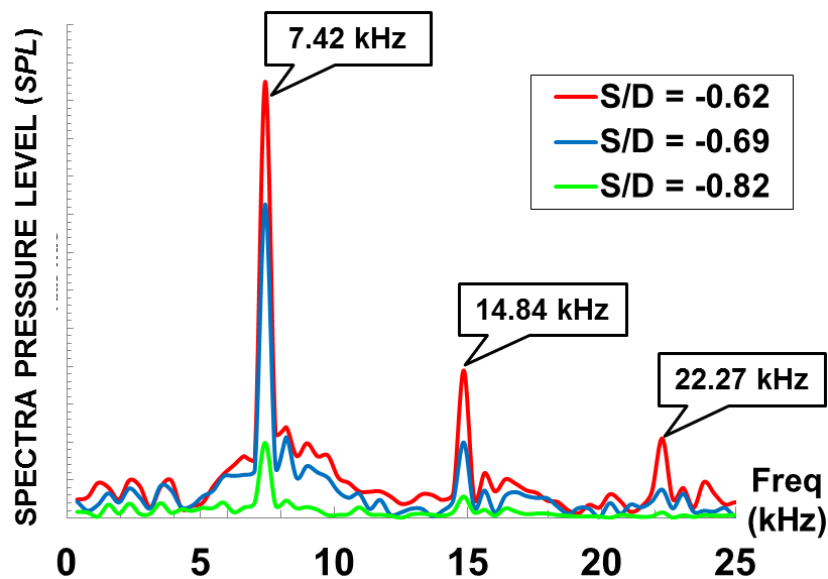


Figure 3.8: Pressure spectra comparison at $S/D = -0.62, -0.69, -0.82$

Spectral Pressure Level (SPL) of the graph shows a peak at 7.42kHz, which is consistent with the reference [71][72]. According to Fig. 3.8, all respective locations have the same frequency peak values. S/D = -0.62 shows a higher peak as compared to other locations. This is one of the reasons why a series of micro-holes has been applied at this location. The comparison between computational and experimental data at the initial three frequency peaks also shows that they agree well with each other, as presented in Table 3.1.

Table 3.1 Comparison frequency (kHz) between numerical and experimental

Peak	Frequency (kHz)		$\Delta\%$
	CFD	Experiment	
1 st	7.42	7.37	0.67
2 nd	14.84	14.71	0.09
3 rd	22.27	22.14	0.59

Boundary layer characteristics have also been validated. Boundary layer profiles were measured at a distance equal to one trailing edge diameter for both the suction side and the pressure side. Fig. 3.9 shows the result of this comparison: a good agreement has been achieved between experimental and computational results.

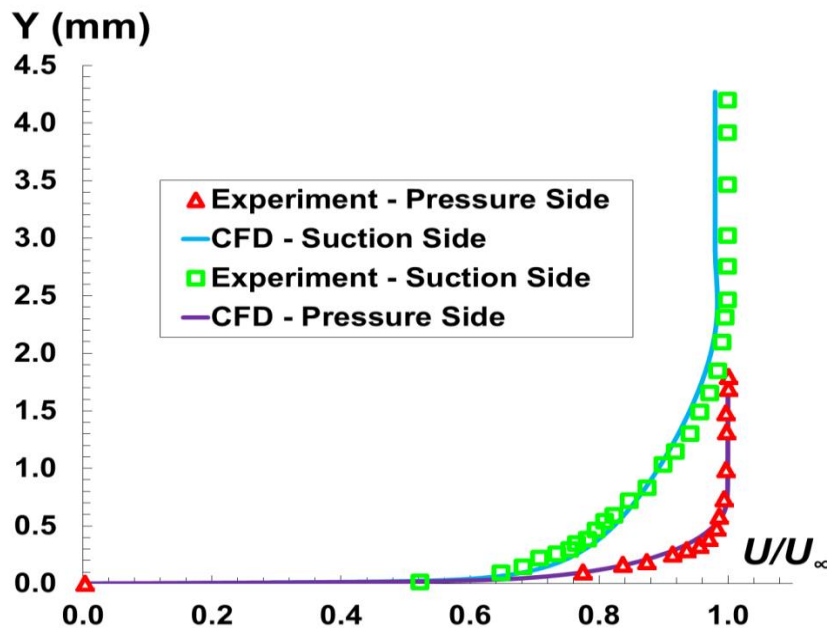


Figure 3.9: Boundary layer profile at trailing edge

3.3.2 VELOCITY PROFILE THICKNESS

Table 3.2 summarizes the three sizes of hole used for investigation at constant $S/D = \pm 0.62$. The “base” represents the basic blade without any hole. ΔL is length of the hole and D_h is diameter of the hole. The velocity profile is plotted on Fig. 3.10. Unity velocity is defined as the point where the profile velocity (u/u_{\max}) remains unchanged with a further increase in Y/D . The profile thickness is measured according to the distance between the point where the velocity becomes unity and the point of maximum velocity (for both suction and pressure sides) as shown in Fig. 4.9. The velocity profile thickness is less in all cases with holes than in the base case. The results are summarized in Table 3.3.

Table 3.2 Hole Diameters at constant $S/D = \pm 0.62$

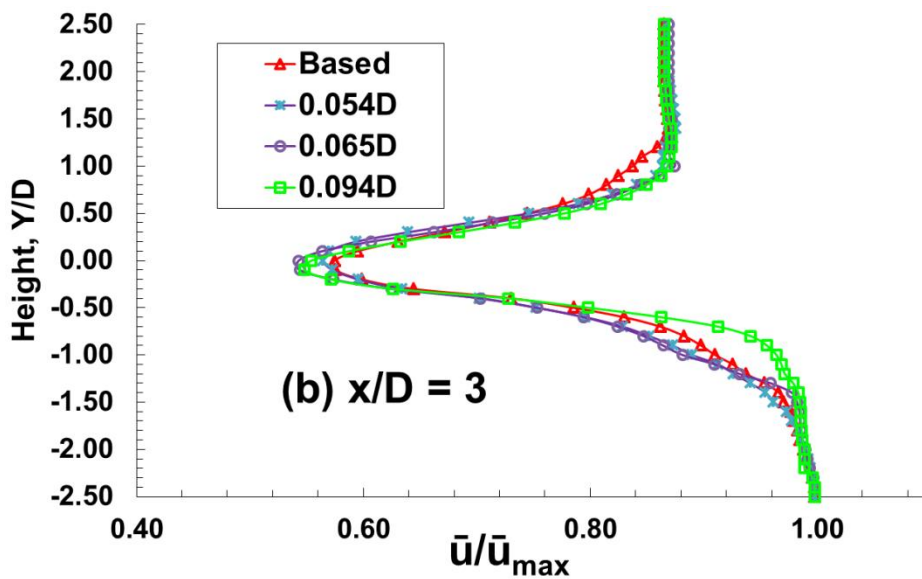
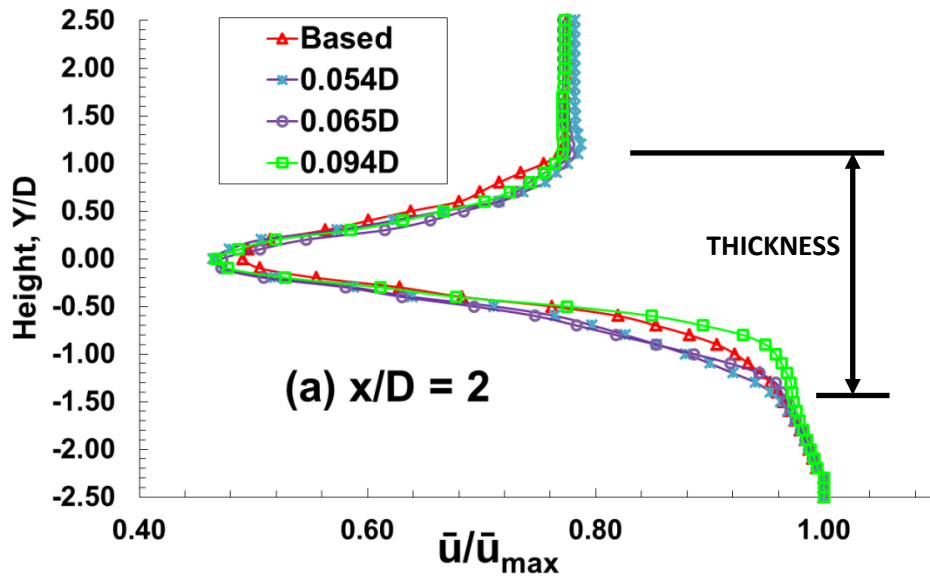
D_h/D	$\Delta L/D_h$
Base	-
0.054	18.12
0.065	15.23
0.094	10.32

Table 3.3 compares the thickness of the velocity profile in each case. The base cascade (no hole) shows growth in the profile thickness downstream from $x/D = 2$ to $x/D = 4$. This wake growth is due to turbulence mixing. When the hole is added at $S/D = \pm 0.62$ on the blade, the velocity profile thickness reduces markedly. For the smallest D_h ($0.054D$), the profile thickness reduces by 14%.

Table 3.3 Velocity Profile Thickness for Different Hole Diameters at (a), (b) and (c)

D_h/D	(a) $x/D = 2$	(b) $x/D = 3$	(c) $x/D = 4$
Base	3.60	3.76	3.92
0.054	3.60	3.50	3.10
0.065	3.60	3.30	2.90
0.094	3.30	3.20	2.50

As D_h increases from $0.054D$ to $0.065D$, the profile thickness further decreases by nearly 20%. For $D_h = 0.094D$, the profile thickness further decreases by 24%. According to Eq. 3.1, an increase in D_h may lead to an increase in U . As U increases, the mixing and momentum increase [80]. The increase in momentum affects the overall velocity. This explains why $D_h = 0.094D$ gives the smallest thickness of the velocity profile. This result is supported by previous result [81]. The average velocity in the wake region is higher in the hole cases, which demonstrates good flow control.



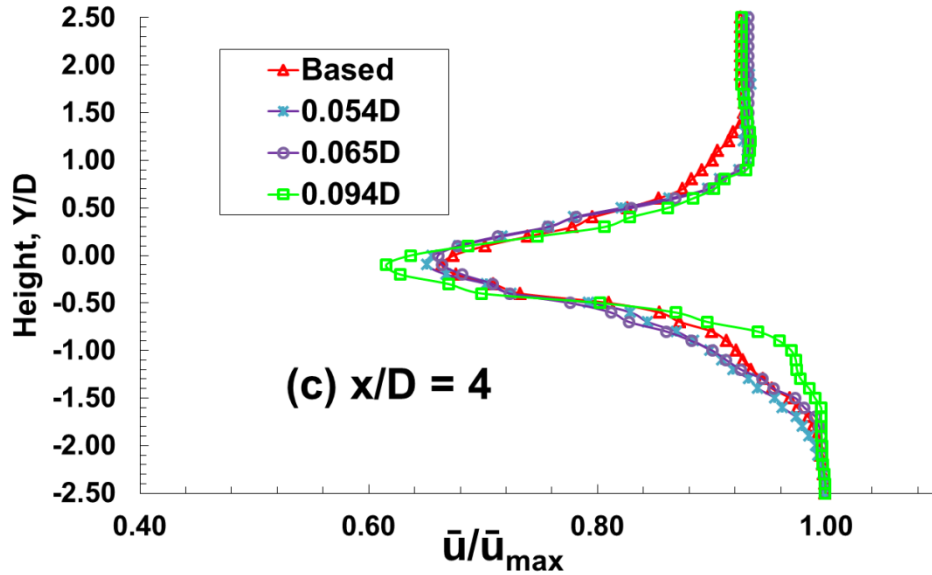


Figure 3.10: Velocity profile at the blade wake for different hole diameters at (a), (b) and (c)

Furthermore, creating the hole has little effect on the velocity component U at the center of the wake region ($-0.4 < Y/D < +0.4$). At this area, the velocity is smaller mainly due to the boundary layer growth. Further downstream, the velocity is increasing due to the mixing and eventually become same with maximum velocity (as observed from $X/D = 2, 3$ and 4). This finding is in line with the previous result [82].

3.3.3 TOTAL PRESSURE

Fig. 3.11 shows the time-averaged total pressure contour in the wake for different values of D_h . As we have seen, the pressure drop is reduced and the vortex is suppressed by adding the hole. Initially, the pressure drop for the base case has dominance in the center region of the wake ($-1 < y/D < +1$), until $x/D = 10$ as shown in Fig. 3.11(a). For $D_h = 0.054D$, the pressure drop is minimized to $x/D = 8$, approximately. As D_h increases from $0.054D$ to $0.065D$, the pressure drop in the wake decreases as the length of x/D decreases - Fig. 3.11(c). For $D_h = 0.094D$, this pressure drop further reduces.

The pressure relaxation is achieved more rapidly for a larger D_h . This can be explained as follows. In this study, the hole is represented in terms of dimensionless velocity (Eq. 3.1). A change in D_h affects U and pressure, as confirmed by previous results [61]. The hole changes the flow stream, resulting in propagation of the local vortex and a decrease in pressure drop in the wake. This is why the total pressure drop at $D_h = 0.094D$ is suppressed at a shortened x/D . Further downstream in the wake (from $x/D = 0$ to $x/D = 10$), the interaction between flows from the suction and pressure sides continues, reducing the pressure drop. Fig. 3.12 shows the distribution of the trailing edge pressure at different values of D_h . An increment in pressure will reduce the wake loss and enhance overall performance [40][41][83]. Trailing edge pressure increases in all cases with holes in the blade, which is confirmed by previous results [70].

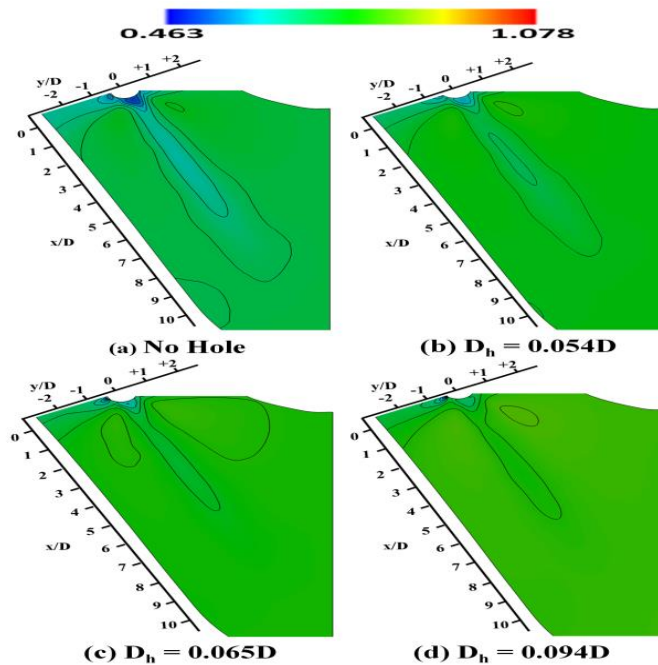


Figure 3.11: Time-averaged total pressure contour at the blade wake for different hole diameters

The trends for $D_h = 0.054D$ and $D_h = 0.065D$ are similar. For $D_h = 0.094D$, the pressure is a maximum of 14% greater than that in the base case. As explained earlier, U increases as D_h increases. Because the pressure in this study is slightly higher than ambient pressure, the changes in cross flow velocity are related to the mean free path.

The mean free path is the average distance of motion of a moving particle and is related to the diameter of the molecule, relative velocity, and pressure.

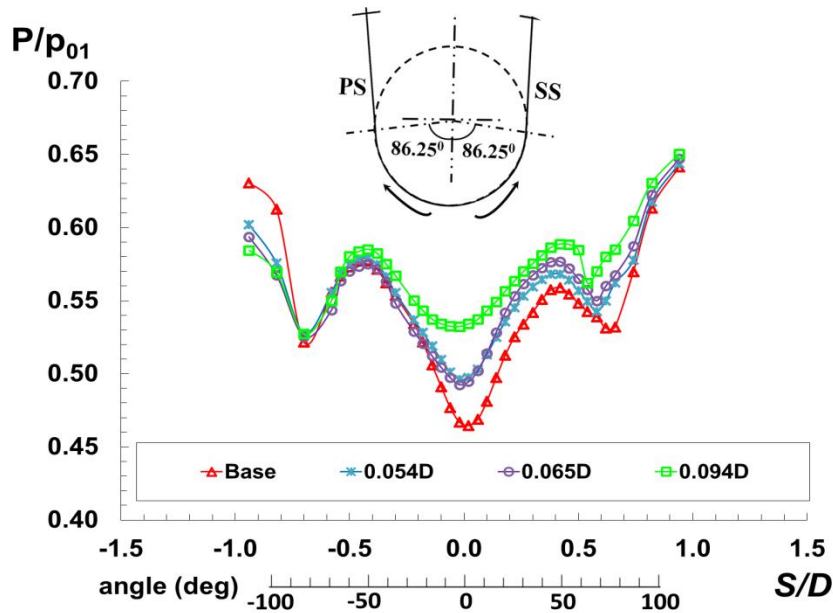


Figure 3.12: Distribution of trailing edge pressure along the trailing edge

As the hole is connected between the pressure side and suction side, the fluid velocity has moved through the hole. This velocity increases at the lower velocity region, which becomes a jet / blowing phenomena. The jet mixes with the flow stream and accelerates the flow, as explained in sub-chapter 3.3.2. This will cause an increase in the boundary layer thickness on the area immediately after the hole area, and will decrease the surface velocity on this area. As this surface velocity is reduced, the surface pressure increases, as explained in the Bernoulli equation and several other studies [133,134], where the pressure coefficient decreases on the suction side when the jet has been applied. As for the pressure side, the velocity flows through the hole, as with the suction phenomenon. This causes the velocity to drop at the area immediately after the hole, for similar reasons as for the suction side.

As the hole diameter increases, more space is available for the flow to go through the hole. As a result, this may increase the velocity and increase the boundary

layer thickness, which is the reason why a larger D_h results in higher pressure. Connecting the pressure and suction sides of the blade, shifts the pressure from the high-pressure region to the low-pressure region. As a result, the pressure increases in the low-pressure region, which offsets the shear layer in this area. This weakens the vortex on the blade surface and reduces the pressure drop in the wake. An increase in pressure distribution indicates the increase of the ratio between jet pressure and cross-flow pressure. A higher jet to cross-flow pressure ratio increases the mixing efficiency [132], eventually suppressing the downstream vortex.

3.3.4 WAKE LOSS

Wake loss, ξ is defined as

$$\xi = \frac{P_{01} - P_{02}}{P_{01} - P_{s,01}} \quad (3.2)$$

where P_S is the static pressure. All pressure values are time averaged.

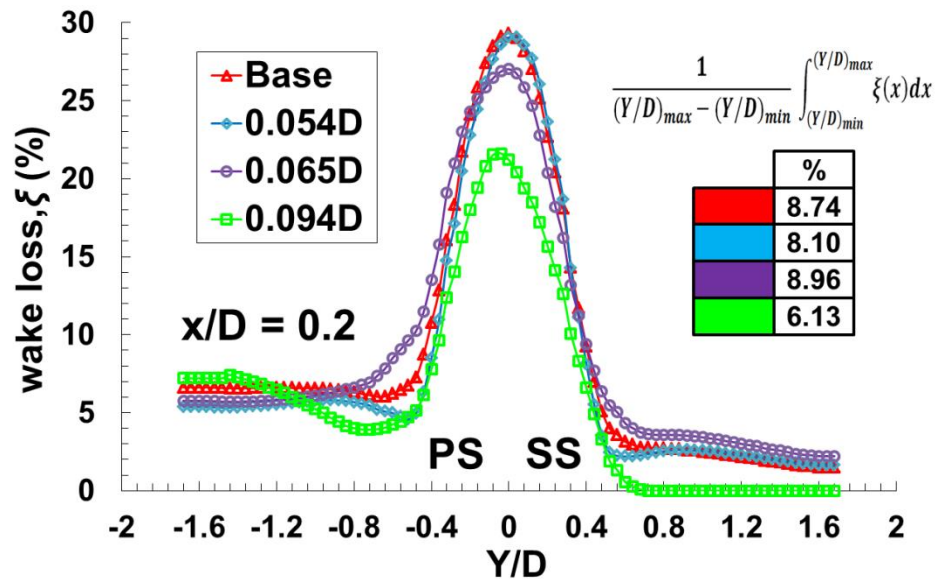


Figure 3.13: Wake loss coefficients at $x/D = 0.2$

Fig. 3.13 shows the wake loss coefficients for different values of D_h . By plotting wake loss, the reduction of the pressure loss can be viewed. Overall, it is clear that ξ is lower in the case of a hole than for the base blade. All graphs have a peak at $Y/D = 0$. The case of $D_h = 0.054D$ has a trend similar to that of the base case. An increase in D_h from $0.054D$ to $0.065D$ decreases ξ by approximately 2% at the center of the wake region. At the same time, ξ increases in the $Y/D > 0.4$ region and $-0.8 < y/D < -0.4$ region. The reduction of ξ is greater when $D_h = 0.094D$. In the center region of the wake ($-1 < Y/D < 1$), wake loss is minimized by a maximum of 10% relative to the base case. The reduction of ξ is related to the increase in pressure produced at the exit of the blade, which was explained previously. As we integrate each curve in respect of the minimum and maximum Y/D value, it is obvious that $D_h = 0.094D$ gives the lowest percentage of ξ .

The increase in pressure at the downstream region of the wake is related to the explanation in previous sub-section 3.3.3, in which the pressure drop at the hole surface is reduced. The surface pressure is thus higher for a blade with a hole than for the blade with no hole. In contrast, there is a small increase in ξ at $Y/D < -1.2$ for $D_h = 0.094D$. This increase is related to the shifted shear boundary layer in a low-pressure region on the surface, and may result in a pressure drop in the field far from the blade's wall and not fully suppressed at a short distance of x/D . As mentioned before, the vortex of a blade with a hole is suppressed more rapidly than the base blade. Fig. 3.14 shows ξ at $x/D = 1.5$. The lowest ξ is observed for $D_h = 0.094D$, which suggests that there is high pressure in this plane ($x/D = 1.5$).

All cases of a blade with a hole have low ξ at a short x/D distance, indicating that a hole directly affects the total pressure produced in the wake. It can be said that D_h affects the trailing edge pressure and wake loss. $D_h = 0.094D$ was chosen for the optimum value for further investigation. While maintaining $D_h = 0.094D$, the location of the hole is changed and the effect of ξ is investigated. Table 3.4 summarizes the variation of S/D at constant D_h . The relationship between the hole location and ξ is presented in Fig. 3.15 and Fig. 3.16. For $S/D = \pm 0.73$, ξ is similar to that in the base case (in the center region of the wake).

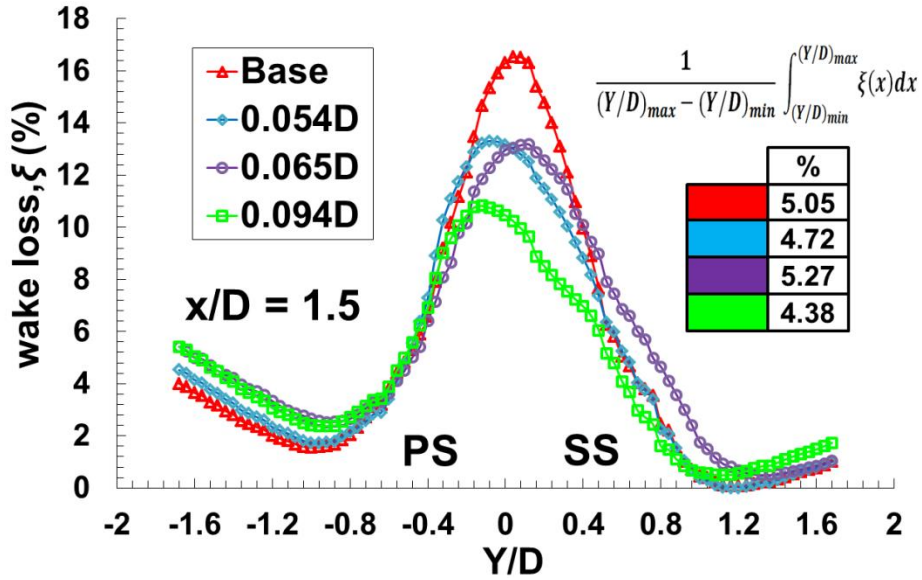


Figure 3.14: Wake loss coefficients at $x/D = 1.5$

This can be explained by the fact that there is no initial vortex formation at this location ($S/D = \pm 0.73$). Creating a hole at this location may have a small effect on the closed flow stream (near the blade surface) and pressure drop. As the hole location shifts to $S/D = \pm 0.58$, ξ decreases. At $S/D = \pm 0.58$, the trend of ξ is similar to that for $S/D = \pm 0.62$. This is because there is an initial vortex in this area, and the addition of the hole thus delays the vortex formation and reduces ξ .

Table 3.4 Variation of S/D at a constant Hole Diameter ($D_h = 0.094D$)

S/D	L/D_h
Base	-
± 0.58	9.69
± 0.62	10.32
± 0.73	11.02

A maximum of 2.61% of reduction in ξ has been achieved in this calculation (average). There are discrepancies in the $Y/D < 0$ region between each case. This is because the hole is added near the initial vortex. The effect of the pressure increment on the low-pressure side thus moves the boundary layer nearer the blade surface, pushes the nearest vortex to downstream, and reduces the pressure in this area. The

hole also delays the vortex formations, thus weakening the vortices, which is confirmed by the visualization in Fig 3.17. This results in the ideal pressure becoming dominant, thus reducing the pressure loss through the hole and reducing the pressure drop in the wake.

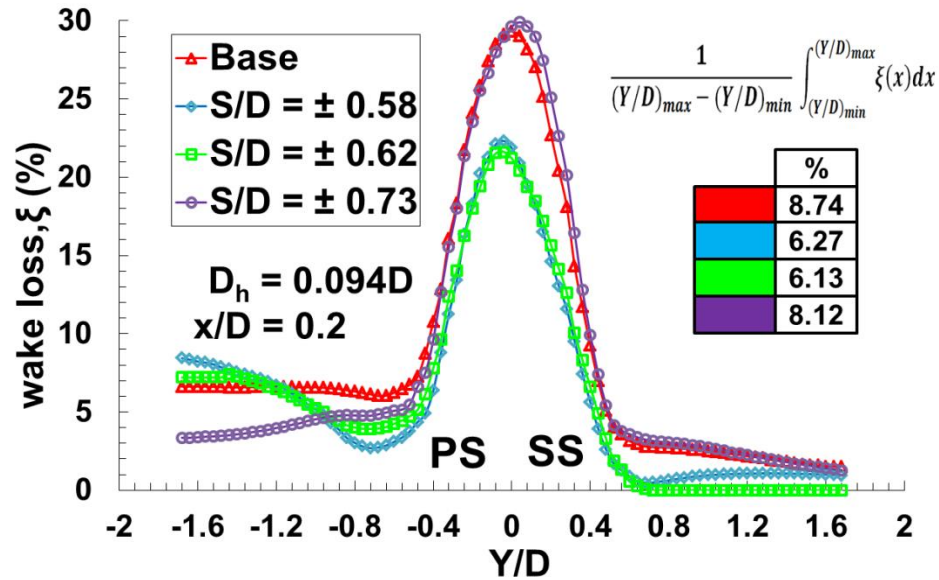


Figure 3.15: Wake loss coefficients at $x/D = 0.2$ ($D_h = 0.094D$)

The vortex cannot be suppressed at a short distance x/D . An observation further downstream is thus needed. Fig. 3.16 presents ξ for different locations at $x/D = 1.5$. Further downstream, the discrepancies of ξ in the $Y/D < 0$ region are eliminated. The base case still produces the highest ξ . On this plane, the difference between $S/D = \pm 0.73$ and the base case is appreciable, in contrast with previous observations at $x/D = 0.2$.

The case of $S/D = \pm 0.62$ continues to produce the lowest ξ . At $S/D = \pm 0.62$, the vortex formation is delayed, which affects vortex formation downstream of the cascade. This shows that a series of micro-holes at the location of vortex formation not only increases the trailing edge pressure distribution but also reduces ξ . This effect may also be due to the lower $\Delta L/D_h$, as reviewed by Bunker [84], who stated that lower $\Delta L/D$ may improve the pressure distribution and reduce the overall energy loss. Modification at the location of the dominant vortex affects the pressure and reduces the energy loss. It can be said that ξ is affected not only by the hole diameter but also by the hole location.

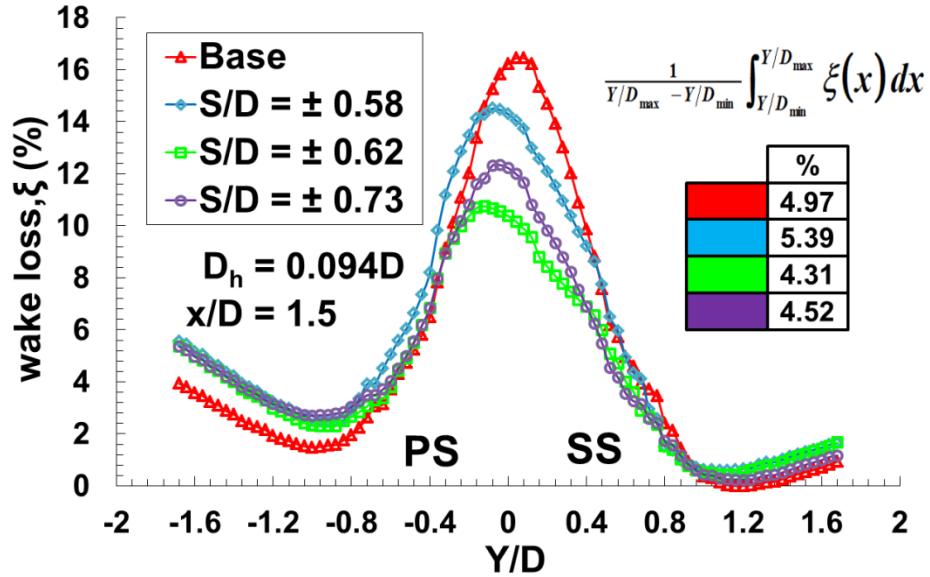


Figure 3.16: Wake loss coefficients at $x/D = 1.5$ ($D_h = 0.094D$)

3.3.5 INSTANTANEOUS FLOW FIELD

The instantaneous iso-surface of the study case has been plotted in order to show better comparison (in terms of flow field) between the base case and the hole case. Fig. 3.17 shows iso-surfaces of vorticity magnitude colored with stream wise velocity. The isometric view has been oriented, which permits the observation of wake vorticity and shear layer, as well as the effect of the hole mechanisms. The figure also illustrates the gradual shedding of the vortex. The comparison has been made at approximately the same time phase. The case, $D_h = 0.094D$ at $S/D = \pm 0.62$, has been chosen for this configuration.

Fig. 3.17(i) corresponds to the initial condition of wake vortex formation for base and hole case. The difference between both cases is readily apparent even at an early stage. There are concentrations of vortices at the trailing edge surface area of the base case, which are not significantly apparent at the span-wise hole oriented case. At this stage, in both cases, enrollment of vortex shedding from the pressure side of the blade has not yet begun.

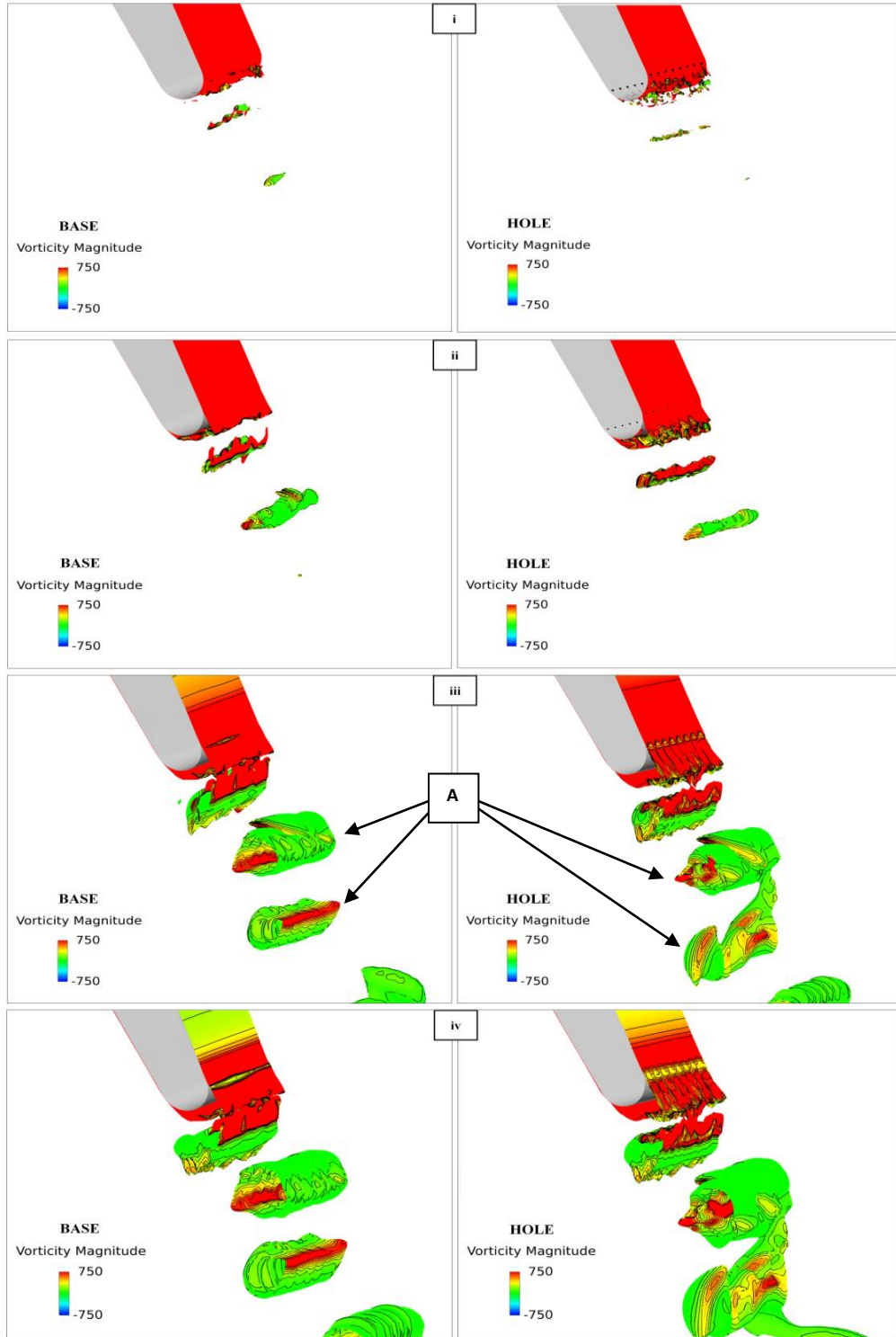


Figure 3.17: Iso-surface instantaneous vorticity magnitude for base and hole case. Hole case condition ($D_h = 0.094D$, $S/D = \pm 0.62$)

As holes were added to the surface of the blade, the vortex suppressed around trailing edge (at the region downstream of the hole area) and reduced the vortex concentration (at the hole area). In short, the addition of micro-holes has successfully suppressed the strong vortex at the surface of the trailing edge. With reference to Fig. 3.17(ii), attention should be focused at the trailing edge area (surface) of the blade. For the hole case, at the region between the hole downstream area ($-0.62 < S/D < +0.62$), a less strong vortex has been developed, which did not appear in the base case. This is believed to be due to the vortex, where the pressure side started to enroll and mix with the suction side vortex. At the same time, the vortex started to grow and moved away from the trailing edge.

In both cases (base and hole), when a downstream vortex initially developed, approximately the same sized vortex was produced. However, a significant difference is apparent in Fig. 3.17(iii). While the micro-hole series continue to induce a strong vortex, the “second vortices” downstream of the wake become separated from the initial vortex formation. While for the base case, “second vortices” are not fully separated from the initial vortex. Further downstream of the wake, we can observe the development of vortex shedding for both cases. For the hole case, this growth, which has been labeled as “A” in Fig. 3.17(iii), is significantly reduced. From the appearance of the contours and also the physical structure of the vortex, we can say that at “A”, vortex strength has been reduced, and the structured vortex which appeared in the base case, is physically changed in hole cases.

For Fig. 3.17(iv) shows that as the interaction between the vortices continues, the strong vortex concentration observed in the base case gradually becomes less evident in the hole case (at trailing edge surface). A significant difference is observed at the surface area, where the holes have been added. Even in the base case, there are vortices with relatively low strength on the suction side and when a series of micro-holes are added to this area, the vortex seems to be well distributed span wise along the blade. As a result, this reduces the vortex strength in the wake and causes the vortex to separate from the initial vortex. Further downstream, the same effect as in the previous figure becomes more obvious. A strong contour vortex appears in the base case, but is suppressed in the hole case. No concentrated and “structured” vortices can be seen

downstream of the hole case, and a delayed vortex formation in the downstream area has been achieved.

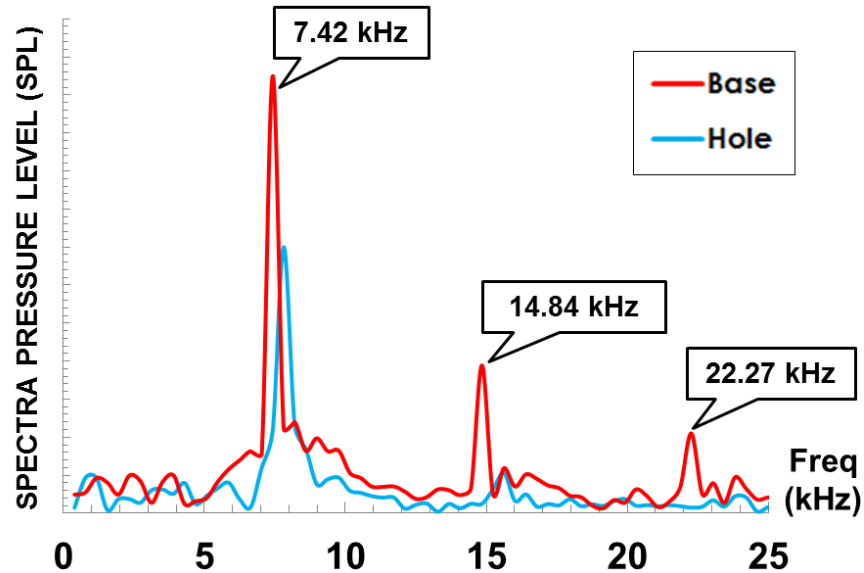


Figure 3.18: Frequency comparison between base case and hole case. Hole case condition ($D_h = 0.094D$, $S/D = \pm 0.62$)

Fig. 3.18 shows the comparison of frequency between the base case and the hole case. It can be seen that the frequency power is reduced significantly (for the hole case), especially for the 2nd and 3rd peaks. In summary, the addition of a series of micro-hole reduces vortex formation at the trailing edge surface initially, which leads to a reduction in the strength of the vortex at the blade wake. Further downstream, the delay in vortex formation is also observed.

Another parameter that is associated with blade loss is entropy increase [3]. The main source of entropy is the viscous effect of boundary layers and the mixing process, shock wave and heat transfer [3]. Fig. 3.19 shows a comparison of entropy generation in the base case and in the hole case ($D_h = 0.094D$, $S/D = \pm 0.62$). The decrease of entropy generation means a reduction in loss. As seen in this figure, the entropy produced from the blade in the hole case is lower than in the case of the no hole blade. In the downstream area of the wake, flow mixing continues, initially very rapidly, up to one chord of the blade [85]. Physically, a shear layer depends on the stream wise

pressure gradient and transverse velocity gradient, dV/dy [4]. Making holes at the trailing edge allows the flow to be mixed between the suction side and pressure side, while jet mixing at the surface reduces the shear layer at the hole area [86]. This is due to the fact that the jet has reduced the friction on the surface and reduced maximum velocity. As this shear layer decreases, the rate of entropy generation is also reduced, which is proportional to $\mu_{\text{eff}} (dV/dy)^2$ [3]. This explains why entropy generation in the hole case is lower than in the no hole case.

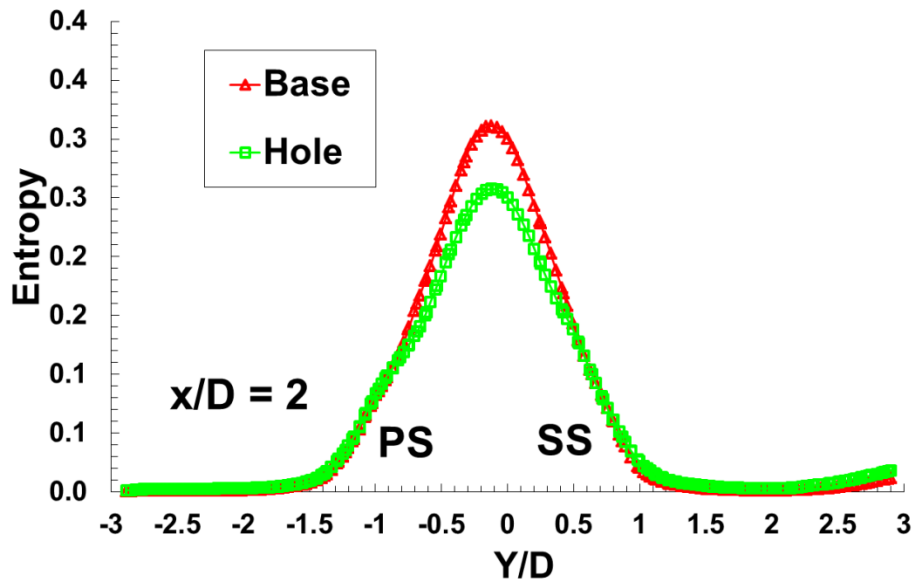


Figure 3.19: Entropy generation comparison between base case and hole case. Hole case condition ($D_h = 0.094D$, $S/D = \pm 0.62$)

3.4 CONCLUSIONS

The application of a series of micro-holes on a turbine blade was numerically investigated. The turbulence model selection was a vital step in order to obtain an accurate result; finally, the *SA-DDES* turbulence model was chosen in this calculation. First, the effect of the hole size was investigated. The larger hole diameter of $0.094D$ was the most effective among three diameters tested. $D_h = 0.094D$ reduced the wake loss by a maximum of 10%, increased the trailing edge pressure distribution by 14% and reduced wake velocity profile thickness by a maximum of 24%, as compared to the

base (no hole) case. In addition, it was found that a series of micro-holes suppresses the vortex and reduces the pressure drop in the wake at lower distances of x/D .

Next, the effect of the location of a series of fixed diameter holes of $0.094D$ was studied. The optimal location was obtained at $S/D = \pm 0.62$, where approximately 2.6% maximum reduction in average wake loss was achieved, compared to the base case. The location of the holes is also significant; at the upstream location ($S/D = \pm 0.73$) is weakly affected by pressure distribution and wake loss, which is similar to the base case. In contrast, at the downstream location ($S/D = \pm 0.58$), the wake loss was reduced by 2.4%, compared to the base case, which was similar to the result at $S/D = \pm 0.62$. It can be concluded that placing a series of micro holes downstream of $S/D = \pm 0.62$ is effective for vortex suppression.

In conclusion, a micro-hole series of $D_h = 0.094D$ at $S/D = \pm 0.62$ is shown to produce the most effective results, compared to other configurations, and the ensuing flow field also shows suppression of the vortex downstream of the blade wake.

CHAPTER 4

DIFFERENT STEADY SYNTHETIC JET HOLE ARRANGEMENTS ON A HIGH SUBSONIC TURBINE BLADE

4.1 INTRODUCTION

Turbine blade wakes normally exhibit an unsteady character in the form of vortex shedding (von Karman vortex streets) [2]. The total loss associated with vortex shedding is generally significant at conditions of high-speed [3]. However,

These losses can be reduced through optimization of the blade geometry (shape), proper flow control, and boundary layer control. A synthetic jet is an option for flow control, and is widely being used in incompressible laminar flow. To date, there are few studies of the effect of synthetic jets at high subsonic flow, since no flow separation has occurred under high Reynolds number operating conditions; i.e. with a spark-synthetic jet actuator [87]. A synthetic jet has the advantage of zero mass input and non-zero input of momentum without any extra air-supply device [88]. The jet can be either a steady/continuous jet or a blowing and suction jet. The impact of synthetic jets on the performance of the turbine blade aerodynamics is still being studied [88]. Different locations, directions and arrangements of synthetic jets have different effects [89].

Nominal direction of a synthetic jet may generate vortex pairs induced by span wise instability, transition to turbulence, and become indistinguishable from the mean jet flow [90]. The effect of the number of holes in the steady synthetic jet and its arrangement are new elements of investigation in high subsonic flow synthetic jet

studies. This study is motivated by several findings from previous research. Aram et al. [91] has claimed that strong counter-rotating vortices can be observed only on the stream-wise oriented synthetic jet, and cannot be observed on a span-wise oriented configuration. A span-wise distribution of synthetic jet is beneficial in delaying trailing edge separation [87]. Thus, span-wise and stream-wise configurations each has its own benefit. In this study, both effects have been combined. Applying a synthetic jet can also reduce vortex shedding at the blade wake. Rizzetta et. al. [92] investigated the near wake regions of the aft-blade and found that active synthetic jet control is able to reduce the wake loss coefficient by about 53% ~ 56%. This effect was also confirmed by Kurmanov et al. [69]. Thus, the present study focuses on the effect of single, double and triple rows of steady synthetic jets on wake vortex shedding and on the pressure around the blade and at the wake.

4.2 NUMERICAL METHOD

The three-dimensional, Reynolds-averaged, unsteady Navier–Stokes equation for compressible flow is solved. For this calculation, standard central difference is used for discretizing the viscous flux, and total variation diminishing scheme is used for discretizing the inviscid fluxes. The procedure is second-order accurate in time, and the calculations are carried out using a structured in-house and single-block code method. Roe’s flux-difference splitting scheme is used for a numerical inviscid flux calculation, where second-order accuracy is achieved by employing the MUSCL scheme with the van Albada flux limiter, while the lower upper symmetric Gauss Seidel together with a second-order dual time stepping method is employed to calculate the unsteady flow.

Fig. 4.1 shows a close-up view of the region around the trailing edge. The maximum number of iterations is 2×10^5 , and there are five inner iterations for the implicit scheme (time marching). Dimensionless Δt^* is equal to 105.42×10^{-6} and the physical time step $\Delta t = 3.33 \times 10^{-7}$ s. The numerical method is validated by comparing the numerical results with experimental data obtained by Sieverding et al., [71] for the configuration without a hole. The instantaneous result calculated a Courant–Friedrichs–Lewy number of around 10. The configuration of the cascade is presented in Fig. 4.2,

which is the same as Sieverding et al. The chord, C is 140 mm, axial chord, C_{ax} is 91.84 mm, trailing edge diameter, D is 7.43 mm and pitch, s is 97.44 mm. The span-wise size of the blade is 10% of the blade chord length.

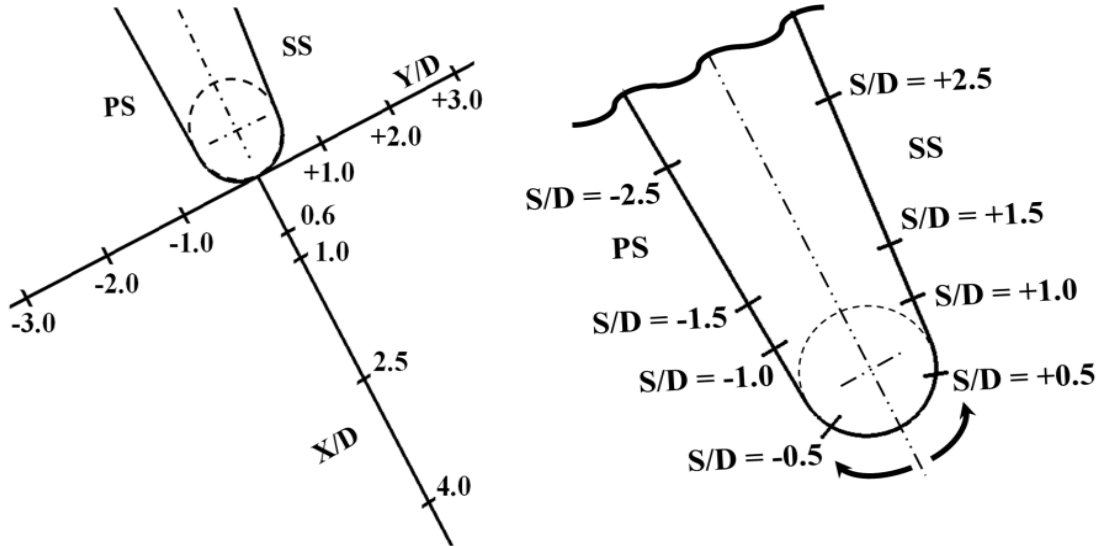


Figure 4.1: Trailing-edge S/D , x/D and Y/D reference system

4.2.1 BOUNDARY CONDITIONS

Fig. 4.2 shows an O-type structured grid that has 4.0×10^6 grid points. In pre-processing, the grid has been developed via Gridgen software and the minimum grid size is 0.002mm ($y^+ \approx 1$). Imposed boundary conditions at the turbine inlet are total pressure, $P_{01} = 140,000$ Pa and total temperature, $T_{01} = 280$ K, respectively. At the outlet, isentropic Mach number, $M_{is,02} = 0.79$ and Reynolds number is 2.8×10^6 . To achieve these conditions, the outlet pressure is specified as $P_{02} = 92,755$ Pa.

At the blade surface, a non-slip adiabatic wall boundary condition is applied. For the inlet boundary condition, subsonic Riemann Invariant condition, R_{01} has been imposed. A translational periodical boundary condition is applied for this calculation, illustrated in Figure 4.2, as in previous studies [60]. The static pressure has been prescribed at the outlet, thus the subsonic outlet boundary condition has been imposed.

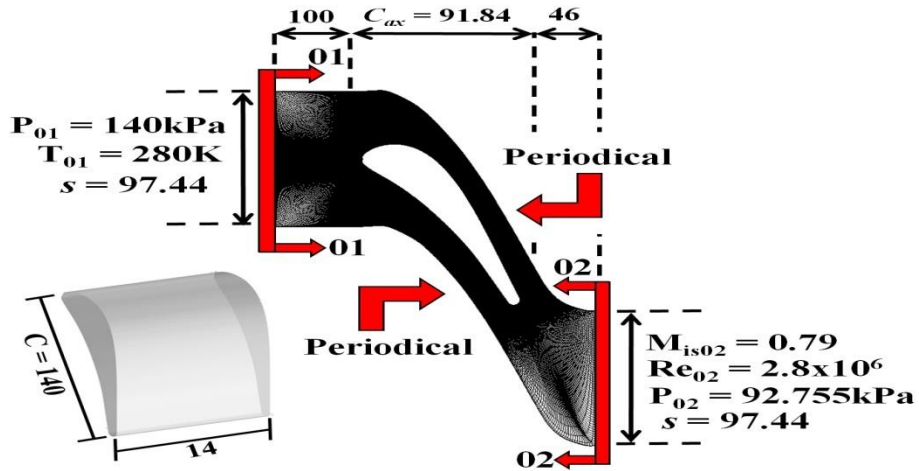


Figure 4.2: Boundary condition, calculation grid, blade configuration and dimensions (in mm)

The synthetic jet is represented in terms of finite jet Mach number, M_{jet} at the surface of the blade, which is defined as [93];

$$M_{jet} = \frac{V_{in,jet}}{V_{stream}} = \frac{\text{Velocity of the jet}}{\text{Velocity of stream}} \quad (4.1)$$

First, the computations are carried out to investigate the effect of a single row of synthetic jet holes at different locations, with constant size and flow rate.

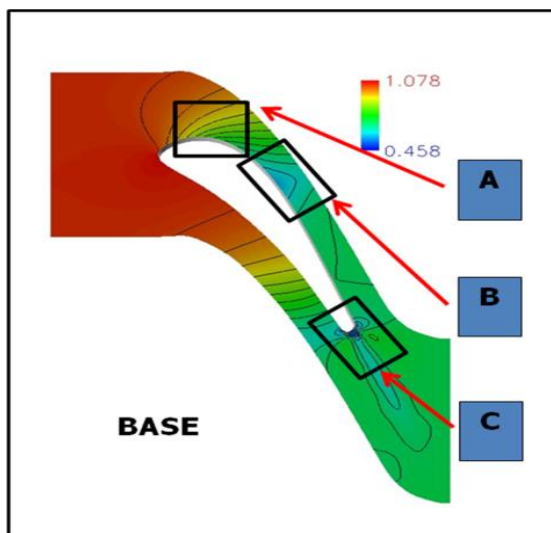


Table 4.1 Location of pressure difference

Label	S/D	Location
A	+19.67	$0.27C_{ax}$
B	+13.67	$0.42C_{ax}$
C	+0.67	$0.97C_{ax}$

Figure 4.3: The location selection for Synthetic jet configurations

This location has been identified based on the area where large differences in total pressure occurred, as shown in Fig. 4.3, and based on the wake loss produced at respective location. This pressure difference from leading edge to trailing edge is mainly due to blade design. The wake loss, ξ can be calculated as in Eq. (3.2). All pressure values are time averaged. Fig. 4.4 shows the wake loss for each location at $x/D = 1.5$.

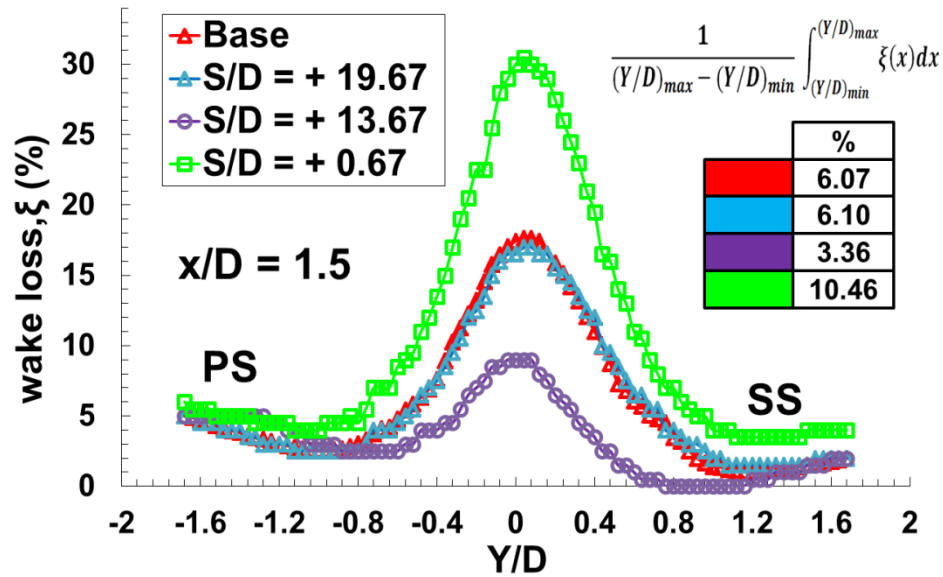


Figure 4.4: Wake Loss for Base, A, B and C

The lowest wake loss was obtained when the synthetic jet is applied at $S/D = +13.67$. As a result, the location of $S/D = +13.67$ was chosen. Next, the number of rows of synthetic jet holes, single, double and triple rows, was further investigated, as illustrated in Fig. 4.5. These three configurations of slot-hole series can give a better description of the stream-wise and - span wise effect of a synthetic jet. Since the focus of this study is to observe the aerodynamic flow field and the blade wake flow, the detail inside the synthetic jet hole is not discussed. All the slot-holes are $0.13D \times 0.13D$ in size and slots are placed equidistantly at $\Delta Z = 1.17\text{mm}$. A synthetic jet angle, α_{syn} of 10 degrees tangential to the flow direction and M_{jet} of 0.7 are constant for all cases. The slot-holes have been applied only on the suction side surface for all cases, as in previous research [94].

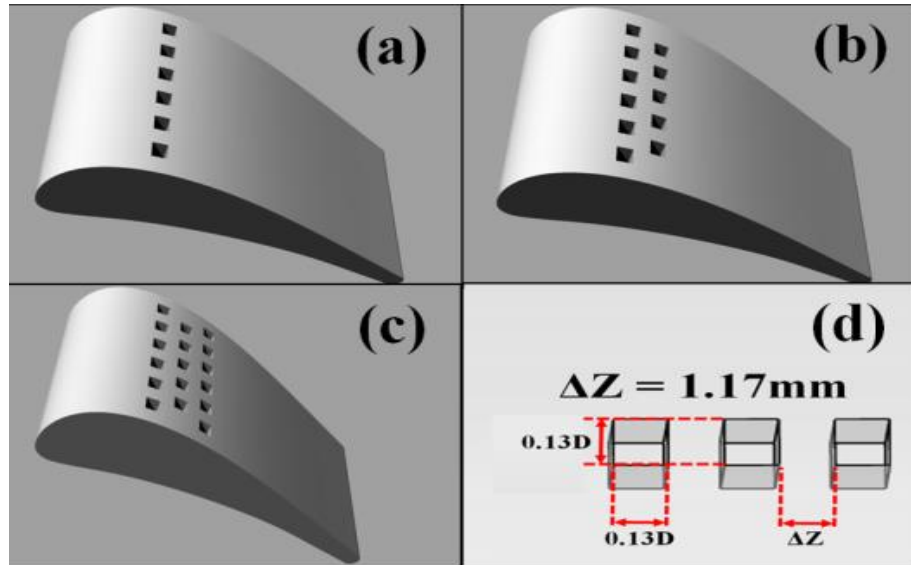


Figure 4.5: Synthetic jet configurations (a) single slot-hole (b) double slot-hole (c) triple slot-hole (d) slot-hole configurations

Four turbulence models have been tested, which are Spalart Allamaras (*SA*), Detached Eddy Simulation (*DES*), Delay Detached Eddy Simulation (*DDES*) and Improved Delay Detached Eddy Simulation (*IDDES*) turbulence models [62][64][65][67][95], as explained in Chapter 2. The comparisons of the turbulence models were explicated in Chapter 3, and the *SA-DDES* turbulence model has been chosen to be used in this study.

4.3 RESULTS AND FINDINGS

4.3.1 SURFACE PRESSURE COEFFICIENT, $C_{P,sur}$ AND LIFT COEFFICIENT, C_L

Each configuration case has been compared with the base case. Since the experimental result of $C_{P,sur}$ is not available in the literature, the $C_{P,sur}$ of the base case relies on the simulation result. Fig. 4.6 shows the result of $C_{P,sur}$ for all cases. For the base case, $C_{P,sur}$ shows a downward trend of pressure at the trailing edge suction side. Adding the synthetic jet changes the pressure coefficient effect on the blade [69]. Adding a single row of synthetic jet caused the pressure spike to plateau at $0.5 < x/C_{ax}$

<0.6. This pressure spike is due to the introduction of the synthetic jet that causes the surface pressure to increase sharply up to 0.70, which is consistent with previous findings [89][96]. The pressure then decreases to a minimum value of -0.6. The sudden pressure drop is due to the development of boundary layer trajectories. Since the velocity ratio (M_{jet}) is quite high (0.7), it is expected that the jet would block the stream flow and boundary layer, causing the cross flow to be diverted over and around the jet flow. This will create a low pressure region downstream near the jet area [131]. The maximum increment of 53% in $C_{P,sur}$ (as compared with the base case) occurred at the trailing edge area ($x/C_{ax} > 0.9$).

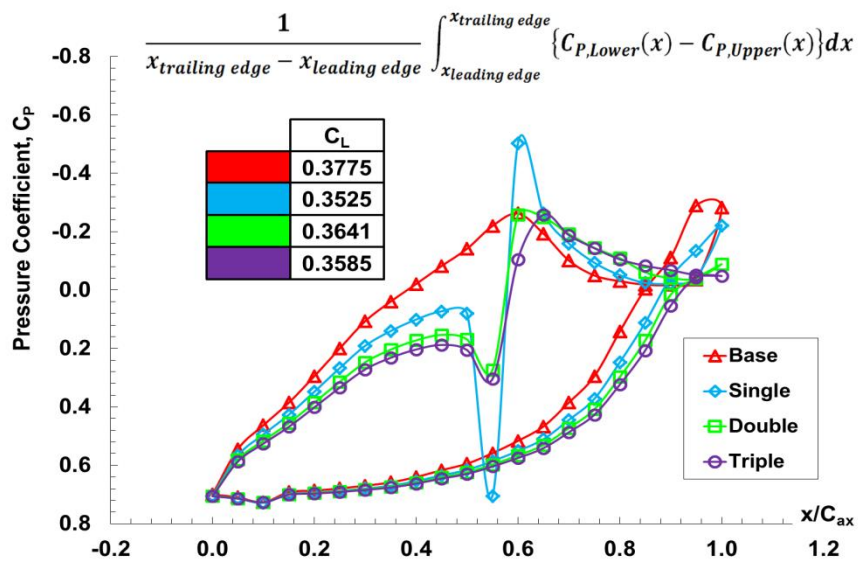


Figure 4.6 Pressure Coefficient (C_P) and Lift Coefficient (C_L) for each case

When another row of slot-holes (double row) is added, the respective $C_{P,sur}$ plateau is reduced. A significant effect is observed at $x/C_{ax} = 0.6$, where the reduction of pressure has improved about 50% compared to the single row application. Improvement has also been achieved at the trailing edge area, where $C_{P,sur}$ has been fully eliminated. As for the pressure side, a small increment of $C_{P,sur}$ has occurred between $0.4 < x/C_{ax} < 0.9$. In the case of the triple row of synthetic jets, the result exhibits a similar trend to that of the double row case. A small increment of $C_{P,sur}$ can be observed at $x/C_{ax} = 0.6$. Between $0.65 < x/C_{ax} < 0.9$, the $C_{P,sur}$ registered a small reduction for all cases where synthetic jets were introduced.

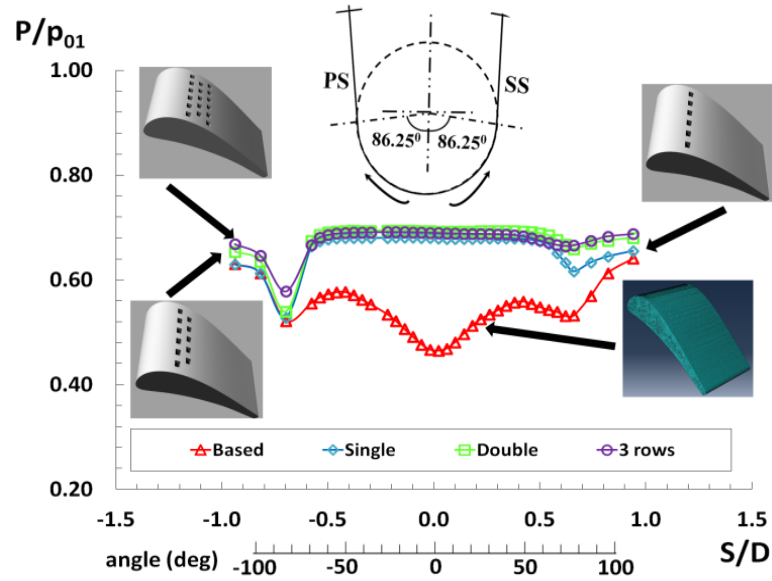


Figure 4.7 Distribution of trailing edge pressure for each case

The increase of $C_{p,sur}$ is related to velocity changes at the location of the synthetic jet. The Bernoulli equation explains that the velocity increase will cause a reduction in pressure, and vice versa. In this calculation, the velocity of the jet is introduced lower than stream velocity, which may cause a reduction in flow velocity, hence increasing the pressure distribution. The lift coefficient can be obtained by;

$$C_L = \frac{1}{X_{TE} - X_{LE}} \int_{X_{LE}}^{X_{TE}} [C_{P,lower}(x) - C_{P,upper}(x)] dx , \quad (4.2)$$

where X_{LE} and X_{TE} denote the $-x$ coordinate of the leading edge and the trailing edge of the blade, while $C_{P,lower}$ is the pressure coefficient on the lower surface and $C_{P,upper}$ is the pressure coefficient on the upper surface. It can be seen that adding synthetic jets has reduced the lift coefficient. Fig. 4.7 shows the distribution of the trailing edge pressure. An increment in pressure reduces the wake loss and enhances the overall performance. It is clear that the synthetic jet increases the trailing edge pressure distribution, which is confirmed by previous results [97]. The trends for all the synthetic

jet applications are similar. Small discrepancies between each synthetic jet configuration have been observed at $S/D > 0.5$ and $S/D < -0.5$.

The steady synthetic jet is applied on the suction side and this jet is mixed with the flow stream, which accelerates the flow, as explained in Chapter 3, sub-section 3.3.2. This causes an increase in boundary layer thickness on the area right after the area where the jet is located, causing the surface velocity on this area to decrease. As surface velocity decreases, surface pressure increases, as explained per the Bernoulli equation and other references [133,134], where the pressure coefficient decreases on the suction side when the jet has been applied. This is why surface pressure distribution increases in configurations with holes. Overall, it can be said that the application of synthetic jets increases the pressure of the trailing edge and decreases the pressure drop at the wake.

4.3.2 FLOW FIELD CONTOURS

Fig. 4.8 shows the time-averaged total pressure contour around the blade. At the wake area, the pressure drop is reduced and the vortex is suppressed. Initially, the pressure drop for the base case is greatest in the central region of the wake from $(-1 < y/D < +1)$, until $x/D = 10$.

Adding a single row of holes, reduces the area of pressure drop (at the location where the synthetic jet is applied), but at the same time, the magnitude of the pressure drop increases, which is consistent with the result of $C_{p,sur}$ in the previous result. In contrast, the pressure at the wake dropped substantially, compared to the base case, where the pressure drop has been eliminated.

In the case of the double row synthetic jet, the high magnitude of pressure drop (at the hole area) is reduced and the wake area remains without any pressure drop. For the triple case, the flow field was almost the same as for the double case. As the jet phenomena are added, the flow around the blade surface is disturbed and “blocked”. This may lead to significant reduction of pressure at the jet area, as seen in Fig. 4.8.

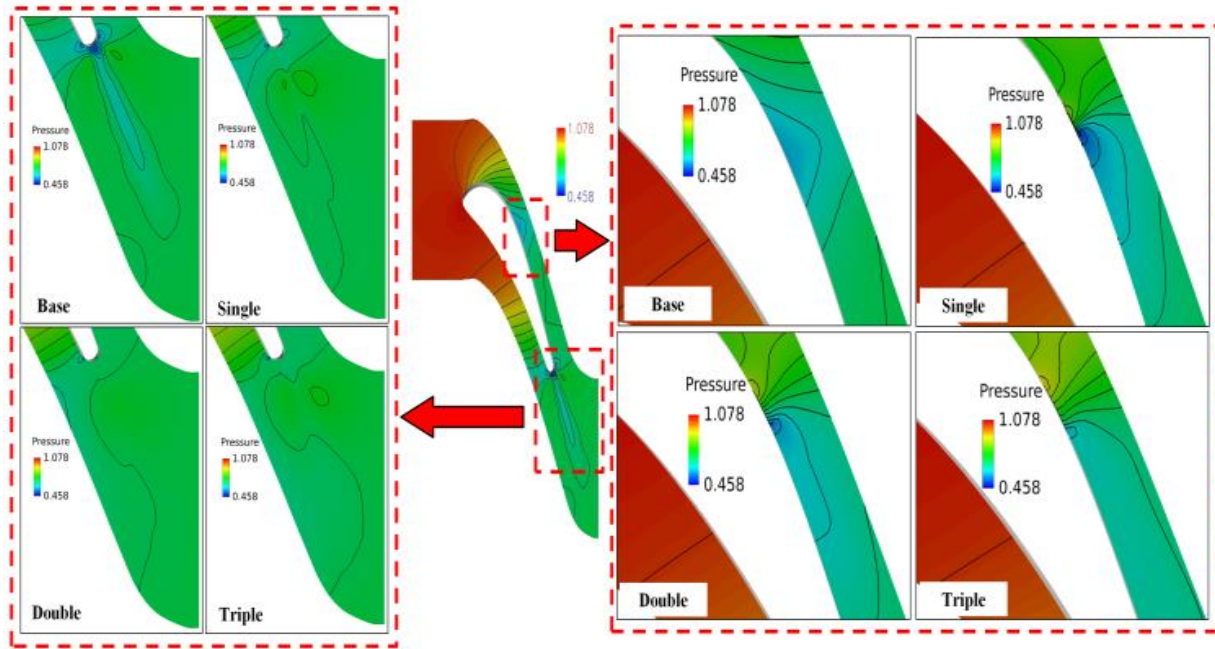


Figure 4.8 Time average total pressure contour (a) Base, (b) Single Row (c) Double Rows and (d) Triple Rows Hole

Fig. 4.9 corresponds to the instantaneous iso-surface vorticity of each case. Before the synthetic jet is applied, strong vortices have developed at the wake of the blade, especially at the suction side of the blade. When the single row of holes of the synthetic jet is applied, this vortex fluctuation and strength are significantly reduced. There is also a significant delay in the reattachment of the boundary layer which develops as a consequence of the synthetic jet, and is believed to be due to compressible effect [87][98]. In the case of a double row of holes, the reattachment area between the vorticity is slightly longer than in the single case, occurring at approximately $x/D \approx 0.8$. Further downstream at the wake, the interaction between the vortex continues at low strength.

The triple row case displays unsteadiness of the vortex at the suction side surface and this affects vortex formation downstream at the wake. In this configuration, the vortex develops different shapes, compared to the other cases.

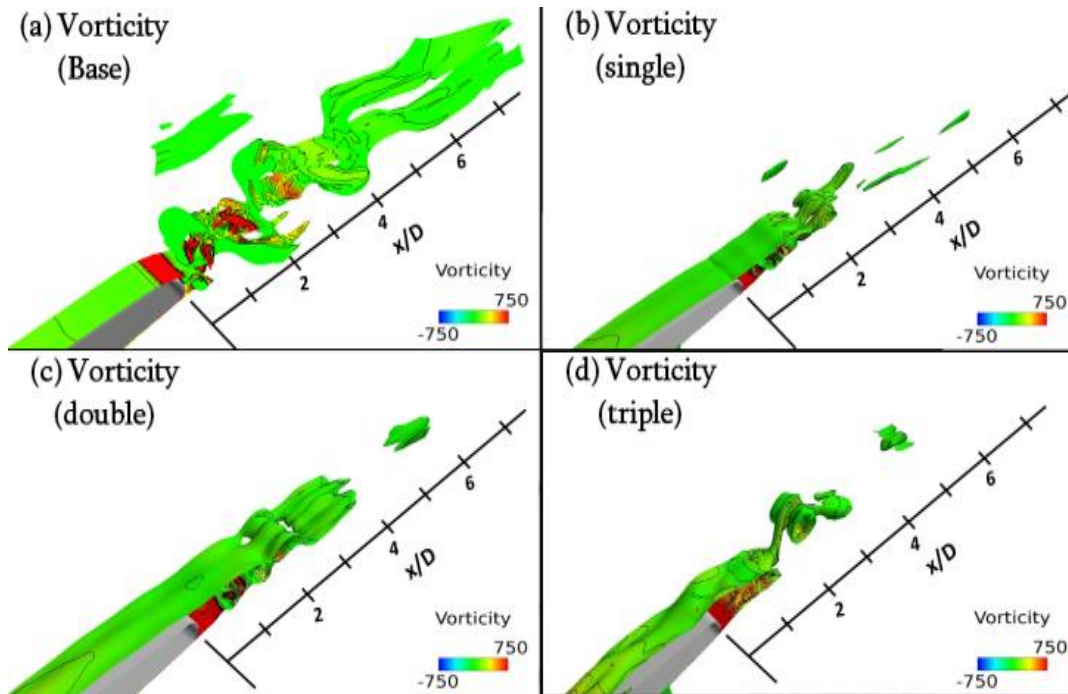


Figure 4.9 Iso-surface instantaneous vorticity for each case

4.3.3 WAKE LOSS

Fig. 4.10 shows the wake loss coefficients for different hole arrangements at $x/D = 1.5$. By plotting the wake loss, the reduction of pressure loss can be viewed. Overall, it is clear that ξ is lower in the case of a synthetic jet than for the base blade. All graphs have a peak at $y/D = 0$. All synthetic jet configurations reduce the wake loss. Reduction in wake loss suggests that the pressure at the wake has increased. A single row case reduces ξ by about 44%, compared to base case. The lowest ξ is achieved by the double row case, in which the maximum reduction of wake loss is approximately 2% lower than for the single case. A triple row of synthetic jet registered an increment in wake loss of about 9.2% compared to double row case, although it was still lower than the base case. Even though the synthetic jet was applied only at the suction side surface, the effect on wake loss can be presented as the overall wake loss reduction [99].

CHAPTER 5

SIMULATION OF COMPRESSIBLE AND MULTI-PHASE FLOW IN PLASMA SPRAY WITH FVM-MPS HYBRID METHOD

5.1 INTRODUCTION

As the previous chapter has confirmed, the application of a series of micro-holes at the trailing edge area has been proven computationally to be effective for downstream vortex suppression. Several techniques for making micro-holes on a turbine blade have been suggested, including laser drilling, electrolyte jet drilling, electrochemical machining, and electrical discharge machining.

5.1.1 Electrical Discharge Machining (EDM)

Electrical Discharge Machining (EDM) is a non-traditional machining process. The basic components in the EDM process consist of a tool electrode, a work piece, and a dielectric and pulse generator. The process is based on removing material from the work piece surface by a series of electrical discharges between the tool and the work piece in the presence of dielectric fluid. By moving the tool electrode towards the work piece, an arc discharge can occur in a narrow gap of several μm to several tens μm between the two electrodes after high voltage is applied. Material is removed by melting and/or evaporating. Generally, EDM can be classified into two main categories: sinking EDM, and wire EDM.

The increase in demand for micro parts and products has forced manufacturers and researchers to explore methods of producing products which are small in size and high in accuracy. When EDM processes are applied to produce a product with holes, cavities or pins smaller than 500 μm , the process is categorized as micro EDM [100][101]. Examples of the application are drilling small and deep holes for turbine components or for fuel injection nozzles [102][103][104]. To realize machining in micro scale, two main requirements should be fulfilled: reduction of unit removal, and improvement of equipment precision [100]. Since there is no direct contact between the electrode and the work piece with EDM, problems related to mechanical stresses, chatter, and vibration during machining can be eliminated. Regardless of hardness, any conductive materials can be machined by EDM. One of the challenges in using EDM as a tool for making micro holes in turbine blades is that EDM can only make contact with conductive surface. Normally, a turbine blade is coated with a non-conductive coating to operate under high temperature systems.

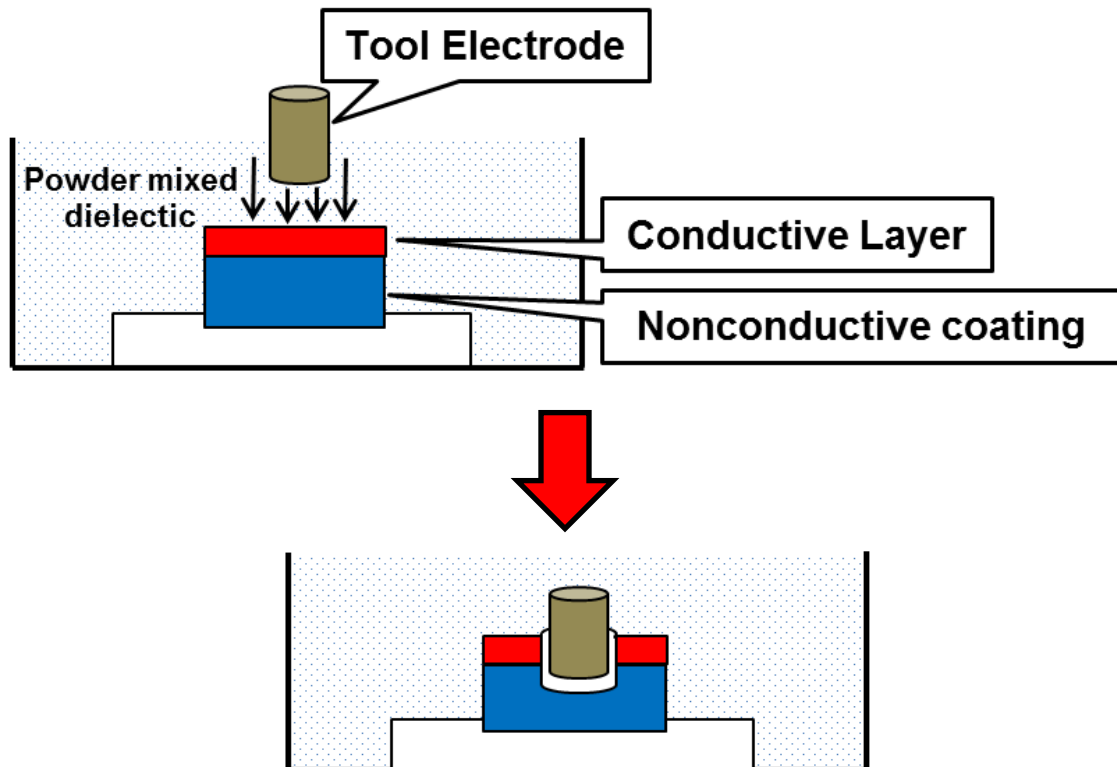


Figure 5.1 Proposed method of conductor coating by [105]

In order to solve this limitation, Gokhan and Cogun [105] have proposed a new method by applying a layer of conductive coating on the surface / area where the EDM is to take place [105]. This conductive layer coating provides electrical conductivity on the surface to be machined. The initial discharge formations occur between the tool electrode and conductive layer. After this conductive layer is completely eroded, conductivity is provided by means of graphite powder added into a dielectric fluid which serves as a bridge between the nonconductive workpiece surface and the conductive layer. Conductive graphite powders in the machining gap are formed by the breakdown of the dielectric fluid, and conductive particles that are removed from the conductive layer stick to the surface of the non-conductive workpiece through the thermal effect of the discharge and form a thin conductive layer on the surface of the nonconductive workpiece. The process continues by means of the formed carbon layer on the nonconductive workpiece. In this way, EDM is made suitable for the machining of electrically nonconductive workpieces by mixing graphite powder particles into a dielectric liquid and coating the surfaces of the workpieces with a conductive layer.

As noted, a turbine blade is normally coated with a non-conductive coating in order to withstand high temperature operating conditions. Therefore, in order to perform EDM, as a first step for making a series of holes, it is necessary to apply a conductive layer coating at the trailing edge area. This study will simulate this coating process prior to the micro hole machining process.

5.1.2 Conductive Coatings

A plasma spray is used to produce coatings such as a Thermal Barrier Coating and conductive coatings. Micrometer size powders are introduced into a hot plasma jet, then heated and evaporated to form droplets. The droplets collide at high speed with the substrate to form a coating. The droplets are flattened as they cool and solidify due to heat exchange with the substrate. Shinoda et al., [106] experimentally measured the flatness of the particles. It was found that particles' flatness was proportional to 0.2-0.3 powers of the Reynolds number. The droplet impinged on the substrate becomes a

splat or a splash with a large deformation and break-up. Fukumoto et al. [107] measured the threshold temperature between the splash and the splats experimentally.

In previous studies, full-scaling modeling of the plasma spray was performed by solving the fluid flow of the plasma jet using either the FVM (Finite Volume Method) or the FDM (Finite Difference Method), while a simple model with a point mass was used to simulate the powder particle behavior [108][109]. It is difficult to simulate the deformation of the droplet in such approaches, and they are also not suitable to study the physics of the microstructure formation. On the other hand, the VOF (Volume of Fluid) method of the incompressible Navier-Stokes equation is typically used to simulate the collision and deformation processes of a single droplet [110][111][112][113]. The formation processes of the air void, which affect thermal conductivity, have been investigated by simulating the impingement of the multiple droplets on a substrate [114][115]. Full-scale modeling to reproduce the deformation of the droplets is useful for the development of new materials. However, the computation cost is too high to capture the interface of the droplet entirely in full-scale modeling using the VOF method in the Euler coordinate, since the interface resolution requires very fine computational grids. During acceleration and the heating process of the powder, the heat is transferred from the atmospheric gas to the powder particles, and the liquid droplet is deformed by the aerodynamic force from the atmospheric gas. Thus far, however, the physics of these processes has not been fully taken into account in conventional studies. It should be noted that the plasma jet is known to be heavily turbulent, as observed in the experiment reported in [116]. The liquid droplet should be deformed significantly by the turbulence. Moreover, the effect of the aerodynamic force and heat exchange on the substrate has not been considered, to the best of the author's knowledge.

The aim of the present study is to realize a full-scaling modeling that can reproduce the micro-structure of the coatings. The MPS (Moving Particle Semi Implicit) method for computing the large-scale deformation, break-up, and attachment of the liquid droplet is coupled with the FVM for accurately computing the high-speed flows of compressible fluid, while reducing the computational cost as compared to the VOF method. In the present study, the numerical method has been developed along the same line as the FVM-MPS hybrid method developed in an earlier study by Ikejiri et al.

[117]. The hybrid method is now extended to simulate the plasma spray, solving the compressible and viscous gas flow, heat transfer between the droplet and the substrate, and the phase change of the droplet. To the best of the author's knowledge, this is the first time such an extension is being carried out.

5.2 METHODOLOGY

5.2.1 GAS FLOW CALCULATION

FVM (Finite Volume Method) is used for simulating the fluid flows.

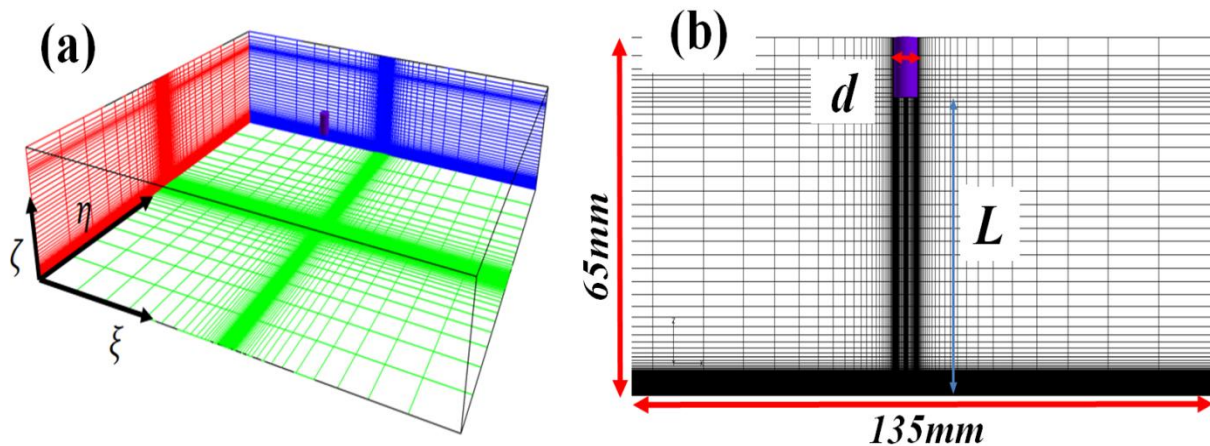


Figure 5.2 (a) Overall computational grid (b) Position of expansion nozzle [d = nozzle diameter (5mm), L = nozzle distance (50mm)]

The unsteady three-dimensional compressible Navier-Stokes equation is solved. Spatial accuracy is extended up to third-order via the MUSCL method [116]. The air is assumed to be an ideal gas (atmospheric air), and the viscosity coefficient is evaluated by using the Sutherland equation. The SLAU method, which is able to maintain accuracy at low Mach number flow, is used to evaluate the non-viscous flux [118]. The Van Albada flux limiter is adapted. Viscous flux is discretized using central difference.

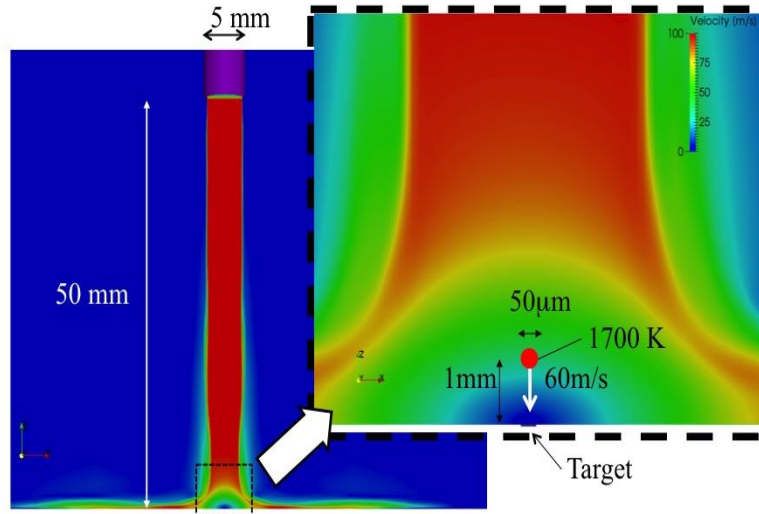


Figure 5.3: The calculated velocity distributions of the jet initial conditions

An explicit third-order TVD Runge-Kutta method is used for the time integration [119]. Fig. 5.2 shows the computational grid used in this calculation. A total grid number of 7.82×10^6 is used. The initial velocity distribution of the jet before inserting particles is shown in Fig. 5.3. If the boundary-fitted grid is used for calculating the flow around the droplet, the boundary layer on the interface of the droplet can be regenerated accurately.

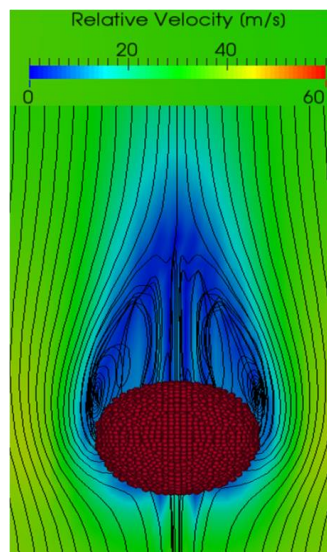


Figure 5.4: Droplet around the flow ($Re = 133$)

However, the computational cost is too high for full-scaling modeling. In the present study, the virtual boundary method is applied to establish the boundary condition of the droplet interface [120]. This method allows the imposition of a non-slip boundary within the flow field by a feedback forcing term which was added in the momentum term, as found in reference [120] and in chapter 5.2.4 of this study. This method is similar to a coordinating transformation, which has been widely used in the finite element method. This external force has been applied at a specific grid point of the simulation. The droplet consisted of particles. Aerodynamic force is exerted on the particle on the interface between the droplet and the atmospheric air, while the reaction force is generated from the particle to the gas. The flow around a droplet is shown in Fig. 5.4. The Reynolds number is 133 in this case. The wake flow geometry is similar to the visualization in the reference [121]. A plausible flow can be formed around the droplets by using the virtual boundary method. The flow calculation without any particles is converged first, and then a droplet of a given initial velocity and temperature is introduced at the height of 1mm above the substrate, as shown in the expanded image in Fig. 5.3. The detailed condition of droplet is presented in Table 5.1.

Table 5.1: Calculation Condition of Droplet and Gas Jet

Droplet Substance	Copper
Substrate Material	SUS304
Distance between initial MPS particle	2.0 μm
Initial Droplet Diameter	50.0 μm
Initial Droplet Velocity	60 m/s
Initial Droplet Condition (height)	1.0 mm
Initial Droplet Temperature	1700K
Substrate Temperature	300K
Droplet Solidification Temperature	1357K
Exit Nozzle Speed	100m/s
Exit Nozzle Temperature	273 K
Exit Nozzle Static Pressure	1.0 atm
Nozzle Diameter	5mm
Nozzle to substrate Distance	50mm

5.2.2 PARTICLE CALCULATION METHOD

The following three-dimensional incompressible Navier-Stokes equation is solved using the MPS method for simulating the droplet dynamics.

$$\begin{aligned} \frac{D\rho}{Dt} &= 0 , \\ \frac{Du}{Dt} + \frac{1}{\rho} \nabla p - \nu \nabla^2 u - F_{ext} &= 0 . \end{aligned} \tag{5.1}$$

The present method follows [122]; it consists of the explicit integration of the velocity field and the implicit integration of the pressure equation. The Laplacian is evaluated using Khayyer's model [123][124]. In addition, the incomplete Cholesky decomposition with conjugate gradient method (ICCG method) is used for the implicit integration of the pressure equation. The water column collapse problem was solved for the validation of the MPS method, and the numerical results were compared with the experimental results [125][126][127]. The FVM flow calculation and the MPS droplet calculation were solved in series, while weakly coupled with each other.

5.2.3 INTERFACE DETERMINATION

The number density of the particle on the free surface is considered to satisfy:

$$n^* < \beta n^0 . \tag{5.2}$$

Here, n^0 is the initial particle number density, and n^* is the particle number density that is calculated after the explicit integration of the velocity field. We set $\beta = 0.95$. In addition, Gotoh et. al [128] conditions are imposed as an auxiliary judgment.

5.2.4 EXTERNAL FORCES (SURFACE TENSION, AIR FORCE) MODEL

The external force term, \mathbf{F}_{ext} includes surface tension, aerodynamic force, and gravity. Most studies so far have used the VOF method, while the CSF (Continuum Surface Force) model has been used for the evaluation of surface tension [129]. In the present study, the Ishii model is used as it is more stable than the CSF model when applied to the particle methods [130]. The normal force originating from the pressure, F_p , and the shear force, F_s are applied on the interface between the gas and the particles. In order to evaluate F_s accurately, it is necessary to resolve the boundary layer of the air flow generated in the droplet surfaces, which may increase computational cost. For this reason, F_p and F_s are being estimated using simple models as follows.

$$\begin{aligned} F_p &= p_i S n_i , \\ F_s &= \frac{1}{2} \rho S C_d (u_i^{\text{gas}} - u_i) |u_i^{\text{gas}} - u_i| , \end{aligned} \quad (5.3)$$

where S is the surface area of a single particle and C_d is the drag coefficient of a sphere as a function of Re , which can be calculated as $\frac{24}{Re}$. n_i is the normal vector of the intersurface at the position of particle i . u_i^{gas} is the velocity vector of the atmospheric gas at the same position as particle i , and u_i is the velocity vector of particle i . For the atmospheric gas, the reaction force is applied on the virtual interface between the gas and the droplet so that the overall momentum is conserved.

5.2.5 HEAT CONDUCTION MODEL

The heat conduction equation was solved to simulate the cooling process between the droplet and the substrate after the contact:

$$\frac{Dh}{Dt} = \nabla j \quad , \quad (5.4)$$

where h is the enthalpy of each particle of the droplet and J is the heat flux from droplet to the base material. The heat flux is given as follows,

$$J = \frac{2k_1k_2}{k_1 + k_2} \nabla j \quad , \quad (5.5)$$

where k_1 is the thermal conductivity of the liquid droplet, and k_2 is the thermal conductivity of the solid substrate. The thermal conduction inside the droplet and the substrate are calculated by solving Eq. (5.5) and putting $k_1=k_2$. The present model for the thermal conduction is simplified by ignoring the contact thermal resistance across the interface, and is much simpler than, for example, the VOF simulation [110].

5.2.6 PHASE TRANSITION (SOLIDIFICATION) MODEL

The solidification fraction, γ , is defined as a discontinuous function of enthalpy as:

$$\gamma = \begin{cases} 1 & (h < h_{s0}) \\ \frac{h_{s1} - h}{h_{s1} - h_{s0}} & (h_{s0} \leq h \leq h_{s1}) \\ 0 & (h > h_{s1}) \end{cases} \quad , \quad (5.6)$$

where h_{s0} and h_{s1} are the enthalpy at the beginning and at the end of the melting process. For simplicity of the analyses, the droplet is assumed to be liquid for $\gamma < 0.5$, and solid for $\gamma \geq 0.5$. After a particle is solidified on the substrate, the particle adheres to the substrate.

5.3 RESULT AND FINDINGS

The velocity distributions of the gas flow and the droplets during the collision process are shown in Fig. 5.5. Due to the motion of the droplet in the gas atmosphere, a wake is generated in the gas behind the droplet. The gas is compressed in a region between the substrate and the droplet prior to the impact, and then the gas expands outward from the collision point horizontally to the substrate surface after the impact. After the impact, the droplet particles in contact with the substrate surface are solidified instantaneously and their motions are stopped, while the particles above the contact surface remain mobile to move in a lateral direction. The lateral motions of these particles are enhanced by the gas flow above the droplet in the lateral direction. After the latter timing ($t = 0.437 \mu\text{s}$), a few particles fly off the droplet.

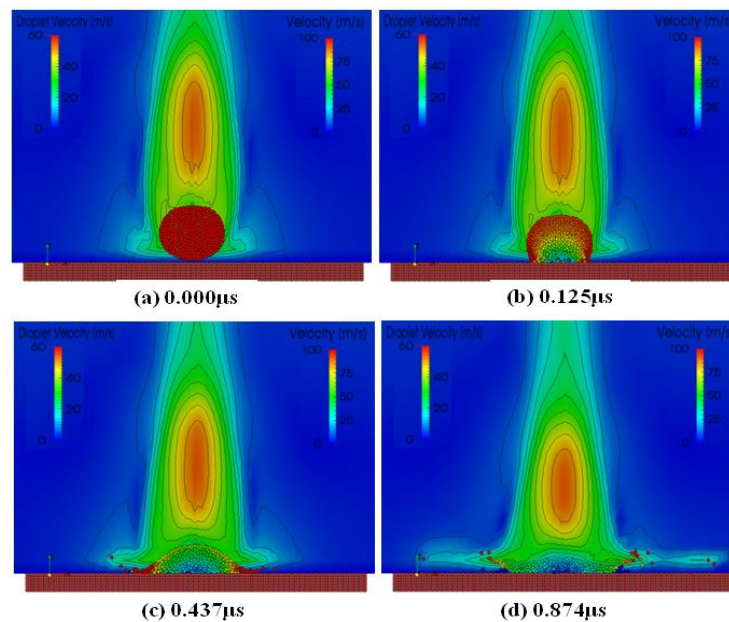


Figure 5.5 The droplet velocity distribution in the collision process

The temperature distribution during the collision process is shown in Fig. 5.6. As shown in Fig 5.6 (a), before impinging on the substrate, the droplet is slightly flattened. Due to the aerodynamic force, the temperature is uniform within the droplet. At $t = 0.25 \mu\text{s}$, the substrate starts to be heated by the droplet while the temperature in the droplet is still high. At $t = 0.8 \mu\text{s}$, the droplet particle starts to cool near the periphery, while the

temperature of the droplet near its center is still high. The solidification of the droplet proceeds from the periphery to the center. At $t = 1.8 \mu\text{s}$, the particles around the periphery are solidified while the temperature near the center is still high so that the particles near the center are still mobile. The solidified particles near the periphery deflect the particles moving outward from the center to the upper direction, like a jump ramp.

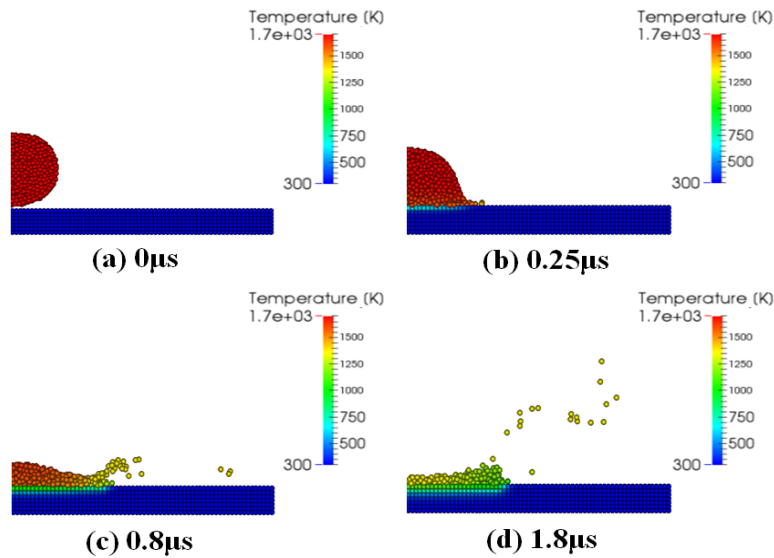


Figure 5.6 The droplet temperature distribution during the collision process

A few particles moving from the center bounce off the periphery. While at $t = 0.8 \mu\text{s}$, the shape of the droplet is convex, and then it becomes concave at $t = 1.8 \mu\text{s}$ due to the deflection at the jump ramp. The shape of the resulting splat is concave. This is consistent with the calculated result using the VOF method [110]. In fact, Kamnis et al. [110] simulated the process using a two dimensional numerical model (VOF method), in order to reduce the computational time and complexity.

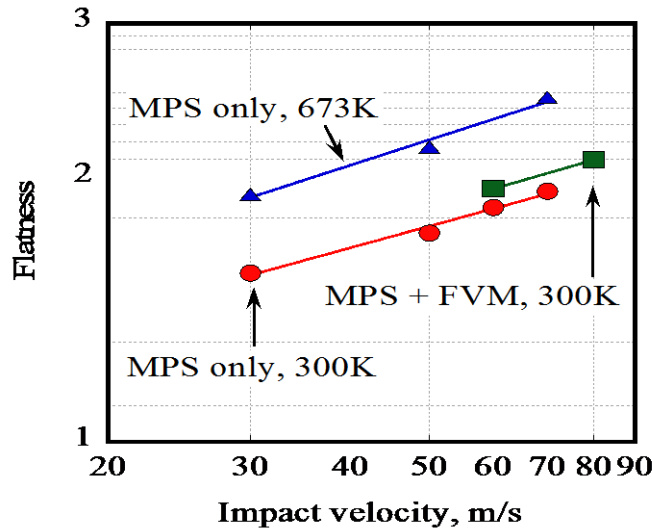


Figure 5.7 Flatness as a function of impact velocity

By using this hybrid FVM + MPS method, a similar result can be obtained in acceptable computational time with three dimensional calculations. The flatness of splat as a function of the impact velocity of the droplet is shown in Fig. 5.7. The flatness or degree of flattening is defined as the ratio of the final splat diameter and the diameter of the particle just before the impingement process. The figure shows the results of both the FVM and MPS coupled analysis (FVM + MPS) and the uncoupled analysis (MPS only) which ignored the aerodynamic force from gas to the droplet. Two different initial temperatures of the substrate were tested. The result shows that flatness increases with impact velocity.

In the case of MPS only, if the initial temperature of the substrate is set at 300K, the flatness is found to be proportional to Reynolds number, $Re^{0.25}$; if the temperature is set at 673K, the flatness is proportional to $Re^{0.30}$. For the initial substrate temperature of 300K, the flatness of the coupled analyses of FVM and MPS is slightly higher than the results of the uncoupled analysis (MPS only), which is proportional to $Re^{0.26}$. The graph trends in each case are similar, and the present results are consistent with previous results obtained from VOF analyses [106], and experimental results [111], in which the flatness was found to be proportional to $Re^{0.2-0.3}$ [106]. When the substrate initial temperature is raised from 300K to 673K, the flatness also increases. The shape of the splat is determined by the dynamic deformation and solidification of the droplets.

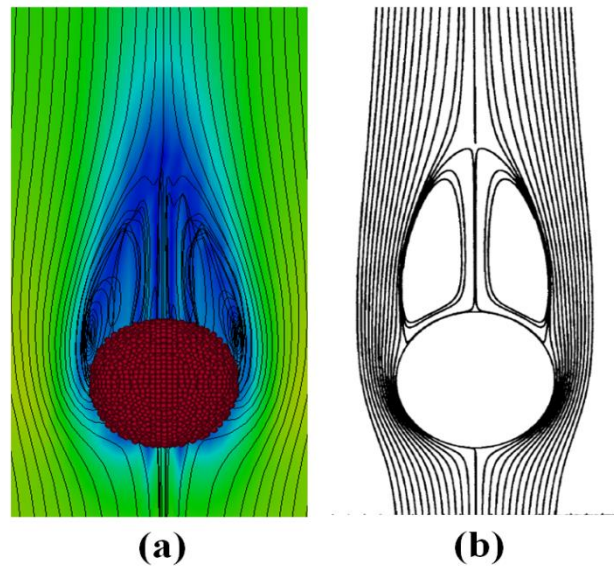


Figure 5.8 Streamline around the droplet (a) CFD calculation (b) Reference [121].

By increasing the initial temperature of the substrate while maintaining the initial droplet temperature, the heat flux from the droplet to the substrate is reduced and overall solidification is delayed. The mobility of the droplet lasts a longer time enabling the higher substrate initial temperature to increase the flatness. The VOF calculation of Al_2O_3 by [111] has shown that the solidification time increases with an increase in the substrate temperature. At the same initial temperature of the substrate, the results in the FVM + MPS coupled analyses show greater flatness than in the uncoupled analysis of the MPS only. This is because the liquid droplet is flattened by the aerodynamic force prior to the collision. The droplet structures on steady axisymmetric flow in Figure 5.8 are also consistent with reference [121]. For convenience, Fig. 5.8 shows both configurations, from the calculation result (Fig. 5.4) and from the reference.

5.4 CONCLUSION

A new method coupling FVM and MPS using a virtual boundary method is introduced. The following conclusions can be drawn:

- (1) The processes from the acceleration and deformation of a droplet under the

influence of ambient gas flow to the solidification of the droplet on a substrate have successfully been observed.

- (2) The trend of flatness at the initial temperature of 300K is proportional to $Re^{0.26}$, which is consistent with the experimental result ($Re^{0.2-0.3}$).
- (3) The splat shape results also agree well with previous VOF method.
- (4) The virtual boundary method in this calculation has successfully realized a full-scale modeling calculation of the plasma spray, with good computational time.

CHAPTER 6

OVERALL CONCLUSION

6.1 PREAMBLE

In Chapter 6, the overall conclusion to the research is presented, and the objectives achieved. Finally, some suggestions are made for future research.

6.2 OVERALL CONCLUSIONS

The following general conclusions can be drawn from the research findings:

- (1) The use of three dimensionalities is important to ensure an accurate result is obtained.
- (2) Different turbulence models give different results. Careful selection of the turbulence model was a vital step toward obtaining an accurate result.
- (3) The proposed method of connecting the suction side and the pressure side of a turbine blade successfully suppressed the vortex at the trailing edge and wake area.
- (4) The optimal application of micro holes is sensitive to location and size.
- (5) With respect to the research parameters, the optimum ($D_h = 0.094D$ at $S/D = \pm 0.62$) gave maximum reduction in wake loss of 10%, reduced wake velocity profile thickness at a maximum of 24% and reduced the frequency peak.
- (6) The proposed method of applying the multi-hole synthetic jet has successfully

- suppressed the vortex at the wake area.
- (7) A small separation on the blade surface is beneficial for single and double row cases, while greater separation is disadvantageous in the case of triple rows.
 - (8) Double rows give maximum reduction in wake loss of 13% and eliminate the pressure coefficient drop spike.
 - (9) A new method that coupled FVM and MPS was successfully developed, in which the process from acceleration until deformation of a droplet can be observed.
 - (10) The flatness of an observed droplet was proportional to $Re^{0.26}$, which is consistent with experimental results. The shapes of droplets also agree well with what is reported in references

6.3 RECOMMENDATIONS

The following are recommendations for future research:

- (1) As comparisons between each turbulence model were made, it was apparent that there are some discrepancies between each turbulence model. As the turbulence model in this study has been limited to only one equation turbulence model, it is suggested that a future researcher implements two equation turbulence models (i.e. k-omega, k-epsilon etc.) for the same study.
- (2) Prior to the results obtained, small discrepancies were observed between the numerical simulation and experimental values, in terms of total pressure distribution along the blade (Fig. 3.5). Since the effects of turbulence models are significant in this study, the modification on existing turbulence model (*SA-DDES*) is also expected to improve this result. This would lead to a novel study in computational fluid dynamic turbulence flow.
- (3) An experiment could be conducted to evaluate the result especially for the effect of through-holes and synthetic jets.
- (4) Since the effect of through-holes has been presented in terms of the Hagen-Poussille equation, for a computational study, a future researcher could attempt

to simulate the flow inside these holes, by using detailed boundary conditions and grids. This would require enhanced computer capability.

- (5) A detailed study could investigate the synthetic jet effect in overall flow (stream-wise and span-wise) direction.

REFERENCES

- [1] Chaluvadi, V.S.P., "Blade - Vortex Interactions in High Pressure Steam Turbines", Doctoral Thesis, Cambridge University, (2000).
- [2] Ciccotelli, G., and Serveding, C.H., "The Effect of Vortex Shedding on the Unsteady Pressure Distribution around Trailing Edge of a Turbine Blade", Transaction of ASME, ASME Journal of Turbomachinery Vol.119, pp.810-819 (1997).
- [3] Denton, J.D., "Loss Mechanisms in Turbomachines", Transaction of ASME, ASME Journal of Turbomachinery, Vol.115, pp. 621-656 (1993).
- [4] Gostelow, J.P., Platzer, M.F., and Carscallen, W.E., "On Vortex Formation in the Wake Flows of Transonic Turbine Blades and Oscillating Airfoils", ASME Journal of Turbomachinery, Vol.128, pp.528-535 (2006).
- [5] Bloor, M.S., "The Transition to Turbulence in the Wake of a Circular Cylinder", Journal of Fluid Mechanics, Vol.19, pp.290-304 (1964).
- [6] Williamson, C. H. K., "Oblique and parallel models of vortex-shedding in the wake of a circular cylinder at low Reynolds number", Journal of Fluid Mechanics, Vol.206, pp.579-627 (1986).
- [7] Gerrard, J. H., "The Mechanics of the Formation Region of Vortices behind Bluff Bodies", Journal of Fluid Mechanics, Vol.25, pp.401-413 (1966).
- [8] Ciccotelli, G., and Serveding, C.H., "A Review of the Research on Unsteady Turbine Blade Wake Characteristics", Technical report, AGARD-CP-571, Loss Mechanisms and Unsteady Flows in Turbomachines, Paper 6, (1996).
- [9] Rouser, K.P., "Use Of Dimples To Suppress Boundary Layer Separation On a Low Pressure Turbine Blade", Technical Paper, Air Force Institute of Technology (2002).
- [10] Chu, T.L., "Effect of Mach Number and Flow incidence on aerodynamic losses on Steam Turbine Blades," Thesis, Virginia Polytechnic University (1999).
- [11] Brooksbank, E.J., "A Numerical Investigation of Time Resolved Flows around Turbine Blades," Ph.D. thesis, University of Leicester, (2001).
- [12] Shaker, S.F., Abdullah, M.Z., Mujeebu, M.A., Ahmad, K.A., and Abdullah, M.K., "Study On The Effect of Number of Film Cooling Rows on the Thermal

- Performance of Gas Turbine Blade” , Journal of Thermal Science and Technology, pp.88-98, (2012).
- [13] Zhang, X.F., and Hodson, H., “Effect of Reynolds Number and Freestream Turbulence Intensity on the Unsteady Boundary Layer Development on an Ultra-High-Lift Low Pressure Turbine Airfoil”, Transaction of ASME, ASME Journal of Turbomachinery, pp.1001-1010 (2010).
- [14] Zhou, C., Hudson, H. and Christop, H., “The Effects of Trailing edge thickness on the losses of Ultrahigh lift Low Pressure Turbine Blade”, ASME Journal of Turbomachinery Vol.136, pp.1-12 (2014).
- [15] Bourgoyne, D.A., Ceccio, S.L., and Dowling, D.R., “Vortex Shedding from a Hydrofoil at High Reynolds Number”, Journal of Fluid Mechanics, Vol.531, pp.293-324 (2005).
- [16] Andre, S.C., and Anthony, J., “Suppression of the unsteady vortex wakes of a circular cylinder pair by a doublet-like counter-rotation”, International Journal for Numerical Methods in Fluids, Vol.206, pp.1-18 (2009).
- [17] Tani, G., “Suppression of vortex shedding from a truncated trailing edge by plasma actuation”, MSc Thesis, pp.5-23 (2011).
- [18] Azebedo, M.A., Cavadas, A.S., Coelho, P.M., Proenca M.F., and Pinho, F.T., “Control of vortex shedding behind a circular cylinder at moderate Reynolds number”, Conferência Nacional em Mecânica dos Fluidos, Termodinâmica e Energia, pp.1-9, (2012).
- [19] Chan, W., Hu, H., and Li, H., “Suppression of Vortex Shedding from a Circular Cylinder by using a Suction Flow Control Method”, AIAA 2013-0103, 51st Aerospace Sciences Meeting and Exhibit, Texas, (2013).
- [20] Johnston, J.P., and Nishi, M., “Vortex-generator Jets-Means for Flow Separation Control”, AIAA Journal, Vol.28, No.6, pp.989-994, (1990).
- [21] Compton, D.A., and Johnston, J.P., “Streamwise Vortex Production by Pitched and Skewed Jets in a Turbulent Boundary-Layer”, AIAA Journal, Vol.30, No.3, pp.640-647, (1992).

- [22] Jeffrey, P.B., Sondergaard, R., and Rivir, R.B., "Turbine Separation Control Using Pulsed Vortex Generator Jets", Transaction of ASME, Journal of Turbomachinery, Vol.123, pp.198-206, (2001).
- [23] Bernardini, C., Carnevale, M., Manna, M., Martelli, F., Simoni, D., and Zunino, P., "Turbine Blade Boundary Layer Separation Suppression via Synthetic Jet an Experimental and Numerical Study", Journal of Thermal Science, Vol. 21, No. 5, Science Press and Institute of Engineering Thermophysics, CAS and Springer, pp.404-412, (2012).
- [24] Borgeson, D., "Boundary Layer Control Using Micro-Electromechanical Systems", Master Thesis, Air Force Institute of Technology, AFIT/GSO/ENY/02-1, (2002).
- [25] Lin, J.C., Howard, F.G., Bushnell, D.M., and Shelby, G.V., "Investigation of Several Passive and Active Methods of Turbulent Flow Separation Control", AIAA Paper #90-1598, (1990).
- [26] Chang, P.K., "Separation of Flow", Pergamon Press, (1970).
- [27] Rao, D.M., and Kariya, T.T., "Boundary-Layer Submerged Vortex Generators for Separation Control – An Exploratory Study", 1st National Fluid Dynamic Congress, AIAA Paper No.88-3546-CP, (1998).
- [28] Bearman, P.W., "Investigation of the flow behind a two-dimensional model with a blunt trailing edge and fitted with splitter plates", Journal of Fluid Mechanics, Vol.21, pp.241-255 (1965).
- [29] McCormick, D.C., "Shock-Boundary Layer Interaction Control with Low-Profile Vortex Generators and Passive Cavity", AIAA Journal, Vol.31, No.1, pp.91-96, (1993).
- [30] Lin, J.C., Howard, F.G., and Shelby, G.V., "Turbulent Flow Separation Control through Passive Techniques", AIAA 2nd Shear Flow Conference, Tempe, AZ, AIAA Paper No.89-0976, (1989).
- [31] Chu, D.C., and Karniadakis, G.E., "A direct numerical simulation of laminar and turbulent flow over riblet-mounted surfaces", Journal of Fluid Mechanics, Vol. 250, pp.1-42, (1993).

- [32] El-Samni, O.A., Chun, H.H., and Yoon, H.S., "Drag reduction of turbulent flow over thin rectangular riblets", *International Journal of Engineering Science*, Elsevier, No.45, pp.436-454, (2007).
- [33] Choi, K.S., "Near-wall structure of a turbulent boundary layer with riblets", *Journal of Fluid Mechanics*, Vol. 208, pp.417-458, (1989).
- [34] Chan, A.S., Dew, P.A., Jameson, A., Liang, C., and Smits, A.J., "Vortex Suppression and Drag Suppression in the Wake of Counter-Rotating Cylinder", *Journal of Fluid Mechanics*, pp.1-40, (2011).
- [35] Bearman, P.W., and Owen, J.C., "Reduction of Bluff-Body Drag and Suppression Of Vortex Shedding by the Introduction of Wavy Separation Lines", *Journal of Fluid Mechanics*, Vol.12, pp.123-130, (1998).
- [36] Bearman, P.W., and Harvey, J.K., "Golf Ball Aerodynamics" *The Aeronautical Quarterly*, Vol.27, No.2, pp.112-122 (1976).
- [37] Aoki, K., Muto, K., and Okanaga, H., "Aerodynamic Characteristics and Flow Pattern of a Golf Ball with Rotation", *Elsevier Procedia Engineering* 2, pp.2431-2436 (2010).
- [38] Bearman, P.W., and Harvey, J.K., "Control of Circular Cylinder Flow by the Use of Dimples", *AIAA Journal*, Vol.31, No.10, pp.1753-1756, (1993).
- [39] Lake, J.P., "Flow Separation Prevention on a Turbine Blade in Cascade at Low Reynolds Number", PhD Dissertation, Air Force Institute of Technology, AFIT/DS/ENY/99-01 (1999).
- [40] Effendy, M., Yao, Y., and Yao, J., "Comparison Study of Turbine Blade with Trailing-Edge Cutback coolant Ejection Designs", *Proceeding of 51st AIAA Aerospace Sciences Meeting including the New Horizons Forum and Aerospace Exposition*, AIAA 2013-0548, pp.1-12 (2013).
- [41] Lutum, E., and Johnson, B.V., "Influence of the Hole-to-Diameter ratio on Film Cooling with cylindrical hole", *ASME Journal of Turbomachinery* Vol.121, pp.209-216 (1999).
- [42] Veldhuis, L.L.M., Jansen, D.P., Haddar, J.E., and Correale, G., "Novel Passive and Active Flow Control for High Lift", 28th *International Congress of the Aeronautical Sciences ICAS 2012*, Brisbane, Australia (2012).

- [43] Hoffmann, K.A., and Chiang, S.T., "Computational Fluid Dynamics", Engineering Education System, (2000).
- [44] Anderson JR, J.D., "Computational Fluid Dynamics the Basic with Application", McGraw Hill, (1995).
- [45] Jameson, A., and Yoon, S., "Lower-Upper Implicit Schemes with Multiple Grids for the Euler Equations", Journal of AIAA, Vol.25, No.7, pp.929-935 (1987).
- [46] Yoon, S., and Jameson, A., "An LU-SSOR for the Euler and Navier-Stokes Equations", NASA-CR-179556, (1986).
- [47] Yoon, S., and Jameson, A., "Lower-Upper Symmetric-Gauss-Seidel Method for the Euler and Navier-Stokes Equations", Journal of AIAA, Vol.26, No.9, pp.1025-1026 (1988).
- [48] Arnone, A., Liou, M., and Povinelli, L.A., "Integration of Navier-Stokes Equations Using Dual Time Stepping and a Multigrid Method", Journal of AIAA, Vol.33, No.6, pp.985-990 (1995).
- [49] Dubuc, L., Cantariti, F., Woodgate, M., Gribben, B., Badcock, K.J., and Richards, B.E., "Solution of the Unsteady Euler Equations Using an Implicit Dual-Time Method", Journal of AIAA, Vol.36, No.8, pp.1417-1424 (1998).
- [50] Yoon, S., and Kwak, D., "Three-Dimensional Incompressible Navier-Stokes Solver using Lower-Upper Symmetric Gauss-Seidel Algorithm", Journal of AIAA, Vol.29, No.6, pp.874-875 (1991).
- [51] Yoon, S., and Kwak, D., "Implicit Navier-Stokes Solver for Three-Dimensional Compressible Flows", Journal of AIAA, Vol.30, No.11, pp.2653-2659 (1992).
- [52] Obayashi, S., and Kuwahara, K., "An Approximate LU Factorization Method for the Compressible Navier-Stokes Equations", Journal of Computational Physics, Vol.36, No.8, pp.1417-1424 (1986).
- [53] Blazek, J., "Computational Fluid Dynamics; Principles and Applications", Elsevier, pp.267-293 (2001).
- [54] Liou, M., and Steffen, C.J., "New Flux Splitting Scheme", Journal of Computational Physics, Vol.107, pp.23-23 (1993).

- [55] Wada, Y., and Liou, M.S., "An Accurate and Robust Flux Splitting Scheme for shock and Contact Discontinuities", *SIAM Journal of Scientific Computing*, Vol.18, pp.633-657 (1997).
- [56] Hirsch, C., "Numerical Computation of Internal and External Flows", Engineering Education System (2000).
- [57] Roe, P.L., "Approximate Riemann Solver, Parameter Vectors, and Difference Schemes", *Journal of Computational Physics*, Vol.43, pp.357-372 (1981).
- [58] Davies, D.E., and Salmond, D.J., "Calculation of the Volume of a General Hexahedron for Flow Predictions", *Journal of AIAA*, Vol.39, No.5, pp.787-793 (2001).
- [59] Vinokur, M., "An Analysis of Finite-Difference and Finite-Volume formulations of Conservation Laws", NASA CR-177416 (1986).
- [60] Clark, J.P., and Grover, E.A., "Assessing Convergence in Predictions of Periodic-Unsteady Flow Fields", *ASME Journal of Turbomachinery*, Vol. 129, pp.740-749 (2007).
- [61] Cerri, G., Giovannelli, A., Battisti L., and Fedrizzi, R., "Advances in effusive cooling techniques of gas turbine", *Journal of Applied Thermal Engineering*, Elsevier, Vol. 27, pp.692-698.
- [62] Spalart, P.R., and Allmaras, S.R., "A One-Equation Turbulence Model for Aerodynamics Flows", 30th Aerospace Sciences Meeting & Exhibition, January 1992, pp.1-22 (1992).
- [63] Deck, S., Duvéau, P., D'Espiney, P., and Guillen, P., "Development and application of Spalart-Allmaras One Equation Turbulence Model to Three Dimensional Supersonic Complex Configuration", *Elsevier Aerospace Science and Technology*, No.6, pp.171-183 (2002).
- [64] Spalart, P.R., Jou, W.-H., Strelets, M., and Allmaras, S.R., "Comments on the feasibility of LES for wings, and on a hybrid RANS/LES approach", *Advances in DNS/LES*, pp.137-147 (1997).
- [65] Spalart, P.R., Deck, S., Shur, M.L., Squires, K.D., Strelets, M.K. and Travin, A., "A New Version of Detach-Eddy Simulation, Resistant to ambiguous Grid

- Densities”, Theoretical Computational Fluid Dynamics, Vol.20, pp.181-195 (2006).
- [66] Chai, X., and Manesh, K., “Dynamic k-Equation Model for Large Eddy Simulation of Compressible Flow”, AIAA 2010-5026, pp.1-13 (2010).
- [67] Deardorff, J.W., “A Numerical Study of Three-Dimensional Turbulent Channel Flow at Large Reynolds Number”, Journal of Fluid Mechanics, Vol.41, Part 2, pp.453-480 (1970).
- [68] Yangwei, L., Jinjing, S. and Lipeng, S., “Corner Separation Control by Boundary Layer Suction Applied to a Highly Loaded Axial Compressor Cascade”, MDPI Journal Energies, Vol.119, pp.786-793 (2014).
- [69] Kurmanov, B., Namba, M., and Podvidz, G., “Turbulent Flow Computation in Film-Cooling Turbine Cascade”, Proceedings of the International Gas Turbine Congress 2003 Tokyo, pp.1-8 (2003).
- [70] El-Gendi, Mohammed, K.I., Mori, K., and Nakamura, Y., “Novel Flow Control Method of Vortex Shedding for a Turbine Blade”, Transaction Japan Society of Aeronautic Space Science, Vol.53, pp.122-129 (2010).
- [71] Sieverding, C.H., Ottolia, D., Bagner, C., Comadoro, A., Brouckaert, J.F., and Desse, J., “Unsteady Turbine Blade Wake Characteristics”, ASME Journal of Turbomachinery, Vol.126, pp.551-559 (2004).
- [72] Sieverding, C.H., Richard, H. and Desse, J., “Turbine Blade Trailing Edge Flow Characteristics at High Subsonic Outlet Mach Number”, ASME Journal of Turbomachinery, Vol.125, pp.298-309 (2003).
- [73] Lipowsky, H., Kovalcheck, S., and Zweifach, B.W., “The distribution of blood rheological parameters in the microvasculature of cat mesentery”, Circulation Res, Issue 43, pp.738-749 (1978).
- [74] Skalak, R., “Capillary Flow: Past, Present and Future”, Biorheology, No.27, pp.277-293 (1990).
- [75] Loudon, C., and McCulloh, K., “Application of the Hagen-Poiseuille Equation to Fluid Feeding Through Short Tubes”, Entomological Society of America, Vol.92, No.1, pp.153-158 (1999).

- [76] Potsdam, M., and Pullian, T., "Turbulence modeling treatment for rotorcraft wakes", In AHS Specialist's Conference on Aeromechanics, Jan. 23-25 (2008).
- [77] M.El-Ghondour, Shatat, M.M.E., and Nakamura, Y., "On the physics of Vortex Formation at the Tip of a Turbine Blade", ASME Turbo Expo 2012: Turbine Technical Conference and Exposition, June 11-15 (2012).
- [78] Magagnato, F., and Gabi, M., "Prediction of Transitional Flow of Turbine Blades with DDES and LES", Proceedings of 8th World Congress on Computational Mechanics, July 2008 (2008).
- [79] Friedrichs, S., Hodson, H.P., and Dawes, W.N., "The Design of an Improved Endwall Film-Cooling Configuration", ASME Journal of Turbomachinery, Vol.121, pp.772-780 (1999).
- [80] Shan, J.W., and Dimotakis, P.E., "The Turbulent Mixing in Transverse Jets", Proceedings of the 3rd Australasian Conference on Hydraulics and Fluid Mechanics, pp.159-163 (1968).
- [81] Saha, A.K. and Shrivastava, A., "Suppression of Vortex Shedding around a Square Cylinder using Blowing", Sadhana Springer, Vol.40, pp.769-785 (2015).
- [82] Mulleners, K., Gilge, P. and Hohenstein, S., "Impact of surface roughness on the Turbulent Wake Flow of a Turbine Blade", Journal of Aerodynamics, pp.1-9 (2014).
- [83] Collie, J.C., Moses, H.L., Schetz, J.A. and Geogory B.A., "Recent Advances in Simulating Unsteady Flow Phenomena Brought About by Passage of Shock Waves in a Linear Turbine Cascade", ASME Journal of Turbomachinery, Vol.115, pp.687-698 (1993).
- [84] Bunker, R.S., "A Review of Shaped Hole Turbine Film-Cooling Technology", ASME Journal of Heat Transfer, Vol.127, pp.441-453 (2005).
- [85] Prato, J. and Lakshminarayana, B., "Investigation of Compressor Rotor Wake Structure at Peak Pressure Rise Coefficient and Effects of Loading", ASME Journal of Turbomachinery, Vol.115, Issue.3, pp.487-500 (1993).
- [86] Konopka, M., Meinke, M., and Shrouder, W., "Large-Eddy Simulation of Supersonic Film Cooling at Finite Pressure Gradients", Springer-Verlag Berlin Heidelberg, pp.353-369 (2012).

- [87] Smith, B. L. and Swift, G. W., "Synthetic jet at Large Reynolds Number and Comparison to Continuous Jets", *Journal of AIAA*, pp.2001-3030 (2001).
- [88] Liu, X. and Wang, X., "Performance Improvement of Low Pressure Turbine Blade by using Synthetic Jets", *Engineering Application of Computational Fluid Mechanics*, Vol.3, No.4, pp.445-458 (2011).
- [89] Memory, C., Gompertz, K., Chen, J. P. and Bons, J., "Numerical Simulations of Vortex Generating Jets on Low Pressure Turbine Blades", *Journal of AIAA*, (2010).
- [90] Smith, B.L., and Glezer, A., "The Formation and Evolution of Synthetic Jets", *Journal of Physics and Fluids*, Vol.10, No.9, pp.2281-2297 (1998).
- [91] Aram, S., and Mittal, R., "Computational Study of the Effect of Slot Orientation on Synthetic Jet-Based Separation Control", *International Journal of Flow Control* (2016).
- [92] Rizetta, D.P., and Visbal, M.R., "Numerical Study of Active Flow Control for a Transitional Highly Loaded Low Pressure Turbine", *Journal of Fluid Engineering*, Vol.128, No.9, pp.956-967 (2006).
- [93] Argawal, R.K., and Vadillo, J.L., "Active Control of Shock / Boundary Layer Interaction in Transonic Flow over Airfoils", *Proceedings of the 21st International Congress of Theoretical and Applied Mechanics* (2005).
- [94] Huang, J.H., Corke, T.C., and Thomas, F.O., "Plasma Actuators for Separation control of Low Pressure Turbine Blades", *Journal of AIAA*, Vol.44, No.1, pp.51-57 (2006).
- [95] Shur, M.L., Spalart, P.R., Strelets, M.K., and Travin, A.K., "A Hybrid RANS-LES Approach with Delay DES and Wall-Modelled LES Capabilities", *International Journal of Heat and Fluid Flow*, Elsevier, Vol.29, pp.1638-1649 (2008).
- [96] Postl, D., Gross, A., and Fasel, H.F., "Numerical Simulations of Active Flow Control of Low Pressure Turbine Blades", *42nd AIAA Aerospace Sciences Meeting*, Reno, NV (2004).
- [97] Buren, T.V., Whalen, E., and Amitay, M., "Interaction between vortex generator and a synthetic jet in cross flow", *Physic of Fluids*, Vol.27, pp.107101 (2015).

- [98] Frank, J.A., "Large-eddy simulation of flow separation and control on a wall mounted hump", PhD Thesis, Mechanical Engineering, The Johns Hopkins University (2011).
- [99] Walters, D.K., and Lylek, J. H., "Impact of Film-Cooling Jets on Turbine Aerodynamic Losses", ASME Journal of Turbomachinery, Vol.122, pp.537-545 (2000).
- [100] Masuzawa, T., "State-of-the-art in micro machining", Annals of the CIRP, vol.49, no.2, pp.473-488 (2000).
- [101] Masuzawa, T., "Micro EDM", The 13th Proceedings of The International Symposium on Electromachining (ISEM XIII), vol.1, pp.3-19 (2001).
- [102] Uhlmann, E., and Domingos, D.C., "Investigations on vibration-assisted EDM-machining of seal slots in high-temperature resistant materials for turbine components" The 17th CIRP Conference on Electro Physical and Chemical Machining (ISEM XVII), Procedia CIRP 6, pp.71-76 (2013).
- [103] Diver, C., Atkinson, J., Helml, H.J., and Li, L., "Micro-EDM drilling of tapered holes for industrial applications", Journal of Materials Processing Technology, vol.149, pp.296-303 (2004).
- [104] Hao, T., Yong, L., Zhang, L., and Baoquan, Li., "Mechanism design and process control of micro EDM for drilling spray holes of diesel injector nozzles", Precision Engineering, vol.37, pp.213-221 (2013).
- [105] Kucukturk, G., and Cogun, C., "A New Method for Machining of Electrically Nonconductive Workpieces Using Electric Discharge Machining Technique", Machining Science and Technology, Vol.14, pp.189-207 (2010).
- [106] Shinoda, K., Koseki, T., and Yoshida, T., "Influence of Impact Parameters of Zirconia Droplets on Splat Formation and Morphology in Plasma Spraying", Journal of Applied Physics, Vol.100- 074903 (2006).
- [107] Fukumoto, M., Kato, S., and Okane, I., "Effect of Substrate Temperature on Splating Behavior of Plasma Sprayed Ni Particles", (In Japanese), Journal Japan Inst. Metals, Vol.58, No10, pp.1191-1195 (1994).
- [108] Zagorski, A.V., and Stadelmaier, F., "Full-Scale Modelling of a Thermal Spray Process", Surface and Coatings Technology, Vol.146–147, pp.162–167 (2001).

- [109] Nishiyama, H., "Control of Nano-Micro Particulate Plasma Flow Processes by Integrating Numerical Simulation and Experiment", (In Japanese), Japanese Journal of Multiphase Flow, Vol.24, No.1, pp.3-11 (2010).
- [110] Kamnis, S., and Gu, S., "Numerical Modeling of Droplet Impingement", Journal Physics D: Applied Physics, Vol.38, pp.3664-3673 (2005).
- [111] Chaea, Y.K., Mostaghimi, J., and Yoshida, T., "Deformation and Solidification Process of a Super-Cooled Droplet Impacting on the Substrate Under Plasma Spraying Conditions", Science and Technology of Advanced Materials 1, pp.147-156, (2000).
- [112] El-Hadja, A.A., Zirari, M., and Bacha, N., "Numerical Analysis of the Effect of the Gas Temperature on Splat Formation during Thermal Spray Process", Applied Surface Science, Vol.257, pp.1643–1648, (2010).
- [113] Zheng, Y.Z., Li, Q., Zheng, Z.H., Zhu, J.F., and Cao, P.L., "Modeling the Impact, Flattening and Solidification of a Molten Droplet on a Solid Substrate during Plasma Spraying", Applied Surface Science, Vol.317, pp.526–533, (2014).
- [114] Hejun, L., Pengyun, W., Lehua, Q., Hansong, Z., Songyi, Z., and Xianghui, H., "3D Numerical Simulation of Successive Deposition of Uniform Molten Al Droplets on a Moving Substrate and Experimental Validation", Computational Materials Science, Vol.65, pp.291–301 (2012).
- [115] Kumar, A., Ghosh, S., and Dhindaw, B.K., "Simulation of Cooling of Double-Layered Splat and its Experimental Validation Using Jackson–Hunt Theory", Metallurgical and Materials Transactions B, Vol.42B, pp.269-273 (2011).
- [116] Toro, E.F., "Riemann Solvers and Numerical Methods for Fluid Dynamics", Springer-Verlag, Berlin, (2009).
- [117] Ikejiri, S., Liu, J., and Oka, Y., "Simulation of a Single Bubble Rising with Hybrid Particle-Mesh method", Journal of Nuclear Science and Technology, Vol.44, No.6, pp.886-893 (2007).
- [118] Shima, E., and Kitamura, K., "Parameter-Free Simple Low-Dissipation AUSM-Family Scheme for All Speeds", AIAA Journal, Vol.49, No.8, pp.1693-1709 (2011).
- [119] Shu, C.W., and Osher, S., "Efficient Implementation of Essentially Non-

- Oscillatory Shock-Capturing Schemes”, *Journal of Computational Physics*, Vol.77, No.2, pp.439-471, (1988).
- [120] Saiki, E.M., and Biringen, S., “Numerical Simulation of a Cylinder in Uniform Flow: Application of a Virtual Boundary Method”, *Journal of Computational Physics*, Vol.123, No.0036, pp.450–465 (1996).
- [121] Johnson, T.A., and Patel, V.C., “Flow Past a Sphere up to a Reynolds Number of 300”, *Journal of Fluid Mechanics*, Vol.378, pp.19-70 (1999).
- [122] Koshizuka, S., and Oka, Y., “Moving Particle Semi-Implicit Method for Fragmentation of Incompressible Fluid”, *Nuclear Science and Engineering*, Vol.123, No.3, pp.421-434 (1996).
- [123] Khayyer, A., and Gotoh, H., “Enhancement of Stability and Accuracy of the Moving Particle Semi-Implicit Method”, *Journal of Computational Physics*, Vol.230, No.8, pp.3093-3118 (2011).
- [124] Khayyer, A., and Gotoh, H., “A 3D Higher Order Laplacian Model for Enhancement and Stabilization of Pressure Calculation in 3D MPS-Based Simulations”, *Applied Ocean Research*, Vol.37, No.1, pp.120-126 (2012).
- [125] Hirt, C.W., and Nichols, B.D., “Volume of Fluid (VOF) Method for the Dynamics of Free Boundaries”, *Journal of Computational Physics*, Vol.39, No.1, pp.201-225 (1981).
- [126] Koshizuka, S., “A Particle Method for Incompressible Viscous Flow with Fluid Fragmentation”, *Computational Fluid Dynamics Journal*, Vol.4, pp.29-46 (1995).
- [127] Martin, J.C., and Moyce, W.J., “Part IV. An Experimental Study of the Collapse of Liquid Columns on a Rigid Horizontal Plane, *Philosophical Transaction of the Royal Society of London*”, Series A, Mathematical and Physical Sciences, Vol.244, No.882, pp.312-324 (1952).
- [128] Gotoh, H., Khayyer, A., and Hori, C., “New Assessment Criterion of Free Surface for Stabilizing Pressure Field in Particle Method”, (In Japanese), *Journal of Japan Society of Civil Engineers, Ser. B2 (Coastal Engineering)* Vol.65, No.1, pp.21-25 (2009).
- [129] Brackbill, J.U., Kothe, D.B., and Zemach, C., “A Continuum Method for Modeling Surface Tension”, *Journal of Computational Physics*, Vol.100, pp.335-

354 (1992).

- [130] Ishii, E., and T.Sugii, T., “Development of Surface Tension Model for Particle Method”, (In Japanese), Transactions of The Japan Society of Mechanical Engineers Series B, Vol.78, No.794, pp.1710-1725 (2012).
- [131] Ugrina, S., “Experimental Analysis and Analytical Modelling of Synthetic Jet – Cross Flow Interaction”, Technical paper, pp.97-103 (2007).
- [132] Huang, S., “Effect of Jet-to-Crossflow Pressure Ratio Arrangement on Turbulent Mixing in a Flowpath with Square Staged Injectors”, Journal of Fuel, Elsevier, pp.164-170 (2015).
- [133] Huang, L., Huang, P.G., and LeBeau, R.P., “Numerical Study of Blowing and Suction Control Mechanism on NACA 0012 Airfoil”, Journal of Aircraft, Vol. 41, No.5, pp.1005-1013 (2004).
- [134] Shojaefard, M.H., Noorpoor, A.R., and Ghaffarpour, M., “Numerical Investigation of Flow Control by Suction and Injection”, American Journal of Applied Science 2, Vol. 10, pp.1474-1480 (2005).

LIST OF PUBLICATIONS

JOURNALS

TITLE: Effect of Multiple Through-Holes on the Turbine Blade Trailing Edge
AUTHORS: Mohd Hafiz Mohd Noh, Koichi Mori
JOURNAL NAME: International Journal of Advancements in Mechanical and Aeronautical Engineering (IJAMAE 2016)
DATE ACCEPTED: 1st July 2016
DATE PUBLICATION: 31st August 2016
VOLUME: 3
ISSUE: 2
ISSN NUMBER: 2372-4153
PAGE: 7-15

TITLE: Different Synthetic Jet Hole Arrangement on a High Subsonic Turbine Blade
AUTHORS: Mohd Hafiz Mohd Noh, Koichi Mori
JOURNAL NAME: Journal of Technology (Scopus Elsevier indexed)
DATE ACCEPTED: 16th March 2016
DATE PUBLICATION: In Press
VOLUME: In Press
ISSUE: Special Issue 2016/2017
ISSN NUMBER: 2180-3722

TITLE: Simulation of Compressible and Multi-Phase Flow in Plasma Spray with a FVM-MPS Hybrid Method
AUTHORS: Mohd Hafiz Mohd Noh, Naoki Sawada, Koichi Mori
JOURNAL NAME: Frontier of Applied Plasma Technology
DATE ACCEPTED: 1st August 2016

DATE PUBLICATION: 1st September 2016
VOLUME: 9
ISSUE: No.1 January 2016
ISSN NUMBER: -
PAGE: 27-32

CONFERENCE / SYMPOSIUMS / PROCEEDINGS

TITLE: An Approach for Pressure Distribution Improvement on Turbine Cascade Trailing Edge
AUTHORS: Mohd Hafiz Mohd Noh, Koichi Mori
SYMPOSIUM NAME: The 28th Computational Fluid Dynamics Symposium
DATE: 9th – 11th December 2014
PLACE: Tokyo, Japan

TITLE: Different Synthetic Jet Hole Arrangement on a High Subsonic Turbine Blade
AUTHORS: Mohd Hafiz Mohd Noh, Koichi Mori
SYMPOSIUM NAME: 2016 Advanced Research in Material Sciences, Manufacturing, Mechanical and Mechatronic Engineering Technology International Conference (AR4MET 2016)
DATE: 12th – 14th April 2016
PLACE: Jakarta, Indonesia